RESEARCH ARTICLE

Vacancies and spin–phonon coupling in CrSi$_{0.8}$Ge$_{0.1}$Te$_3$

Ana Milosavljević[1] [ORCID] | Andrijana Šolajić[1] | Bojana Višić[1] | Marko Opačić[1] |
Jelena Pešić[1] | Yu Liu[2] | Cedomir Petrovic[2] | Zoran V. Popović[1,3] |
Nenad Lazarević[1]

[1]Institute of Physics Belgrade, University of Belgrade, Pregrevica 118, Belgrade, 11080, Serbia

[2]Condensed Matter Physics and Materials Science Department, Brookhaven National Laboratory, Upton, New York, 11973-5000, USA

[3]Serbian Academy of Sciences and Arts, Knez Mihailova 35, Belgrade, 11000, Serbia

Correspondence
Ana Milosavljević, Institute of Physics Belgrade, University of Belgrade, Pregrevica 118, 11080 Belgrade, Serbia.
Email: ana.milosavljevic@ipb.ac.rs

Funding information
Serbian Academy of Sciences and Arts, Grant/Award Number: F-134; Slovenian Research Agency, Grant/Award Number: P1-0099; Ministry of Education, Science and Technological Development of the Republic of Serbia U.S. DOE-BES, Division of Materials Science and Engineering, Grant/Award Number: DE-SC0012704

Abstract

We report temperature-dependent Raman scattering and magnetization studies of van der Waals ferromagnetic compound CrSi$_{0.8}$Ge$_{0.1}$Te$_3$. Magnetic susceptibility measurements revealed dominant ferromagnetic interactions below T_C which shift to the lower values due to the presence of vacancies. A Raman active mode, additional to the ones predicted by symmetry in the parent compounds, has been observed. This A_g symmetry mode most likely emerges as a consequence of the atomic vacancies on Si/Ge site. Presence of the strong spin–phonon coupling at temperature around 210 K is indicated by deviations from conventional phonon self-energy temperature dependence of all analysed modes.

KEYWORDS

magnetism, phonons, raman spectroscopy, van der Waals materials

1 | INTRODUCTION

Considerable progress has been made in the field of material science through developing new materials and revealing their properties in the last decade. Namely, in the recent years, large family of van der Waals materials with inherent magnetism became the focus of experimental and theoretical research, because they seem suitable for numerous technical applications.[1-7] The family includes Fe$_{3-x}$GeTe$_2$ metallic materials with high magnetic transition temperature,[8-10] semiconductors CrXTe$_3$ (X = Si, Ge, Sn) and CrX$_3$ (X = Cl, Br, I) monolayers[2,11-13] and heterostructures.[14]

CrSiTe$_3$ and CrGeTe$_3$ are ferromagnetic (FM) semiconductors with band gap of 0.4 and 0.7 eV and Curie temperatures (T_C) of 32 and 61 K, respectively.[15-18] Twining of CrSiTe$_3$ single crystals along c-axes was revealed by X-ray diffraction experiment as well as Cr^{3+} ions magnetic order.[15] Recently, through high-resolution angle-resolved photoemission spectroscopy (ARPES), it was possible to identify full electronic structure near the Fermi level. Due to spin–orbit coupling, CrSiTe$_3$ is a Mott-type FM insulator.[19] Electronic structure of CrGeTe$_3$ single crystals was also investigated by ARPES.[20] It was shown that the low-lying valence bands are centred around the Γ point and are mainly formed from Te 5p orbitals.

Raman scattering studies of $CrSiTe_3$ reveal strong spin–lattice coupling in the paramagnetic phase[15,21] as a consequence of a short-range magnetic order in this compound. In addition to renormalization of energies and linewidths of observed Raman active modes, coupling of doubly degenerate E_g mode with magnetic continuum was found.[21] The coupling results in an asymmetric phonon line shape up to 180 K. Besides the splitting of two low-energy E_g modes in the magnetic phase of $CrGeTe_3$ and unconventional behaviour of phonon properties around transition temperature, experimental results indicate spin–phonon coupling effect with magnetic quasi-elastic scattering.[22] Pressure-dependent Raman scattering study of $CrGeTe_3$ showed a decrease in bond length, the deviation of Cr–Te–Cr angle, and reduction of phase transition temperature.[23]

Change of the carrier concentration plays an important role in the physics of semiconducting materials as it can lead to surprising physical properties. Very small variations in dopant concentrations can lead to structural modifications and considerable changes in magnetic transition temperature. Here, we report a Raman scattering and magnetization studies of $CrSi_{0.8}Ge_{0.1}Te_3$. Our scanning electron microscopy (SEM) measurements reveal 10% of Ge atoms concentration and 10% of vacancies. Vacancies induced a decrease in T_C was detected within magnetic susceptibility measurements. In the Raman scattering results, we identified three A_g and four E_g symmetry modes. Additional peak of the A_g symmetry is also observed in our spectra. This mode may be traced to vacancies and possible inhomogeneous distribution of Ge atoms substitution on Si atomic site at nano-scale. Energies of modes predicted by symmetry analysis are found between the experimental values of parent compounds $CrSiTe_3$ and $CrGeTe_3$, reported previously in Milosavljevi et al..[21] The presence of the strong spin–phonon interaction at temperature around 210 K is indicated in small deviations from conventional temperature-dependent behaviour of the observed modes energies and linewidths, including additional one.

2 | EXPERIMENT AND NUMERICAL METHOD

$CrSi_{0.8}Ge_{0.1}Te_3$ single crystals were grown as described previously.[24] Magnetic properties were measured in a Quantum Design MPMS-XL5 system.

SEM measurements were performed using FEI HeliosNanolab 650. This microscope is equipped with an Oxford Instruments energy dispersive spectroscopy (EDS) system with an X-max SSD detector operating at 20 kV. Measurements were performed on as-cleaved samples deposited on a graphite tape. The elemental composition EDS mapping was obtained on crystals that appeared to be uniform for several tens of microns. The maps show the presence of Cr, Ge, Te and Si.

For Raman scattering experiment, Tri Vista 557 spectrometer was used in the subtractive backscattering micro-Raman configuration. The combination of gratings was 1800/1800/2400 grooves/mm and the entrance slit of $80\,\mu m$. Solid state laser with 532-nm line was used as an excitation source. In our scattering configuration, plane of incidence is ab-plane, where $|a|=|b|$ ($\sphericalangle(a,b)=120°$), with incident (scattered) light propagation direction along c-axes. Samples were cleaved in the air before being placed in vacuum. All measurements were performed in high vacuum (10^{-6} mbar) using a KONTI CryoVac continuous Helium flow cryostat with 0.5-mm thick window. Laser beam focusing was achieved using microscope objective with $\times 50$ magnification. All spectra were corrected for Bose factor.

Spin-polarized density functional theory calculations were performed in Quantum Espresso software package,[25] based on plane waves and pseudopotentials, using Perdew–Burke–Ernzerhof (PBE) exchange-correlation functional[26] and projector augmented wave (PAW) pseudopotentials.[27,28] The cutoff for wavefunctions and the charge density of 85 and 425 Ry were chosen, respectively. The k-point were sampled using the Monkhorst-Pack scheme, on $8 \times 8 \times 8$ Γ centred grid used for both structures. Optimization of the lattice parameters and atomic positions in unit cell was performed until the interatomic forces were minimized down to 10^{-6} Ry/Å. Treatment of the van der Waals interactions is included using the Grimme-D2 correction, in order to obtain the lattice parameters more accurately. Phonon wave numbers were calculated within the linear response method, as implemented in PHonon part of Quantum Espresso.
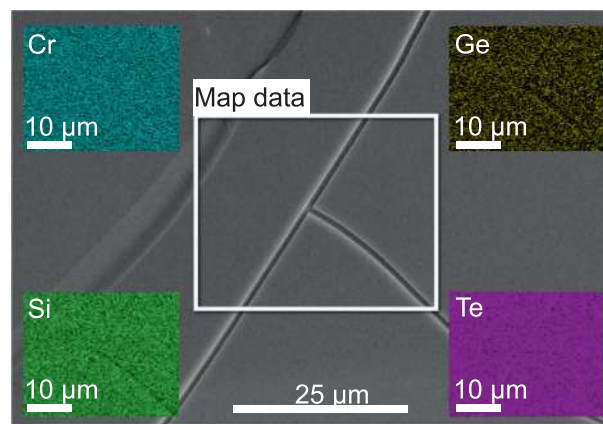

FIGURE 1 Energy dispersive spectroscopy (EDS) mapping on a $CrSi_{0.8}Ge_{0.1}Te_3$ single crystal [Colour figure can be viewed at wileyonlinelibrary.com]

3 | RESULTS AND DISCUSSION

In order to investigate uniformity and elemental composition of $CrSi_{0.8}Ge_{0.1}Te_3$ sample, SEM measurements were performed on as-cleaved crystals. EDS mapping presented in Figure 1 shows that the ratio of Cr:Si:Ge:Te (averaged over 10 measurements) is 1:0.8:0.1:3. This result reveals the presence of 10% Ge atomic vacancies in the sample.

Figure 2a,b presents the temperature dependence of zero-field cooling (ZFC) magnetic susceptibility $\chi(T) = M(T)/H$ measured in 1-kOe magnetic field applied parallel to a (a) and c (b) crystallographic axes. Curie–Weiss law $\chi = \frac{C}{T-\theta}$ fit at high temperatures yields Weiss temperatures $\theta_a = 61(2)$ K, $\theta_c = 70(2)$ K and high temperature paramagnetic moments $\mu_{eff,a} = 4.14(2)\mu_B$ and $\mu_{eff,c} = 3.91(2)\mu_B$ for $CrSi_{0.8}Ge_{0.1}Te_3$, consistent with dominant FM interactions below T_c and in line with the observed FM T_c and magnetic hysteresis loops.[13,24] The approximate T_c value can be determined from the minima of the $d\chi/dT$ curves insets in Figure 2(a,b). It should be noted
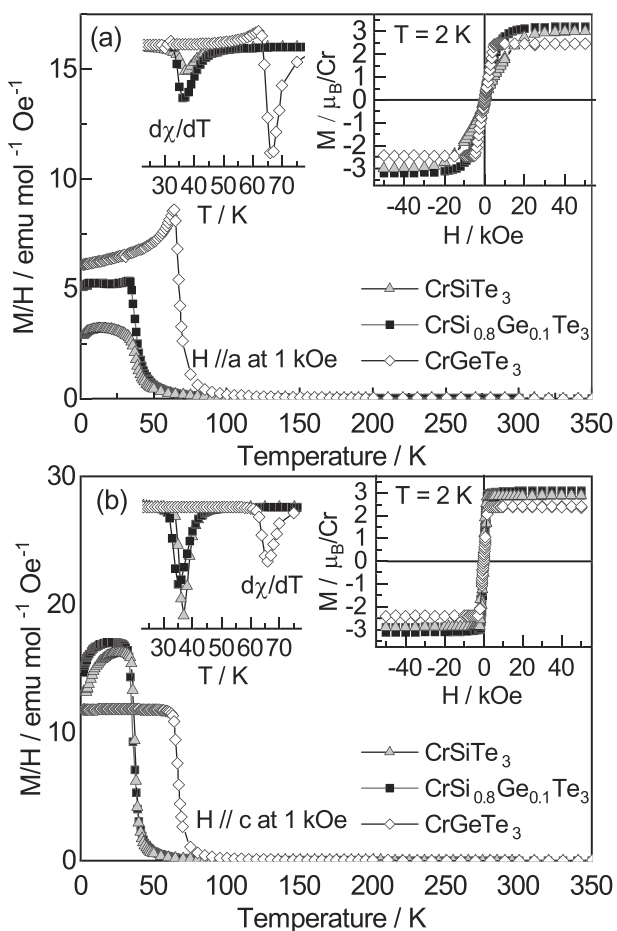
that, instead of monotonous rise, there is a weak but discernible shift to lower temperature in $d\chi/dT$ in $CrSi_{0.8}Ge_{0.1}Te_3$ when compared with $CrSiTe_3$. This small reduction in FM transition temperature is likely induced by the presence of vacancies, as suggested by the EDS data. The presence of vacancies in this class of materials usually disarrange magnetic exchange due to disorder increment, which leads to the reduction of T_C.[29]

Isostructural parent compounds $CrSiTe_3$ and $CrGeTe_3$ crystallize in the rhombohedral crystal structure, described with space group $R\overline{3}$ (C_{3i}^2).[30] According to factor group analysis, five A_g and five double degenerate E_g symmetry modes are expected to be observed in the light scattering experiment. Detailed symmetry analysis, phonon mode distribution and selection rules for parent compounds ($CrSiTe_3$ and $CrGeTe_3$) can be found in Milosavljević et al.[21] In our scattering configuration, the plane of incidence is ab plane, where $|a| = |b|$ ($\angle(a,b) = 120°$) (inset in Figure 3), and the direction of incident (scattered) light propagation is along c-axes. According to the selection rules for this scattering configuration,[21] all Raman active modes may be observed, having in mind that A_g symmetry modes can be detected only in parallel polarization configuration. The E_g symmetry modes are expected to appear in both the parallel and cross polarization configurations. Raman spectra of $CrSi_{0.8}Ge_{0.1}Te_3$, obtained by continuous change of the angle between polarization vectors of incident and

FIGURE 2 Temperature dependence of zero-field cooling (ZFC) $\chi = M/H$ for $CrSiTe_3$, $CrSi_{0.8}Ge_{0.1}Te_3$ and $CrGeTe_3$ in 1-kOe magnetic field applied in-plane (a) and along the c-axis (b). Insets show transition temperatures of ferromagnetic orders ($d\chi/dT$) and magnetic hysteresis loops taken at 2 K

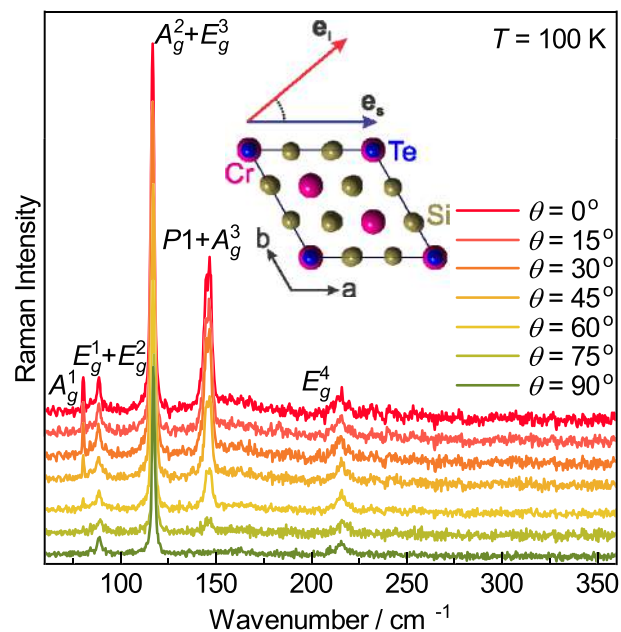**FIGURE 3** Raman spectra of $CrSi_{0.8}Ge_{0.1}Te_3$ single crystal, measured at 100 K, as a function of angle θ, between incident and scattered light polarization. Inset: schematic representation of the incident and scattered light polarization with respect to the crystal orientation [Colour figure can be viewed at wileyonlinelibrary.com]

scattered light, $\theta = \sphericalangle(\mathbf{e}_i, \mathbf{e}_s)$, $(0° \leqslant \theta \leqslant 90°)$ at 100 K, are shown in Figure 3. It can be seen that by changing this angle, starting from $\theta = 0°$, the intensities of the peaks at energies 80.2, 116.4 and 145.5 cm^{-1} continuously decrease and completely vanish for polarization angle of 90°. Therefore, these excitations obey pure A_g symmetry. On the other hand, the peaks at energies of 84.5, 88.3, 117.2 and 215.0 cm^{-1} are not influenced by change of polarization angle, so they can be identified as E_g symmetry modes.

Here, one should note that the feature observed at around 117 cm^{-1} in both scattering configurations is actually a two-peak structure comprising of 116.4-cm^{-1} A_g and 117.2-cm^{-1} E_g symmetry modes. Detailed analysis of the structure for two scattering configurations is presented in Figure A1 of Appendix. Furthermore, closer inspection of the data revealed that peak at energy of 145.5 cm^{-1}, which obeys pure A_g symmetry, is also composed of two modes, $P1$ (144.6 cm^{-1}) and A_g^3 (146.7 cm^{-1}), as shown in Figure A2 of Appendix.

Calculated optical phonon wavenumbers of the parent compounds, CrSiTe$_3$ and CrGeTe$_3$, together with their experimental Raman active values as well as Raman mode energies of CrSi$_{0.8}$Ge$_{0.1}$Te$_3$, are compiled in Table 1. As expected, experimental values of CrSi$_{0.8}$Ge$_{0.1}$Te$_3$ Raman active modes are found between the values of the observed modes in parent compounds.[21] Figure 4a shows compositional evolution of the peaks with highest
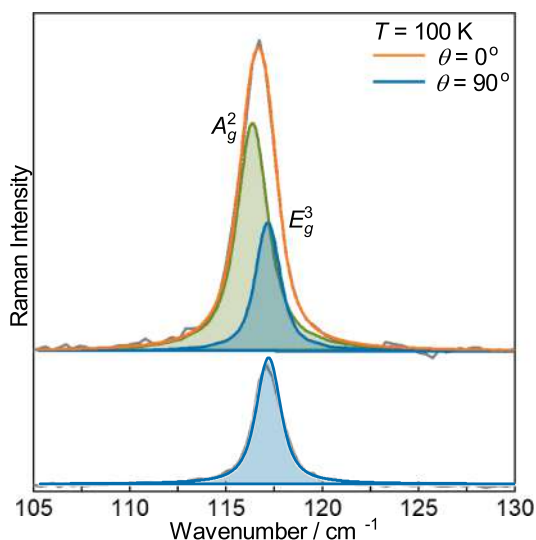

FIGURE A2 Decomposition of phonon mode in parallel scattering configuration on two A_g symmetry modes. Open circles represent the measured data and the blue one sum of two Voigt profile line shapes. Data modelled with one Voigt profile line shape (orange line) deviates significantly from measured data [Colour figure can be viewed at wileyonlinelibrary.com]

intensity, assigned as E_g^3 and A_g^3 symmetry modes in parent compounds. The E_g^3 mode energy changes almost linearly (Figure 4b), as a consequence of change in lattice parameters and "change of mass" effect. The observed energy shift is followed by doubling of the linewidth, dominantly induced by the significant crystalline disorder. The similar type of behaviour, with somewhat larger increase in the linewidth, was also observed for the A_g^3 symmetry mode. The most striking feature was the additional A_g symmetry mode (denoted as $P1$, see Figure A2 of the Appendix), observed in the doped sample. Generally, both the substitutional defects and vacancies may have similar impact on the Raman modes energy and linewidth. Here, the appearance of $P1$ peak can be understood as a consequence of the presence of vacancies on Si/Ge atomic site and their inharmonious distribution at nano-scale. The mode "splitting" is detected only for the A_g^3 but not for other observed modes, due to the fact that different nature of these vibrations results in different values of energy shifts. In the case of other modes, the difference between the shifts for corresponding domains is smaller than the spectral resolution of the instrument ($\sim$1.8 cm^{-1}), and therefore, the separate modes can not be resolved.

Figure 5 shows CrSi$_{0.8}$Ge$_{0.1}$Te$_3$ Raman scattering spectra measured at various temperatures. For clarity, spectra obtained for cross polarization configuration are

FIGURE A1 Decomposition of unresolved A_g^2 and E_g^3 symmetry modes obtained by simultaneous modelling in parallel and cross polarization configuration. Grey line represents the measured data, Voigt line of A_g^2 mode is shown by green, and blue lines represent the E_g^3 symmetry mode in parallel (upper panel) and cross (lower panel) polarization. The orange line is the superposition of these two lines [Colour figure can be viewed at wileyonlinelibrary.com]
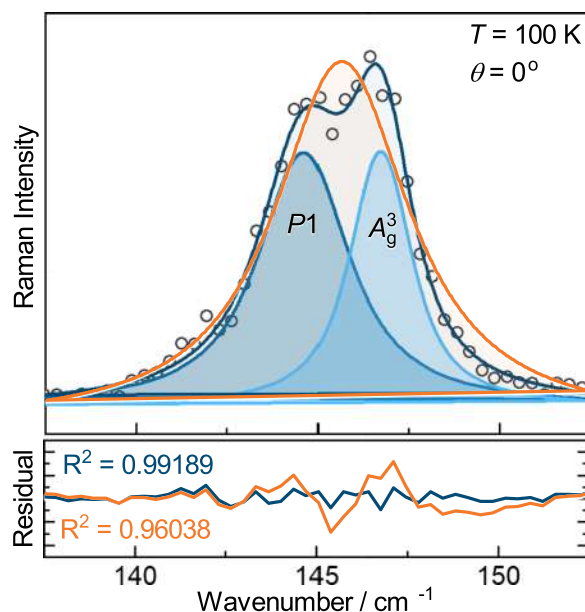
TABLE 1 Phonon symmetry, calculated ($T = 0$ K) and experimental ($T = 100$ K) Raman active phonon wavenumbers of parent compounds CrSiTe$_3$ and CrGeTe$_3$.[21] Experimental values for Raman active phonons of CrSi$_{0.8}$Ge$_{0.1}$Te$_3$ at 100 K are shown in the last column

Raman active modes					
	Calculations		**Experiment**		
Symmetry	**CrSiTe$_3$**	**CrGeTe$_3$**	**CrSiTe$_3$**	**CrGeTe$_3$**	**CrSi$_{0.8}$Ge$_{0.1}$Te$_3$**
A_g^1	88.2	84.2	—	—	80.2
E_g^1	93.5	82.0	88.9	83.5	84.5
E_g^2	96.9	90.8	—	—	88.3
E_g^3	118.3	114.2	118.2	112.2	117.2
A_g^2	122.0	105.9	—	—	116.4
A_g^3	148.0	134.8	147.4	137.9	146.7
A_g^4	208.7	200.3	—	—	—
E_g^4	219.5	209.6	217.2	217.5	215.0
E_g^5	357.4	229.8	—	—	—
A_g^5	508.9	290.7	—	296.6	—

Note: All values are given in cm^{-1}.

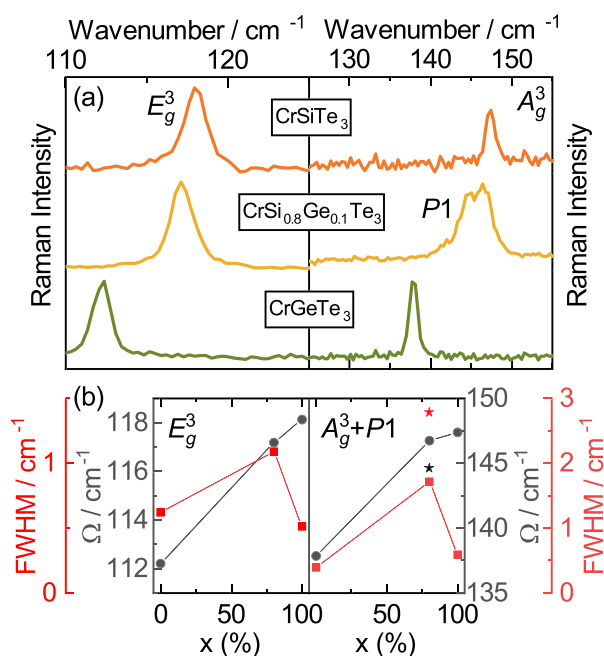**FIGURE 4** (a) Raman scattering spectra of E_g^3 and A_g^3 phonon modes of CrSiTe$_3$ (orange line), CrSi$_{0.8}$Ge$_{0.1}$Te$_3$ (yellow line) and CrGeTe$_3$ (green line) at $T = 100$ K measured in cross (left panel) and parallel (right panel) scattering configuration, respectively. (b) Energy (grey line) and linewidth (red line) of these two modes with respect to the percentage of Si atoms concentration. Energy and linewidth of $P1$ mode are marked with black and red star, respectively [Colour figure can be viewed at wileyonlinelibrary.com]
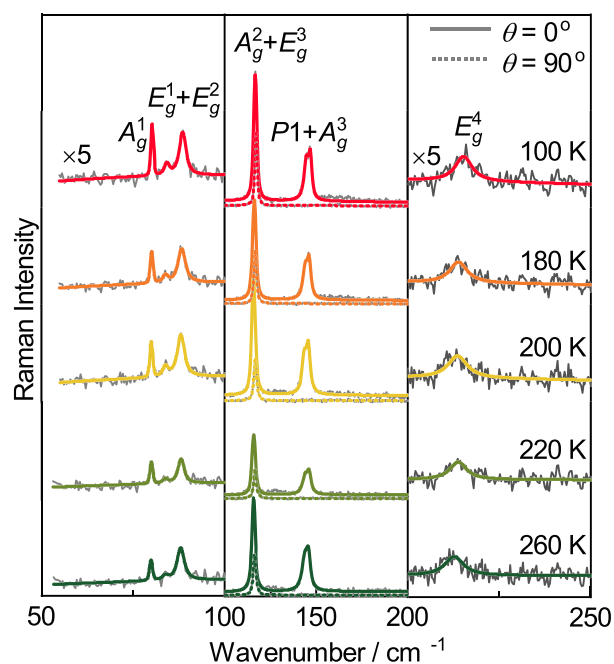
FIGURE 5 Raman spectra of CrSi$_{0.8}$Ge$_{0.1}$Te$_3$ single crystal measured at various temperatures. The spectra were analysed by using multiple Voigt peak functions and a single $\chi''_{cont} = a\Gamma\omega/(\Gamma^2 + \omega^2) + b\omega$ function, for parallel ($\theta = 0°$, solid coloured lines) and cross ($\theta = 90°$, dashed coloured lines) scattering configuration. For clarity, higher and lower energy ranges (left and right panel) are multiplied by the factor of five [Colour figure can be viewed at wileyonlinelibrary.com]

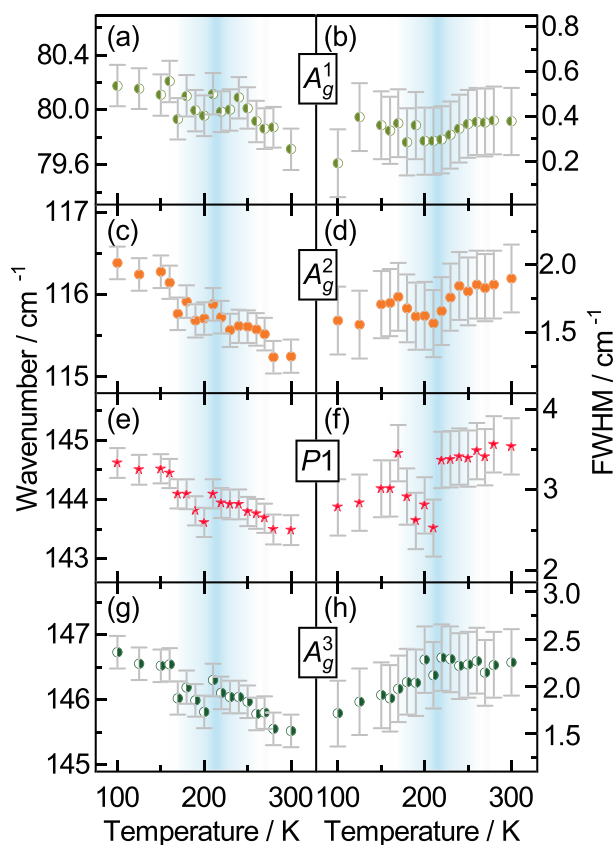**FIGURE 6** Energy and linewidth temperature dependence of A_g^1 (a,b), A_g^2 (c,d), $P1$ (e,f) and A_g^3 (g,h) Raman modes [Colour figure can be viewed at wileyonlinelibrary.com]
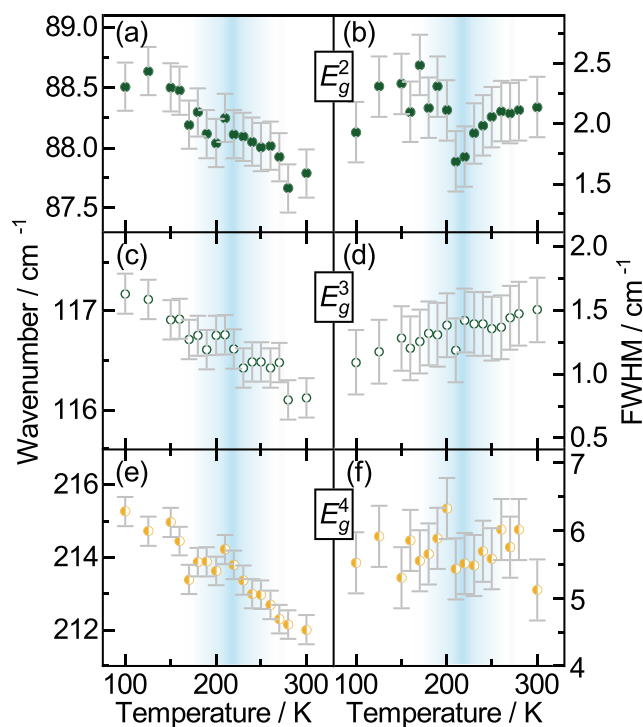

FIGURE 7 Energy and linewidth temperature dependence of E_g^2 (a,b), E_g^3 (c,d) and E_g^4 (e,f) symmetry modes [Colour figure can be viewed at wileyonlinelibrary.com]

only shown for the mid-energy range. Temperature dependence of energies and linewidths of all the observed A_g symmetry modes, including $P1$, are presented in Figure 6. By heating the sample from 100 K to approximately 210 K, monotonous decrease in energy of all the A_g symmetry modes is present, dominantly driven by thermal expansion.[31] In the temperature region around 210 K, these modes' energy exhibit small deviation, followed by a continuous decrease up to room temperature. In the same temperature region, deviation from expected anharmonic type of behaviour is observed for all the A_g symmetry modes linewidth. This effect is more pronounced for higher energy modes where the anharmonicity is expected to be higher. Similar response of analysed E_g symmetry modes is present and shown in Figure 7.

Concerning previously reported strong spin–phonon coupling in CrSiTe$_3$,[15,21] which persists up to 180 K, we believe that this unconventional behaviour of energies and linewidths can be attributed to the coupling of the phonon modes to the spin system.[32] Due to the doping and presence of vacancies, strong magnetic correlations in CrSi$_{0.8}$Ge$_{0.1}$Te$_3$ are sustained up to 210 K.

4 | CONCLUSIONS

In summary, we presented temperature-dependent Raman scattering and magnetization studies of doped van der Waals ferromagnet CrSi$_{0.8}$Ge$_{0.1}$Te$_3$. SEM measurements revealed the presence of 10% vacancies on Si/Ge atomic site. As a consequence, magnetization measurements detected small but clear decrease in T_C. Seven out of 10 Raman active modes have been assigned in our Raman spectra. Temperature dependence of all the observed modes shows the persistence of magnetic correlations up to 210 K. In addition, the results revealed the appearance of the peak that obey pure A_g symmetry, which is attributed to the possible inhomogeneous distribution of Ge atoms and vacancies at nano-scale. This study provides an insight into the impact of doping and presence of vacancies on magnetic and lattice properties in this class of materials.

ORCID

Ana Milosavljević 🄳 https://orcid.org/0000-0002-8654-0475

REFERENCES

[1] F. Hellman, A. Hoffmann, Y. Tserkovnyak, G. S. Beach, E. E. Fullerton, C. Leighton, A. H. MacDonald, D. C. Ralph, D. A. Arena, H. A. Dürr, P. Fischer, *Rev. Mod. Phys.* **2017**, *89*, 025006.

[2] N. Sivadas, M. W. Daniels, R. H. Swendsen, S. Okamoto, D. Xiao, *Phys. Rev. B* **2015**, *91*, 235425.

[3] K. S. Novoselov, A. K. Geim, S. V. Morozov, D. Jiang, Y. Zhang, S. V. Dubonos, I. V. Grigorieva, A. A. Firsov, *Science* **2004**, *306*(5696), 666.

[4] Q. H. Wang, K. Kalantar-Zadeh, A. Kis, J. N. Coleman, M. S. Strano, *Nat. Nanotechnol.* **2012**, *7*, 699.

[5] G. Cheng, L. Lin, L. Zhenglu, S. Alex, X. Yang, C. Ting, B. Wei, W. Chenzhe, W. Yuan, Z. Q. Qiu, R. J. Cava, G. L. Steven, X. Jing, Z. Xiang, *Nature* **2017**, *546*, 265.

[6] B. Huang Bevin, G. Clark, E. Navarro-Moratalla, D. R. Klein, R. Cheng, K. L. Seyler, D. Zhong, E. Schmidgall, M. A. McGuire, D. H. Cobden, W. Yao, *Nature* **2017**, *546*, 270.

[7] K. S. Burch, D. Mandrus, J.-G. Park, *Nature* **2018**, *563* (7729), 47.

[8] J.-X. Zhu, M. Janoschek, D. Chaves, S. J. C. Cezar, T. Durakiewicz, F. Ronning, Y. Sassa, M. Mansson, B. L. Scott, N. Wakeham, E. D. Bauer, J. D. Thompson, *Phys. Rev. B* **2016**, *93*, 144404.

[9] B. Chen, J. H. Yang, H. D. Wang, M. Imai, H. Ohta, C. Michioka, K. Yoshimura, M. H. Fang, *J. Phys. Soc. Japan* **2013**, *82*(12), 124711.

[10] A. Milosavljević, A. Šolajić, S. Djurdjić-Mijin, J. Pešć, B. Višić, Y. Liu, C. Petrovic, N. Lazarević, Z. V. Popović, *Phys. Rev. B* **2019**, *99*, 214304.

[11] M. A. McGuire, H. Dixit, V. R. Cooper, B. C. Sales, *Chem. Mat.* **2015**, *27*(2), 612.

[12] H. L. Zhuang, Y. Xie, P. R. C. Kent, P. Ganesh, *Phys. Rev. B* **2015**, *92*, 035407.

[13] G. T. Lin, H. L. Zhuang, X. Luo, B. J. Liu, F. C. Chen, J. Yan, Y. Sun, J. Zhou, W. J. Lu, P. Tong, Z. G. Sheng, *Phys. Rev. B* **2017**, *95*, 245212.

[14] M. Gibertini, M. Koperski, A. F. Morpurgo, K. S. Novoselov, *Nat. Nanotech.* **2019**, *14*(5), 408.

[15] L. D. Casto, A. J. Clune, M. O. Yokosuk, J. L. Musfeldt, T. J. Williams, H. L. Zhuang, M.-W. Lin, K. Xiao, R. G. Hennig, B. C. Sales, J.-Q. Yan, D. Mandrus, *APL Mat.* **2015**, *3*(4), 041515.

[16] X. Zhang, Y. Zhao, Q. Song, S. Jia, J. Shi, W. Han, *JJpn. J. Appl. Phys.* **2016**, *55*(3), 033001.

[17] B. Siberchicot, S. Jobic, V. Carteaux, P. Gressier, G. Ouvrard, *Phys. J. Chem.* **1996**, *100*(14), 5863.

[18] V. Carteaux, F. Moussa, M. Spiesser, *EPL.* **1995**, *29*(3), 251.

[19] J. Zhang, X. Cai, W. Xia, A. Liang, J. Huang, C. Wang, L. Yang, H. Yuan, Y. Chen, S. Zhang, Y. Guo, *Phys. Rev. Lett.* **2019**, *123*, 047203.

[20] Y. F. Li, W. Wang, W. Guo, C. Y. Gu, H. Y. Sun, L. He, J. Zhou, Z. B. Gu, Y. F. Nie, X. Q. Pan, *Phys. Rev. B* **2018**, *98*, 125127.

[21] A. Milosavljević, A. Šolajić, J. Pešć, Y. Liu, C. Petrovic, N. Lazarević, Z. V. Popović, *Phys. Rev. B* **2018**, *98*, 104306.

[22] Y. Tian, M. J. Gray, H. Ji, R. J. Cava, K. S. Burch, *2D Mater.* **2016**, *3*(2), 025035.

[23] Y. Sun, R. C. Xiao, G. T. Lin., R. R. Zhang, L. S. Ling, Z. W. Ma, X. Luo, W. J. Lu, Y. P. Sun, Z. G. Sheng, *Appl. Phys. Lett.* **2018**, *112*(7), 072409.

[24] Y. Liu, C. Petrovic, *Phys. Rev. Mater.* **2019**, *3*, 014001.

[25] P. Giannozzi, S. Baroni, N. Bonini, M. Calandra, R. Car, C. Cavazzoni, D. Ceresoli, G. L. Chiarotti, M. Cococcioni, I. Dabo, A. Dal Corso, *J. Phys. Condens. Matter.* **2009**, *21*(39), 395502.

[26] J. P. Perdew, K. Burke, M. Ernzerhof, *Phys. Rev. Lett.* **1996**, *77*, 3865.

[27] P. E. Blöchl, *Phys. Rev. B* **1994**, *50*, 17953.

[28] G. Kresse, D Joubert, *Phys. Rev. B* **1999**, *59*, 1758.

[29] F. A. May, S. Calder, C. Cantoni, H. Cao, M. A. McGuire, *Phys. Rev. B* **2016**, *93*, 014411.

[30] R. E. Marsh, *J. Solid State Chem.* **1988**, *77*(1), 190.

[31] M. Opačić, N. Lazarević, M. Šćepanović, H. Ryu, H. Lei, C. Petrovic, Z. V. Popović, *J. Phys. Condens. Matter.*, *48*(27), 485701.

[32] F. Feng, N. Lazarević, C. Liu, J. Ji, Y. Wang, S. He, H. Lei, C. Petrovic, R. Yu, Z. V. Popović, Q. Zhang, *Phys. Rev. B* **2019**, *99*, 144419.

APPENDIX: A DECOMPOSITION OF UNRESOLVED MODES

Analysing the spectra of $CrSi_{0.8}Ge_{0.1}Te_3$ single crystal, in different polarization configurations (Figure 3), in the energy range around $117 \, cm^{-1}$, becomes clear that lower energy part completely disappears in cross polarization configuration, whereas higher energy part persists. Enlarged part of this energy region is shown in Figure A1, in parallel and cross polarization configuration at temperature of 100 K. After simultaneous modelling of these spectra becomes clear that they consist of the A_g^2 and E_g^3 modes, at energies 116.4 and $117.2 \, cm^{-1}$, respectively. This is completely supported with theoretical calculations presented in Table 1.

On the other hand, existence of $P1$ is not predicted by theoretical calculations, as Raman active peak. Only closer inspection and detailed analysis, presented in Figure A2, shows that much better agreement with experimental results gives modelling as a superposition of two Voigt lines.

PAPER • OPEN ACCESS

Influence of crystal structure and oxygen vacancies on optical properties of nanostructured multi-stoichiometric tungsten suboxides

To cite this article: Bojana Višić *et al* 2022 *Nanotechnology* **33** 275705

You may also like

- A Solar Coronal Hole and Fast Solar Wind Turbulence Model and First-orbit Parker Solar Probe (PSP) Observations
L. Adhikari, G. P. Zank and L.-L. Zhao

- Oxide-Thickness-Dependent Suboxide Width and Its Effect on Inversion Tunneling Current
Yen-Po Lin and Jenn-Gwo Hwu

- Detonation wave of condensation
A V Eremin and V E Fortov

Influence of crystal structure and oxygen vacancies on optical properties of nanostructured multi-stoichiometric tungsten suboxides

Bojana Višić[1,2,5] , Luka Pirker[1,5] , Marko Opačić[2], Ana Milosavljević[2], Nenad Lazarević[2], Boris Majaron[3,4] and Maja Remškar[1]

[1] Department of Condensed Matter Physics, Jozef Stefan Institute, Jamova Cesta 39, 1000 Ljubljana, Slovenia
[2] Institute of Physics Belgrade, University of Belgrade, Pregrevica 118, 11080 Belgrade, Serbia
[3] Department of Complex Matter, Jozef Stefan Institute, Jamova 39, 1000 Ljubljana, Slovenia
[4] Faculty of Physics and Mathematics, University of Ljubljana, Jadranska 19, Slovenia

E-mail: bojana.visic@ipb.ac.rs

CrossMark

Abstract

Four distinct tungsten suboxide (WO_{3-x}) nanomaterials were synthesized via chemical vapour transport reaction and the role of their crystal structures on the optical properties was studied. These materials grow either as thin, quasi-2D crystals with the W_nO_{3n-1} formula (in shape of platelets or nanotiles), or as nanowires (W_5O_{14}, $W_{18}O_{49}$). For the quasi-2D materials, the appearance of defect states gives rise to two indirect absorption edges. One is assigned to the regular bandgap occurring between the valence and the conduction band, while the second is a defect-induced band. While the bandgap values of platelets and nanotiles are in the upper range of the reported values for the suboxides, the nanowires' bandgaps are lower due to the higher number of free charge carriers. Both types of nanowires sustain localized surface plasmon resonances, as evidenced from the extinction measurements, whereas the quasi-2D materials exhibit excitonic transitions. All four materials have photoluminescence emission peaks in the UV region. The interplay of the crystal structure, oxygen vacancies and shape can result in changes in optical behaviour, and the understanding of these effects could enable intentional tuning of selected properties.

Supplementary material for this article is available online

(Some figures may appear in colour only in the online journal)

---

1. Introduction

The family of tungsten oxides, including stoichiometric WO_3 and WO_2 and substoichiometric Magnèli phases (WO_{3-x}, $0 < x < 1$), is widely studied due to numerous intriguing properties [1–5]. These tungsten (sub)oxides have been used as photodetectors [6, 7] and gas sensors [8–10], in photocatalysis and photoelectrochemical water splitting [3, 11, 12],

in smart windows [13] and optoelectronics [14]. In bulk form, WO_3 is a large indirect bandgap n-type semiconductor, with bandgap values reported in the 2.6–3.0 eV range [15–17]. In nanosized WO_3, quantum size effects appear, resulting in a blueshift of the bandgap up to 3.25 eV, with the bandwidth modulation correlated to the size of the nanoparticles [18]. This is a direct consequence of the quantum confinement effect.

Due to the crystal shear mechanism, various substoichiometric Magnèli phases with different combinations of edge- or corner-sharing WO_6 octahedra can be formed [19]. This may lead to appearance of crystal shear (CS) planes and pentagonal columns (PC), which form to accommodate oxygen vacancies [20, 21]. For less reduced suboxides (i.e. x <0.2), CS planes occur; while PCs are formed for x greater than 0.2. In the former, CS planes' corner-sharing WO_6 octahedra become edge-sharing [22], while in the latter WO_7 bipyramids are formed and share their equatorial edges with the WO_6 octahedra [23]. The degree of reduction and appearance of oxygen vacancies can be crucial for understanding the change of the optical response with respect to the fully oxidized WO_3 [8]. Furthermore, it was reported that the oxygen vacancy defect states induced by annealing can significantly improve electrical conductivity [24]. Substoichiometric WO_{3-x} are mostly found to be blue or light green, which is a structure-sensitive phenomenon and is mainly a consequence of the stoichiometry or oxygen vacancies [25, 26]. First-principles pseudopotential and total-energy projector-augmented wave method calculations showed that single oxygen vacancies and substoichiometric crystal structures modify the optical properties and generate different types of defect states in the bulk [27, 28].

For nanostructured WO_{3-x}, various phenomena may lead to different size- and shape- dependent behaviour within the same stoichiometry. This can lead to seemingly contradictory results, if only the effect of the degree of reduction is considered. It was reported that the metallic $WO_{2.83}$ nanorods ($W_{24}O_{68}$) can sustain strong localized surface plasmon resonances (LSPR), centred around 1.4 eV (corresponding to $\lambda = 900$ nm) [26]. Electrical transport measurements of $WO_{2.8}$ (W_5O_{14}) show that they exhibit metallic behaviour [29]. On the other hand, based on electrical transport measurements and photoluminescence spectra, $WO_{2.72}$ ($W_{18}O_{49}$) nanowires (NWs) show a semiconducting behaviour [30, 31].

A close relationship between the creation of oxygen vacancies and stoichiometry (i.e. degree of reduction) and morphology has been reported [32–34]. Both the stoichiometry and the amount of oxygen vacancies heavily depend on the synthesis conditions, and in turn determine the optical and electrical properties, such as photoluminescense and electrical conductivity. Therefore, a careful structural study of these materials is significant for interpreting optical spectra. In this paper, we report on optical properties of various nanostructured suboxides; namely, multistoichiometric W_nO_{3n-1} in two distinct morphologies (platelets and nanotiles), and W_5O_{14} ($WO_{2.8}$) and $W_{18}O_{49}$ ($WO_{2.72}$) nanowires.

2. Methods

2.1. Synthesis

All the materials were synthesized via chemical vapour transport reaction in a two-zone furnace, using iodine as the transport agent. The synthesis protocols are described in detail in [29, 35–37].

2.2. Electron microscopy

Scanning electron microscopy (SEM) was performed on Supra 35 VP (Carl Zeiss, Germany). High-resolution transmission electron microscopy (HRTEM) and electron diffraction (ED) images were obtained by a Cs probe-corrected TEM/STEM JEOL ARM 200CF microscope equipped with a cold-FEG electron source, operating at 200 kV. Cross-sections of the samples for TEM analysis were obtained using a Helios NanoLab 650 Focused Ion Beam-scanning electron microscope (FIB).

2.3. Photoluminescence

The solutions for the optical measurements were prepared using purified water (extinction) or ethanol (photoluminescence and Raman spectroscopy).

Photoluminescence spectra were measured using an optical spectrometer (PTI QuantaMaster 8000 by Horiba) with a continuous Xe lamp and a photomultiplier sensitive in visible and near-infrared part of the spectrum (Hamamatsu R2658). Holographic reflection gratings blazed at 300 nm were used in the dual-stage excitation monochromator, and ruled gratings (500 nm blaze) in the single-stage emission monochromator. The spectra were measured in the wavelength range of 290–450 nm (corresponding to 3.1–4.3 eV) at nominal resolution of 3 nm, with the excitation spectral band centered at 275 nm (4.51 eV). All presented spectra were corrected for spectral dependence of the instrument's excitation and emission channels.

2.4. Extinction measurements

Extinction measurements were performed with an UV–vis spectrometer (Perkin-Elmer lambda 950). The spectra were recorded with a 1 nm resolution. The solution was hand-shaken and the suspensions were measured using quartz cuvettes.

2.5. Raman scattering

The Raman scattering measurements were performed using a Tri Vista 557 Raman system in backscattering micro-Raman configuration. The 532 nm line of VerdiG solid-state (for platelets) and the 514.5 nm line of Ar^+/Kr^+ ion gas laser (for nanotiles and nanowires) were used as an excitation source. A microscope objective with ×100 magnification was used for focusing the laser beam and collecting scattered light. Laser power was kept below 0.5 mW at the sample surface, in order to minimize local heating. Spectra were recorded in parallel and crossed polarisation configuration. All measurements were performed in air, at room temperature. Spectra were corrected for the Bose factor.
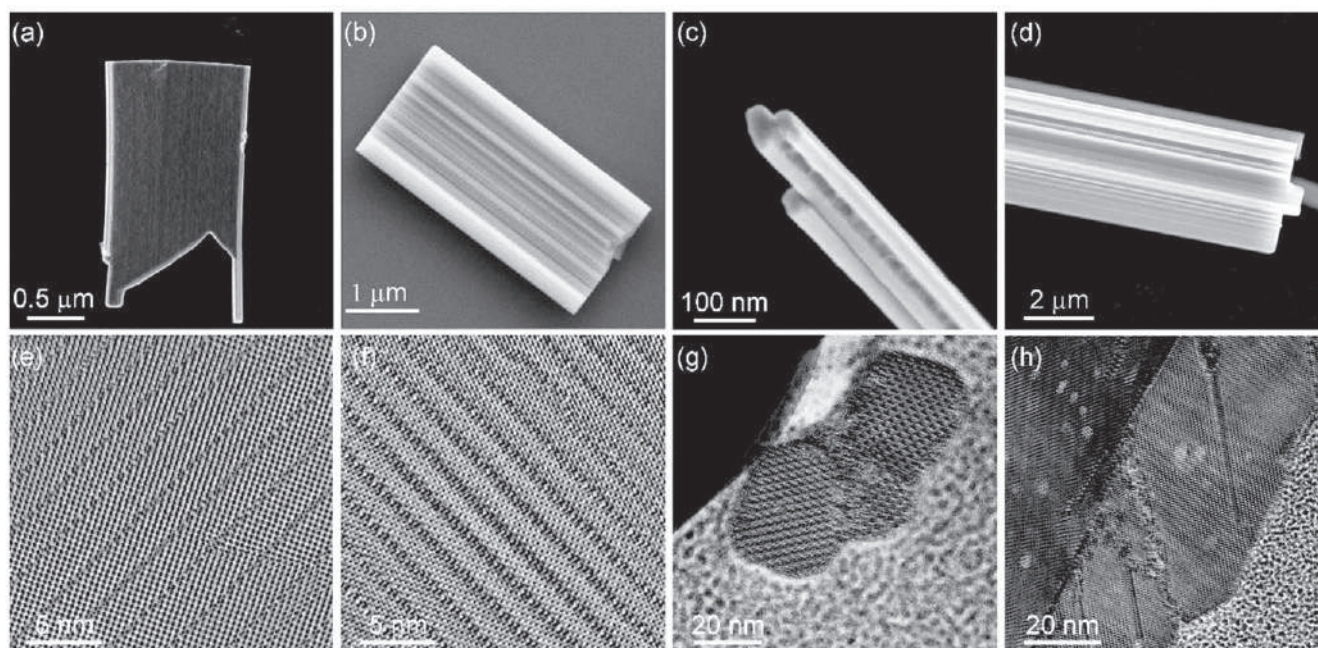
Figure 1. Electron microscopy images of (a), (e) platelets, (b), (f) nanotiles, (c), (g) W_5O_{14} NW and (d), (h) $W_{18}O_{49}$ NW. Top panel corresponds to SEM, while the bottom panel corresponds to TEM images.

Table 1. Stoichiometry of tungsten suboxide nanomaterials, their shape, thickness and lateral size (for 2D W_nO_{3n-1}) or *-diameter and length (for nanowires), and the assessed work function.

Stoichiometry	Shape	Thickness/diameter*	Lateral size/length*	Work function (eV)
W_nO_{3n-1}	Platelets	100 nm	Up to 4 μm	4.18–4.31
W_nO_{3n-1}	Nanotiles	100 nm	Up to several μm	4.94–5.30
W_5O_{14} ($WO_{2.8}$)	Nanowires	100–200 nm	Several tens μm	4.20–4.34
$W_{18}O_{49}$ ($WO_{2.72}$)	Nanowires	Up to 3 μm	Several tens μm	4.55–4.57

2.6. Kelvin probe force microscopy

The work function (WF) was measured with the Kelvin probe force microscopy (KPFM) method using a non-contact frequency-modulated atomic force microscope (NC-AFM, Omicron VT-AFM, Taunusstein, Germany) operating in ultra-high vacuum (10^{-9} mbar). The samples were dispersed in isopropanol and drop casted on a freshly cleaved highly oriented pyrolytic graphite (HOPG) substrate. The AFM and the KPFM images were taken simultaneously on the same area. KPFM was used to determine the WF of the samples by measuring the contact potential difference (CPD) between the substrate (HOPG) and the samples. As HOPG has a fairly stable WF value of 4.60 eV [38], it is commonly used as a reference material in KPFM measurements.

3. Results and discussion

3.1. Composition and morphology

The studied WO_{3-x} phases grow as thin plate-like crystals (platelets, nanotiles) or as nanowires (W_5O_{14}, $W_{18}O_{49}$). Figure 1 shows SEM and TEM images of the W_nO_{3n-1} platelets (a), (e) and nanotiles (b), (f); W_5O_{14} nanowires (c), (g), and $W_{18}O_{49}$ nanowires (d), (h). The stoichiometry and size of all four studied WO_{3-x} phases is summarized in table 1.

The W_nO_{3n-1} platelets grow epitaxially from $W_{19}O_{55}$ nanowires. These nanowires can either get detached from the platelets by mild sonication, or remain at the long edge of the platelet, as seen in figure 1(a). The platelets grow in a rectangular geometry and are approximately 100 nm thick with the lateral size of up to 4 μm. Several W_nO_{3n-1} Magnèli phases, such as $W_{18}O_{53}$ ($WO_{2.944}$), $W_{17}O_{50}$ ($WO_{2.941}$), $W_{16}O_{47}$ ($WO_{2.938}$), $W_{15}O_{44}$ ($WO_{2.933}$), $W_{14}O_{41}$ ($WO_{2.929}$), W_9O_{26} ($WO_{2.889}$) and $W_{10}O_{29}$ ($WO_{2.9}$), were found within a single platelet [36].

The nanotiles with the length and width up to a few μm are approximately 100 nm thick. They have characteristic surface corrugations that can be several tens of nm deep. They are multi-stoichiometric, with six distinct stoichiometries within a single nanotile: $W_{16}O_{47}$ ($WO_{2.938}$), $W_{15}O_{44}$ ($WO_{2.933}$), $W_{14}O_{41}$ ($WO_{2.928}$), $W_{13}O_{38}$ ($WO_{2.923}$), $W_{12}O_{35}$ ($WO_{2.917}$), and $W_{11}O_{32}$ ($WO_{2.909}$), all having the same W_nO_{3n-1} formula [37]. In both plate-like morphologies (i.e. nanotiles and platelets), CS planes are observed, as shown in
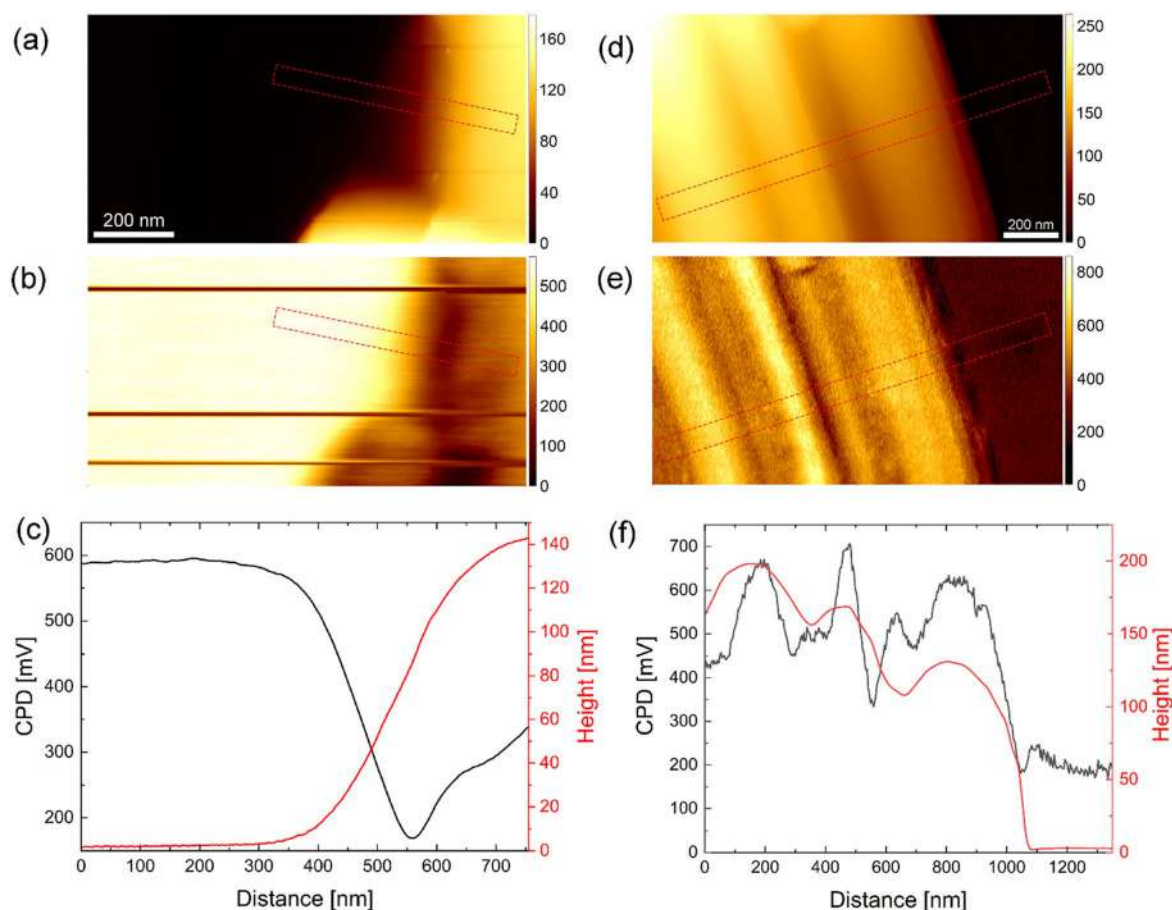
Figure 2. AFM (a), (d) and KPFM images (b), (e) of platelets and nanotiles, respectively. The CPD profiles and the matching thickness (c), (f) correspond to the areas marked with dashed rectangles.

figures 1(e), (f). The distance between the CS planes reflects the stoichiometry of a particular block.

Both W_5O_{14} and $W_{18}O_{49}$ nanowires have constant diameters along the lengths of several tens of μm. The W_5O_{14} NWs are thinner, with the mean diameter of 100–200 nm, while $W_{18}O_{49}$ NWs have significantly larger diameters of up to 3 μm, with rarely observed thin ones [35]. The cross-sectional views of such nanowires (figures 1(g), (h)) reveal that they are composed of several single-crystalline units.

3.2. Work function

The WF was measured on an individual WO_{3-x} nanotile or platelet. The results are compared with the previously published data obtained on the W_5O_{14} and $W_{18}O_{49}$ nanowires [35]. The topography and Kelvin images are shown in figure 2.

The platelet shown in figure 2(a) is around 140 nm thick. The CPD measured on the platelets was between 290 and 420 mV lower than on HOPG, corresponding to a WF of 4.18- 4.31 eV. Very similar WF values were reported earlier for W_5O_{14} nanowires (4.20–4.34 eV) [35]. On the other hand, the CPD obtained on the nanotiles was between 340 and 700 mV higher than on HOPG, indicating a WF of 4.94–5.30 eV. The WF of the nanotiles is thus substantially

higher compared to both W_5O_{14} and $W_{18}O_{49}$ nanowires (4.55–4.57 eV) [35].

The KPFM and AFM images also reveal that the WF is morphology dependent. In the case of platelets, the WF is slightly lower at the edge (figure 2(c)), similar to measurements performed on the edges of W_5O_{14} nanowires [35]. This might be due to the growth mechanism, as the platelets grow from nanowires [36], or due to band bending [39]. The WF of nanotiles also varies with location and was found to be lower inside the corrugations (figure 2(f)). The difference between the CPD at top and the bottom of the corrugation can be up to 350 meV. The summarized positions of WF values are presented in table 2.

3.3. Optical properties

3.3.1. Raman spectroscopy. Raman spectra of WO_{3-x} nanomaterials can be tentatively divided into three regions, characterized by the peaks originating from different types of vibrations. Lattice modes generally appear below 200 cm^{-1}, W–O–W bending modes between approximately 200 and 400 cm^{-1}, whereas between 600 and 900 cm^{-1} one can observe W–O stretching modes [40, 41]. Figure 3 represents room temperature Raman spectra of WO_{3-x} nanostructures measured in three polarization
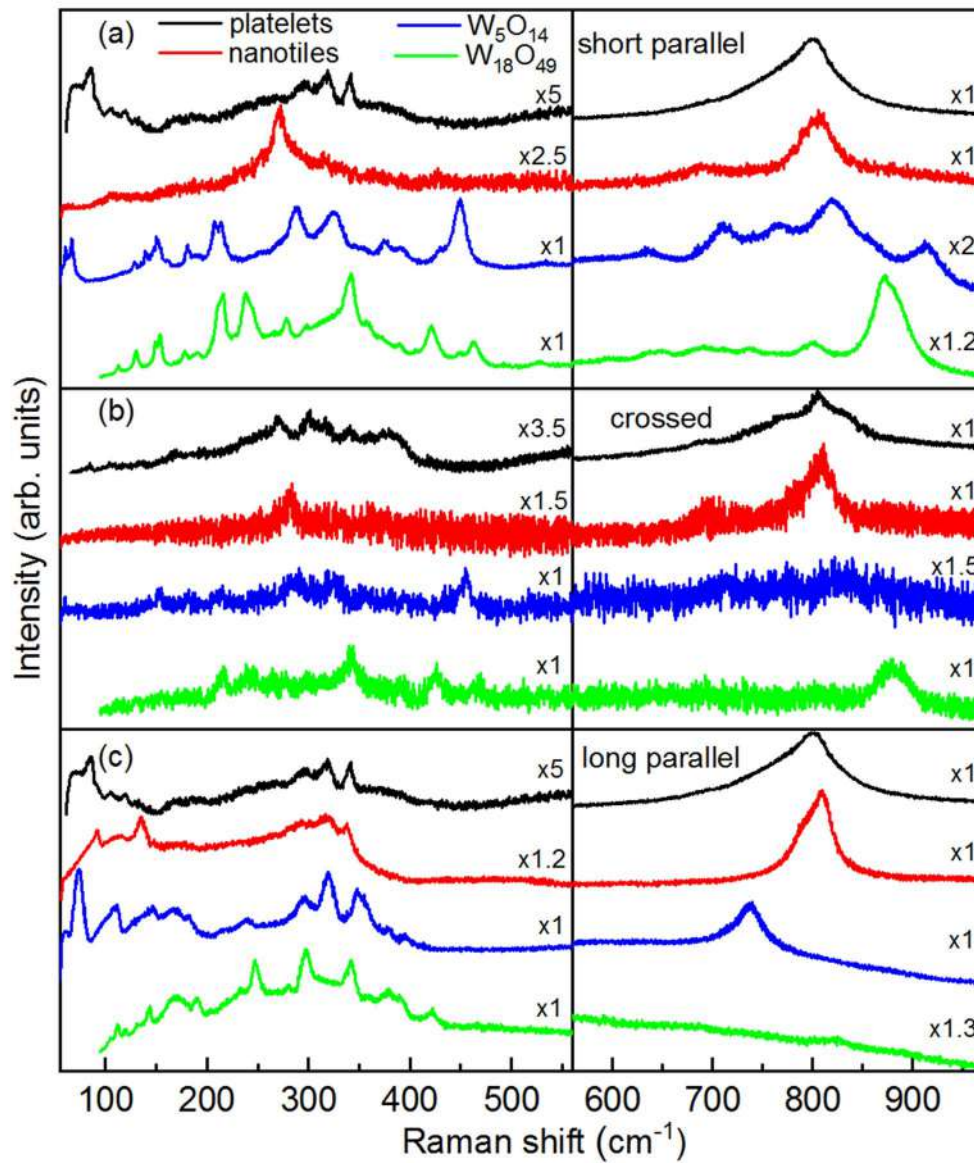
Figure 3. Raman scattering spectra of WO_{3-x} nanostructures measured at room temperature in three polarization configurations: (a) parallel, with incident and scattered light polarized along the short axis of the samples (short parallel configuration), (b) crossed, and (c) parallel, with incident and scattered light polarized along the long axis of the samples (long parallel configuration). For clarity, lower and higher-energy ranges are displayed with different scale factors.

Table 2. Summary of the assessed absorption and PL transitions, bandgap and work function values in tungsten suboxide nanomaterials.

	W_nO_{3n-1} platelets	W_nO_{3n-1} nanotiles	W_5O_{14} ($WO_{2.8}$)	$W_{18}O_{49}$ ($WO_{2.72}$)
UV–vis (nm)	207, 222, 241, 281, 323	205, 216, 240, 281, 324, 416	200, 223, 258, 326, 760	198, 208, 296, 776
PL (nm)	299, 323	302, 316	298, 324	299, 319
Bandgap (direct) (eV (nm))	4.11 (301)	4.05 (306)		
Bandgap (indirect) (eV (nm))	3.76 (330), 3.17 (391)	3.48 (356), 2.78 (446)	2.16 (574)	2.62 (473)
WF (eV)	4.18–4.31	4.94–5.30	4.20–4.34	4.55– 4.57
Average WF (eV)	4.25	5.12	4.27	4.56

configurations: short and long parallel, with incident and scattered light polarized along short and long axis of the sample respectively; and crossed, with polarisations parallel to the short and long axis of the sample but mutually orthogonal. In the case of the platelets, short and long parallel configurations are equivalent due to their symmetry.

Therefore, only two spectra were sufficient to observe all prominent modes noted in [36].

In platelets' crossed polarization configuration spectrum, there are four weak peaks, at 85, 105, 130 and 165 cm^{-1} related to lattice vibration, six peaks centred at 235, 271, 300, 319, 340 and 380 cm^{-1}, originating from W–O–W bending vibrations and one weak (690 cm^{-1}) and two strong (778 and 808 cm^{-1}) W–O stretching vibrations. In parallel configuration, one can observe few relatively weak peaks, at 85, 105, 120, 130, 297, 319 and 340 cm^{-1}, and two sharp overlapped peaks at 778 and 802 cm^{-1}. These results are in very good agreement with those from [36].

In the case of the nanotiles' short parallel polarization spectrum, only one weak peak (105 cm^{-1}) originating from lattice vibration, one strong peak at 271 cm^{-1}, a few weak peaks (at 231, 317, 331, 365 and 428 cm^{-1}) in the W–O–W bending region, and two prominent W–O stretching vibrations centred at 697 and 807 cm^{-1} are observed. In the crossed scattering configuration one can recognize the three highest intensity modes from that were also observed in the short parallel polarization (at 271, 697 and 807 cm^{-1}), whereas spectrum in long parallel polarization contains sharper and more pronounced low energy peaks, indicating good crystallinity and well-defined W–O bond length. Closer inspection revealed eight peaks, at 92, 113, 135, 175, 294, 319, 338 and 807 cm^{-1}, with the two prominent ones at 135 and 807 cm^{-1}, coinciding with the results given in [37].

Raman spectra of nanowires are qualitatively different from those of quasi-2D materials. Namely, for W_5O_{14} NW, in short parallel polarization seven lattice (at 67, 129, 139, 151, 181, 208 and 214 cm^{-1}), six W–O–W bending (at 288, 325, 376, 391, 430 and 448 cm^{-1}) and five W–O stretching vibrations, centred around 635, 712, 767, 819 and 912 cm^{-1}, were observed. Crossed polarization revealed Raman peaks at 151, 181, 208, 288, 325, 448 and 712 cm^{-1}, whereas in long parallel polarization one can observe peaks at 73, 108, 147, 167, 181, 237, 297, 319, 350, 376, 394 and 737 cm^{-1}.

In the short parallel polarization, the $W_{18}O_{49}$ NW spectrum hosts a large number of peaks, at 113, 129, 149, 153, 178, 190, 211, 215, 238, 245, 278, 341, 358, 390, 422, 449, 463, 527, 644, 689, 737, 801, 871 and 882 cm^{-1}, some of which are overlapping. In crossed polarization configuration there are only a few peaks, centred at 211, 215, 238, 245, 341, 422, 463, 871 and 882 cm^{-1}, whereas the spectrum in the long parallel polarization contains modes at 113, 119, 131, 142, 168, 190, 232, 247, 280, 297, 341, 378, 390, 422 and 821 cm^{-1}. The peak positions of all four materials are summarized in tables S1–4 (available online at stacks.iop. org/NANO/33/275705/mmedia).

Unlike the spectra of the nanotiles and platelets, where the W–O stretching modes centred around 800 cm^{-1} are absolutely dominant, Raman spectra of the nanowires contain a large number of sharp peaks in the first two frequency regions, which are comparable or even more dominant than the ones from the stretching vibrations region. This indicates that 2D materials contain a higher number of W–O bonds with well-defined lengths, whereas W_5O_{14} and $W_{18}O_{49}$ nanowires have better crystallinity and higher number of
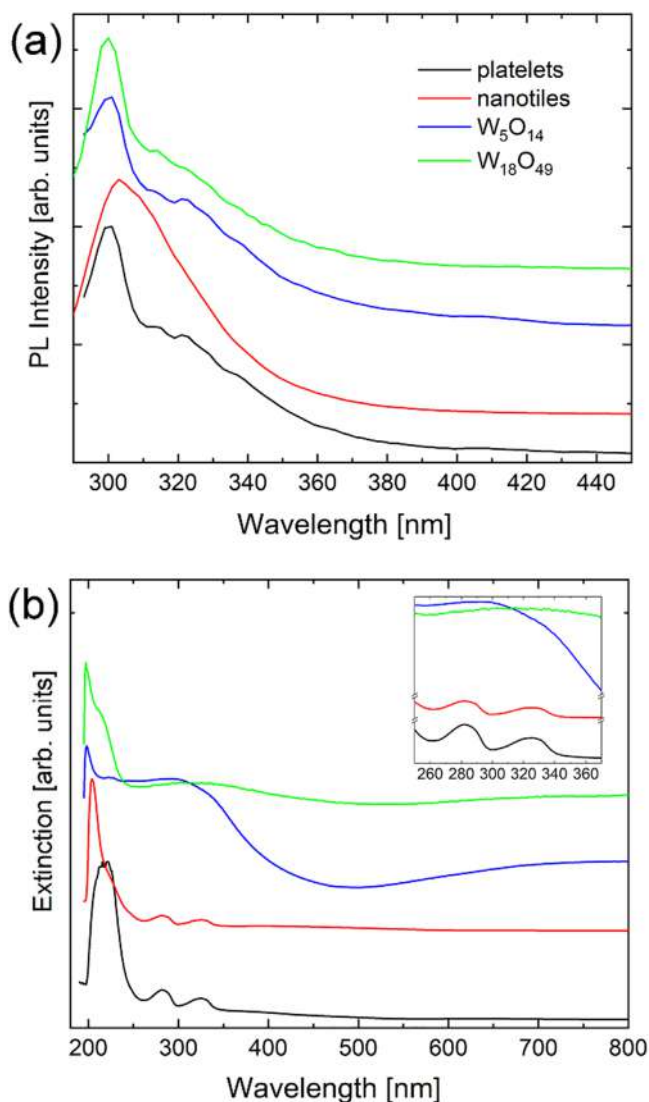
Figure 4. (a) Room temperature PL spectra and (b) UV–vis extinction spectra of platelets, nanotiles, W_5O_{14} and $W_{18}O_{49}$ nanowires.

W–O–W bonds with well-defined bond angles. The fact that spectra of all the analysed materials strongly depend on the sample orientation and light polarization unequivocally confirms their anisotropic structure.

3.3.2. Photoluminescence. In figure 4(a), the PL spectra of all four materials are presented, measured with the excitation centred at 275 nm (4.51 eV). The PL spectra were deconvolved, confirming that they contain two distinct emission lines in the UV region (figure S1). All of these suboxides have a dominant, high-energy peak situated around 300 nm (4.1 eV). An additional, red-shifted component appears in the 320 nm region (~3.9 eV), but its contribution varies. The positions of the PL peaks are summarized in table 2.

Because bulk WO_3 is an indirect band-gap semiconductor, its photoluminescence (PL) spectrum does not have any prominent features. In contrast, the appearance of new states in WO_{3-x} materials allows distinct optical transitions, often

associated with PL emission lines. Many studies were reported on PL activity of the substoichiometric oxides [42–49], and, in general, correlated the electronic transitions to the defect states within the band gap, arising from oxygen vacancies. The two processes guiding these transitions were assigned either to the occurrence of localized states in the bandgap, stemming from oxygen vacancies or other defects; or to a band-to-band transition, arising from the electron–hole recombination induced by quantum confinement. However, there is no general consensus on interpretation of the observed emissions, as the experimental reports differ and do not unambiguously assign the observed emissions to the proposed mechanisms.

Theoretical models show that an oxygen vacancy can be in three new states, namely in a neutral (V_O^0), single- (V_O^+), or double-charged (V_O^{2+}) [25, 27, 34]. Within these models, the removal of an O atom from WO_3 structure (ReO_3-type, W^{6+}–O^{2-}–W^{6+}) results in creation of a V_O^0 state. This corresponds to creation of either a W^{6+} + W^{4+} or $2W^{5+}$ defect states with levels inside or near the valence band (W^{4+}–V_O^0–W^{6+} or W^{5+}–V_O^0–W^{5+}) [25]. Removal of one additional electron, (i.e. conversion to V_O^+ (W^{5+})), leads to Coulombic repulsion between the positive vacancy and the nearest W-ion, displacing the ion and shifting the defect level into the bandgap (W^{5+}–V_O^+–W^{6+}). Removal of another electron creates a new state within the CB (W^{6+}–V_O^{2+}–W^{6+}). Therefore, the neutral state lies inside the valence band (VB), single-charged in the band gap, and the double-charged state inside the conduction band (CB). In other words, the W^{5+} states are shallow and can act as donor states, while electrons trapped in deeper states (W^{4+}) would need more energy to get excited into the CB. It is also important to note that the bandgap is closely related to the W–O bond length. When an O vacancy is introduced, structural relaxation of the lattice leads to an increase of the W–W distance. As the W ion gets displaced from the center of the WO_6 octahedron, the VB lowers and the CB rises, thus increasing the bandgap [50].

For PL spectra reported for $W_{18}O_{49}$ nanowires and nanorods, peaks appear in UV and blue spectral regions [31, 43, 45, 51]. For the nanorods, the peak located in the UV region blueshifts from 350 to 320 nm as the nanorod diameter decreases. This effect is assigned to quantum confinement, since the stoichiometry remains the same. The blue peak is situated around the absorption edge at 430 nm and does not show any size dependence, therefore it was assigned to the defect states within the bandgap [31].

Previously reported XPS measurements on these materials can provide more insight into origin of the transitions [29, 36, 37]. The valence band spectrum of the platelets indicates a semiconducting behaviour with a negligible density of states at the Fermi energy. On the other hand, the valence band spectrum of the nanotiles revealed a slightly metallic behaviour at room temperature due to a partial overlapping of a broad O 2p peak with W 5d orbitals [36, 37]. The W spectra confirm the presence of 5+ and 6+ oxidation states in both nanotiles and platelets. For the nanotiles, 6+ states represent 84% of the total W 4f, with the remaining 16% assigned to 5+, giving the average oxidation number of

5.84 and $3 - x$ value of 2.92. Similarly, the platelets spectrum is comprised of 81% of 6 + and 19% of 5+, with the oxidation number of 5.81 and $3 - x$ value of 2.91. These values are in great agreement with the stoichiometry deduced from the composition [36, 37]. Since the XPS measurements mainly correspond to the surface layers, these results confirm that the samples have no surface contaminations and that the additional defects do not accumulate at the surface layers. Similarly, 5+ and 6+ states have been observed for W_5O_{14} NW [29], while for the $W_{18}O_{49}$ NW, an additional 4+ state can appear [52, 53].

Focusing on the O 1s spectrum of nanotiles, platelets and W_5O_{14} NW, it can be observed that the peak at 533.5 eV is the most prominent for the platelets, the intensity decreases for NW while it is completely absent for the nanotiles. The WF values were increasing in the same order. This peak, together with the one at 532.0 eV, is attributed to O binding with W in lower oxidation states. HRTEM images shown in figure S3 reveal that the CS planes in the platelets appear parallel to the basal plane, which is still within the depth sensitivity of the XPS. On the other hand, the CS planes in the nanotiles are not close to the surface and are terminated in an unordered fashion, with the regular WO_3 dominating the surface. The effect of the oxidation state of the surface W can be of a great influence on the optical properties of these materials. Therefore, we can attribute the two observed emission bands in the UV to two electron–hole recombination processes, whereby the hole comes from the VB, while the electrons come from two resonant states within the CB, i.e. from two V_O^{2+} states [25, 48].

3.3.3. Extinction. As previously mentioned, both theoretical and experimental studies correlated oxygen vacancies and/or substoichiometric crystal structure to the appearance of defect states [27, 54, 55]. It was reported that up to $x = 0.1$, the optical and electrical properties of bulk WO_{3-x} are governed primarily by localized electrons involved in polarons [26]. The insulator-metal transition begins at $x = 0.1$, as the polaron wave functions start to overlap and form delocalized states [56]. As the x increases, free electrons start to dominate optical processes. In general, the indirect bandgap corresponds to the electronic transition from the filled O 2p orbitals at the top of the valence band to the empty W 5d orbitals in the conduction band [57]. Therefore, the absorption spectrum of WO_3 is essentially featureless until the photon energy reaches the bandgap value. Near the UV region, interband transitions start to take place and govern the optical properties [57].

Extinction (UV–vis) measurements, which include contributions of both absorbance and scattering processes, were performed on all four materials and the spectra are presented in figure 4(b). Although the samples were diluted in order to avoid the multi-scattering regime, the scattering effects in the near UV region cannot be completely excluded. The deconvolution of all the spectra has been performed and the positions of the individual peak contributions extracted, as shown in figure S2.

The most prominent transitions appear in the UVC range, with two contributions centred at 207 and 222 nm for the platelets and at 205 and 216 nm for the nanotiles, with another peak situated at 240 nm for both. Additionally, there are two prominent and closely positioned peaks, situated at 281 and 324 nm. These peaks may originate from exitonic transitions, as described later. A wide and less intense peak is also observed at 359 nm and 416 nm for the platelets and nanotiles, respectively. For both materials, the scattering is accounted for with a model function, as described in the SI.

On the other hand, the spectra of nanowires are significantly different compared to the quasi-2D materials. Both types of NWs have a high-energy peak around 200 nm. For $W_{18}O_{49}$ NWs, this peak can be deconvolved into two peaks positioned at 198 and 208 nm. $W_{18}O_{49}$ NWs spectrum has a higher-energy peak centred at 296 nm, ending with a broad transition at 776 nm. In addition to the peak at 200 nm, W_5O_{14} NWs have a very weak peak at 223 nm and an additional broad peak at approximately 300 nm, which can be deconvoluted into two peaks situated at 258 and 326 nm. An even broader peak appears at 760 nm in the near-IR part of the spectrum. The emergence of the near-IR peaks can be associated with LSPR due to free charge carriers. LSPR were observed previously in $W_{24}O_{68}$ ($WO_{2.83}$) and $W_{19}O_{55}$ ($WO_{2.89}$) nanorods, positioned at 900 nm and 600 nm, respectively [26, 55]. Assigning the near-IR tails to LSPR is also in agreement with earlier measurements on these NWs, which suggested metallic behaviour [29, 35].

Extinction spectra of these suboxides vary substantially in the literature, even within the same stoichiometry or morphology. For example, ultrathin (sub-nanometre) $W_{18}O_{49}$ ($WO_{2.72}$) nanowires show a large absorption tail in the visible part of the spectrum, which saturates upon oxidation [32, 51]. This effect points to the presence of a large number of oxygen vacancies or substoichiometric crystal structures. For the nanowires with larger diameter, the absorption in the visible and near-IR range drops. Nanorod bundles of the same stoichiometry have rather featureless spectra, with a steady decrease with increasing wavelength [31]. In the case of $W_{19}O_{55}$ ($WO_{2.89}$) nanorods, the extinction spectrum in UV–vis consists of one broad peak situated at 600 nm (2.07 eV) and a strong absorption band at 200–400 nm, similar to that seen in bulk WO_3 [55]. On the other hand, $W_{24}O_{68}$ ($WO_{2.83}$) nanorods support strong LSPRs, as evidenced by a broad peak centred around 900 nm [26]. WO_{3-x} reduced cubic nanosheets have a narrow peak around 220 nm, with a broader one centred around 300 nm [58]. The strong absorption in the long wavelength region is attributed to the new, oxygen vacancies-induced levels below the conduction band.

Qualitatively, the line shapes of the nanotiles and platelets spectra are similar to those of $WO_{2.9}$ ($W_{20}O_{58}$) nanoparticles [54] and WO_{3-x} quantum dots [59]. For the $WO_{2.9}$ NPs, the UV–vis spectrum consists of two shoulders at 220 and 265 nm, and a band at 320 nm with the bandgap estimated at 3.1 eV (400 nm). These NPs are also stoichiometrically the closest to platelets and nanotiles. Quantum dots have a high-intensity high-energy peak followed by broader

bands around 230 and 285 nm. Therefore, the two peaks found in the nanotiles and platelets and positioned at 281 and 323 nm are most likely a consequence of the crystal structure, i.e. the CS planes.

From the measured extinction spectra, direct and indirect optical bandgaps can be calculated using the equation [60]:

$$\alpha = \frac{A(h\nu - E_g)^n}{h\nu},$$

Here, α is the absorption coefficient, A is a constant, and E_g is the indirect bandgap for $n = 1/2$ and direct bandgap in the case of $n = 2$. The corresponding Tauc plots are presented in figure S4.

The optical bandgaps are highly sensitive to morphology and stoichiometry. In the literature, the measured optical bandgaps of bulk WO_3, bulk $WO_{2.9}$ and $WO_{2.9}$ nanowires were reported at 2.67 eV, 3.05 eV and 3.17 eV, respectively [3, 32]. For $W_{18}O_{49}$ nanorod bundles, the absorption edge is situated at 2.95 eV [31]. The decrease of the bandgap value of these nanorods by approximately 0.5 eV compared to that of the WO_3 nanoparticles of similar size (3.44 eV) [61] is assigned to the presence of new states correlated to the oxygen vacancies. The appearance of these new states can lead to the rise of two indirect absorption edges, as reported for the suboxide nanosheets (at 2.6 eV and 1.11 eV) [58]. In general, the optical bandgap of these nanostructured suboxides is governed by several different processes. The quantum confinement results in the increase of the bandgap, i.e. the smaller the particle, the larger the bandgap. A similar effect can be assigned also to the Burstein–Moss shift [62]. Namely, in the case of n-type metal oxide semiconductors, an increase of dopants (i.e. oxygen vacancies and W^{5+} atoms) shifts the absorption edge to higher energies due to filling states. Consequently, the measured bandgap, as determined from the onset of interband absorption, moves to higher energies (i.e. undergoes a blue shift). On the other hand, in heavily doped semiconductors, bandgap renormalization takes place. As the electrons start interacting with defects and impurities, their energy shifts due to a variety of effects, such as exchange interaction or Coulombic repulsion [63]. Consequently, the bandgap shrinks with increasing doping level, explaining the decrease of the band-gap with the increase of x [64]. The complex interplay of all these effects makes the value of the bandgap difficult to predict.

For both the nanotiles and platelets, an increase of the indirect bandgap is observed. However, there is an opening of another, lower energy bandgap. This bandgap appears as a consequence of the altered electronic structure due to bond length changes caused by oxygen vacancies and formation of CS planes with W atoms in lower oxidation states. The appearance of two indirect absorption edges was previously reported in suboxide nanosheets [58]. The two indirect bandgaps appear at 3.76 and 3.17 eV for the platelets and at 3.48 and 2.78 eV for the nanotiles. The former value can be assigned to the regular bandgap (between the VB and the CB), while the latter appears

between a new, defect-induced band and CB. The regular gap coincides with the transitions observed in the extinction spectra. These values lie in the upper range of the bandgaps reported in the literature, which is attributed to the distortions in the WO_6 octahedra in such substoichiometric materials [12, 24].

Nanowires show the indirect bandgap values of 2.16 and 2.62 eV for W_5O_{14} and $W_{18}O_{49}$, respectively. As these materials show LSPR fingerprints and therefore free charge carriers, their bandgap decreased with respect to WO_3.

The calculated direct optical bandgap is 4.11 eV (302 nm) for the platelets and 4.05 eV (306 nm) for the nanotiles. These values are in good agreement with the dominant PL peaks that are situated at 4.15 eV and 4.11 eV for the platelets and nanotiles, respectively. As discussed previously, both recorded PL bands are in the UV region, in the 3.9–4.2 eV range and can be assigned to two resonant states introduced by oxygen vacancies [27, 47]. Namely, an electron–hole pair forms an exciton near the oxygen vacancy. When an electron is excited to a state at or above the resonance, it can be trapped. The emission bands in the UV are thus attributed to electron–hole recombination, where the electron comes from one of the two resonant levels in the CB, while the hole occupies the VB. Therefore, the direct bandgap stems from optical transitions related to the defect states. These transitions and the corresponding bandgaps are at the same positions for nanotiles and platelets, confirming their similar stoichiometry. The bang gap values and extinction peak positions are presented in table 2.

4. Conclusions

Structural and optical properties of four different WO_{3-x} nanostructures with different morphologies and/or stoichiometries are presented. While the two quasi-2D materials show polycrystallinity, nanowires are of uniform W_5O_{14} and $W_{18}O_{49}$ composition. Raman spectra reveal that less oxidized W_xO_{3x-1} stoichiometries have higher number of W–O bonds with well-defined lengths, whereas more reduced tungsten suboxides have a higher number of W–O–W bonds with well-defined bond angles. The extinction spectra reveal the appearance of excitonic states for the less oxidized W_xO_{3x-1} stoichiometries and two indirect bandgaps deduced from the Tauc plots. Both values appear in the upper range reported for suboxide materials, which can be explained by the formation of oxygen vacancies. The extinction spectra of the more reduced tungsten suboxides show the presence of LSPR in the near-IR region. Their bandgaps are lower, as they have a higher number of free charge carriers, confirmed by the LSPR-like peaks. PL spectra reveal two distinct emission peaks in the UV range, present in all four nanomaterials. They are attributed to electron–hole recombination, with the hole stemming from the VB and electron from one of the resonant states within the CB. Furthermore, the effects of stoichiometry and CS planes are discussed in relation to the understanding of the optical properties.

Data availability statement

All data that support the findings of this study are included within the article (and any supplementary files).

ORCID iDs

Bojana Višić ● https://orcid.org/0000-0002-2065-0727
Luka Pirker ● https://orcid.org/0000-0003-0741-0048
Boris Majaron ● https://orcid.org/0000-0003-2841-8276
Maja Remškar ● https://orcid.org/0000-0002-8919-1768

References

[1] Mahjabin S *et al* 2021 Effects of oxygen concentration variation on the structural and optical properties of reactive sputtered WOx thin film *Sol. Energy* **222** 202–11
[2] Thummavichai K, Xia Y and Zhu Y 2017 Recent progress in chromogenic research of tungsten oxides towards energy-related applications *Prog. Mater. Sci.* **88** 281–324
[3] Huang Z F, Song J, Pan L, Zhang X, Wang L and Zou J J 2015 Tungsten oxides for photocatalysis, electrochemistry, and phototherapy *Adv. Mater.* **27** 5309–27
[4] Pirker L and Višić B 2021 Recent progress in the synthesis and potential applications of two-dimensional tungsten (Sub) oxides *Isr. J. Chem.* (https://doi.org/10.1002/ijch.202100074)
[5] Zhang X, Wei Y and Yu R 2022 Multi-dimensional tungsten oxides for efficient solar energy conversion *Small Structures* **3** 2100130
[6] Liu J, Zhong M, Li J, Pan A and Zhu X 2015 Few-layer WO_3 nanosheets for high-performance UV-photodetectors *Mater. Lett.* **148** 184–7
[7] He Z, Liu Q, Hou H, Gao F, Tang B and Yang W 2015 Tailored electrospinning of WO_3 nanobelts as efficient ultraviolet photodetectors with photo-dark current ratios up to 1000 *ACS Appl. Mater. Interfaces* **7** 10878–85
[8] Aguir K, Lemire C and Lollman D 2002 Electrical properties of reactively sputtered WO_3 thin films as ozone gas sensor *Sensors Actuators* B **84** 1–5
[9] Zhang C *et al* 2011 Highly sensitive hydrogen sensors based on co-sputtered platinum-activated tungsten oxide films *Int. J. Hydrogen Energy* **36** 1107–14
[10] Hariharan V, Gnanavel B, Sathiyapriya R and Aroulmoji V 2019 A review on tungsten oxide (WO_3) and their derivatives for sensor applications *Int. J. Adv. Sci. Eng.* **5** 1163–8

[11] Sayama K, Mukasa K, Abe R, Abe Y and Arakawa H 2001 Stoichiometric water splitting into H2 and O2 using a mixture of two different photocatalysts and an IO3−/I− shuttle redox mediator under visible light irradiation *Chem. Commun.* **23** 2416–7

[12] Wang G, Ling Y and Li Y 2012 Oxygen-deficient metal oxide nanostructures for photoelectrochemical water oxidation and other applications *Nanoscale.* **4** 6682–91

[13] Miyazaki H, Ishigaki T and Ota T 2017 Photochromic smart windows employing WO$_3$-based composite films *J. Mater. Sci. Res.* **6** 62–6

[14] Hai Z, Wei Z, Xue C, Xu H and Verpoort F 2019 Nanostructured tungsten oxide thin film devices: from optoelectronics and ionics to iontronics *J. Mater. Chem.* C **7** 12968–90

[15] Granqvist C G 2000 Electrochromic tungsten oxide films: review of progress 1993–1998 *Sol. Energy Mater. Sol. Cells* **60** 201–62

[16] González-Borrero P *et al* 2010 Optical band-gap determination of nanostructured WO$_3$ film *Appl. Phys. Lett.* **96** 061909

[17] He T and Yao J 2007 Photochromic materials based on tungsten oxide *J. Mater. Chem.* **17** 4547–57

[18] Zheng H, Ou J Z, Strano M S, Kaner R B, Mitchell A and Kalantar-zadeh K 2011 Nanostructured tungsten oxide–properties, synthesis, and applications *Adv. Funct. Mater.* **21** 2175–96

[19] Polaczek A, Pekala M and Obuszko Z 1994 Magnetic susceptibility and thermoelectric power of tungsten intermediary oxides *J. Phys.:Condens. Matter* **6** 7909

[20] Tilley R 1970 The formation of shear structures in sub-stoichiometric tungsten trioxide *Mater. Res. Bull.* **5** 813–23

[21] Pickering R and Tilley R 1976 An electron microscope study of tungsten oxides in the composition range WO$_2$. 90 · WO$_2$. 72 *J. Solid State Chem.* **16** 247–55

[22] Magnéli A 1953 Structures of the ReO$_3$-type with recurrent dislocations of atoms: homologous series' of molybdenum and tungsten oxides *Acta Crystallogr.* **6** 495–500

[23] Lundberg M, Sundberg M and Magnéli A 1982 The 'pentagonal column' as a building unit in crystal and defect structures of some groups of transition metal compounds *J. Solid State Chem.* **44** 32–40

[24] Mohamed A M, Amer A W, AlQaradawi S Y and Allam N K 2016 On the nature of defect states in tungstate nanoflake arrays as promising photoanodes in solar fuel cells *Phys. Chem. Chem. Phys.* **18** 22217–23

[25] Deb S K 2008 Opportunities and challenges in science and technology of WO$_3$ for electrochromic and related applications *Sol. Energy Mater. Sol. Cells* **92** 245–58

[26] Manthiram K and Alivisatos A P 2012 Tunable localized surface plasmon resonances in tungsten oxide nanocrystals *JACS* **134** 3995–8

[27] Karazhanov S Z, Zhang Y, Mascarenhas A, Deb S and Wang L-W 2003 Oxygen vacancy in cubic WO$_3$ studied by first-principles pseudopotential calculation *Solid State Ionics* **165** 43–9

[28] Migas D, Shaposhnikov V and Borisenko V 2010 Tungsten oxides. II. The metallic nature of Magnéli phases *J. Appl. Phys.* **108** 093714

[29] Remškar M, Kovac J, Viršek M, Mrak M, Jesih A and Seabaugh A 2007 W$_5$O$_{14}$ nanowires *Adv. Funct. Mater.* **17** 1974–8

[30] Shi S, Xue X, Feng P, Liu Y, Zhao H and Wang T 2008 Low-temperature synthesis and electrical transport properties of W$_{18}$O$_{49}$ nanowires *J. Cryst. Growth* **310** 462–6

[31] Su C-Y and Lin H-C 2009 Direct route to tungsten oxide nanorod bundles: microstructures and electro-optical properties *J. Phys. Chem.* C **113** 4042–6

[32] Paik T *et al* 2018 Photocatalytic hydrogen evolution from substoichiometric colloidal WO$_{3−x}$ nanowires *ACS Energy Lett.* **3** 1904–10

[33] Song K, Liu X, Tian C, Deng H, Wang J and Su X 2019 Oxygen defect-rich WO$_{3−x}$ nanostructures with high photocatalytic activity for dehydration of isopropyl alcohol to propylene *Surf. Interfaces* **14** 245–50

[34] Wang F, Di Valentin C and Pacchioni G 2011 Semiconductor-to-metal transition in WO$_{3−x}$: nature of the oxygen vacancy *Phys. Rev.* B **84** 073103

[35] Saqib M *et al* 2020 Field emission properties of single crystalline W$_5$O$_{14}$ and W$_{18}$O$_{49}$ nanowires *J. Electron. Spectrosc. Relat. Phenom.* **241** 146837

[36] Pirker L, Višić B, Škapin S D, Dražić G, Kovač J and Remškar M 2020 Multi-stoichiometric quasi-two-dimensional W$_n$ O $3n−$ 1 tungsten oxides *Nanoscale.* **12** 15102–14

[37] Pirker L, Višić B, Kovač J, Škapin S D and Remškar M 2021 Synthesis and characterization of tungsten suboxide WnO3n − 1 nanotiles *Nanomaterials.* **11** 1985

[38] Maeda F, Takahashi T, Ohsawa H, Suzuki S and Suematsu H 1988 Unoccupied-electronic-band structure of graphite studied by angle-resolved secondary-electron emission and inverse photoemission *Phys. Rev.* B **37** 4482

[39] Lanzoni E M *et al* 2021 The impact of Kelvin probe force microscopy operation modes and environment on grain boundary band bending in perovskite and Cu (In, Ga) Se2 solar cells *Nano Energy* **88** 106270

[40] Daniel M, Desbat B, Lassegues J, Gerand B and Figlarz M 1987 Infrared and Raman study of WO$_3$ tungsten trioxides and WO$_3$, xH$_2$O tungsten trioxide tydrates *J. Solid State Chem.* **67** 235–47

[41] Hardcastle F D and Wachs I E 1995 Determination of the molecular structures of tungstates by Raman spectroscopy *J. Raman Spectrosc.* **26** 397–405

[42] Johansson M B, Zietz B, Niklasson G A and Österlund L 2014 Optical properties of nanocrystalline WO$_3$ and WO$_{3−x}$ thin films prepared by DC magnetron sputtering *J. Appl. Phys.* **115** 213510

[43] Lee K, Seo W S and Park J T 2003 Synthesis and optical properties of colloidal tungsten oxide nanorods *JACS* **125** 3408–9

[44] Feng M *et al* 2005 Strong photoluminescence of nanostructured crystalline tungsten oxide thin films *Appl. Phys. Lett.* **86** 141901

[45] Hong K, Xie M, Hu R and Wu H 2007 Synthesizing tungsten oxide nanowires by a thermal evaporation method *Appl. Phys. Lett.* **90** 173121

[46] Wang J, Lee P S and Ma J 2009 Synthesis, growth mechanism and room-temperature blue luminescence emission of uniform WO$_3$ nanosheets with W as starting material *J. Cryst. Growth* **311** 316–9

[47] Luo J Y, Xu N S, Zhao F L, Deng S Z and Tao Y T 2011 Ultraviolet superfluorescence from oxygen vacancies in WO$_{3−x}$ nanowires at room temperature *J. Appl. Phys.* **109** 024312

[48] Wang B, Zhong X, He C, Zhang B, Cvelbar U and Ostrikov K 2021 Nanostructure conversion and enhanced photoluminescence of vacancy engineered substoichiometric tungsten oxide nanomaterials *Mater. Chem. Phys.* **262** 124311

[49] Wang D *et al* 2013 High-performance gas sensing achieved by mesoporous tungsten oxide mesocrystals with increased oxygen vacancies *J. Mater. Chem.* A **1** 8653–7

[50] Walkingshaw A D, Spaldin N A and Artacho E 2004 Density-functional study of charge doping in WO$_3$ *Phys. Rev.* B **70** 165110

[51] Xi G *et al* 2012 Ultrathin W18O49 nanowires with diameters below 1 nm: synthesis, near-infrared absorption,

photoluminescence, and photochemical reduction of carbon dioxide *Angew. Chem. Int. Ed.* **51** 2395–9

[52] Guo C, Yin S, Dong Q and Sato T 2012 The near infrared absorption properties of $W_{18}O_{49}$ *RSC Adv.* **2** 5041–3

[53] Guo C, Yin S, Yan M, Kobayashi M, Kakihana M and Sato T 2012 Morphology-controlled synthesis of $W_{18}O_{49}$ nanostructures and their near-infrared absorption properties *Inorg. Chem.* **51** 4763–71

[54] Barreca F, Acacia N, Spadaro S, Curro G and Neri F 2011 Tungsten trioxide (WO_{3-x}) nanoparticles prepared by pulsed laser ablation in water *Mater. Chem. Phys.* **127** 197–202

[55] Qian J, Zhao Z, Shen Z, Zhang G, Peng Z and Fu X 2016 Oxide vacancies enhanced visible active photocatalytic W 19 O 55 NMRs via strong adsorption *RSC Adv.* **6** 8061–9

[56] Salje E and Güttler B 1984 Anderson transition and intermediate polaron formation in WO_{3-x} Transport properties and optical absorption *Philos. Mag.* B **50** 607–20

[57] Hjelm A, Granqvist C G and Wills J M 1996 Electronic structure and optical properties of WO_3, $LiWO_3$, $NaWO_3$, and HWO_3 *Phys. Rev.* B **54** 2436

[58] Fang Z *et al* 2017 Synthesis of reduced cubic phase WO_{3-x} nanosheet by direct reduction of $H_2WO_4 \cdot H_2O$ *Mater. Today Energy* **6** 146–53

[59] Wang Y *et al* 2017 Simultaneous synthesis of WO_{3-x} quantum dots and bundle-like nanowires using a one-pot template-free solvothermal strategy and their versatile applications *Small* **13** 1603689

[60] Pankove J I 1971 *Optical Processes in Semi-Conductors* (Mineola, NY: Dover Publications, Inc)

[61] He T *et al* 2002 Photochromism of WO_3 colloids combined with TiO_2 nanoparticles *J. Phys. Chem.* B **106** 12670–6

[62] Sarkar A, Ghosh S, Chaudhuri S and Pal A 1991 Studies on electron transport properties and the Burstein-Moss shift in indium-doped ZnO films *Thin Solid Films* **204** 255–64

[63] Walsh A, Da Silva J L and Wei S-H 2008 Origins of band-gap renormalization in degenerately doped semiconductors *Phys. Rev.* B **78** 075211

[64] Smith W, Zhang Z-Y and Zhao Y-P 2007 Structural and optical characterization of WO_3 nanorods/films prepared by oblique angle deposition *J. Vac. Sci. Technol.* B **25** 1875–81

Contents lists available at ScienceDirect

Applied Surface Science
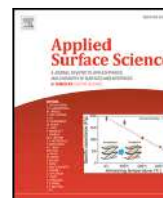
Full length article

Natural two-dimensional pyrophyllite: Nanoscale lubricant, electrical insulator and easily-machinable material

Borislav Vasić [a],[*], Radoš Gajić [a], Ivana Milošević [a], Žarko Medić [a], Marina Blagojev [b], Marko Opačić [a], Aleksandar Kremenović [c], Dejan Lazić [d]

[a] *Institute of Physics Belgrade, University of Belgrade, Pregrevica 118, 11080 Belgrade, Serbia*
[b] *Faculty of Mining and Geology, University of Belgrade, Đušina 7, 11000 Belgrade, Serbia*
[c] *Laboratory of Crystallography, Faculty of Mining and Geology, University of Belgrade, Đušina 7, 11000 Belgrade, Serbia*
[d] *Biotech Engineering D.O.O, Golsvordijeva 32, 11000 Belgrade, Serbia*

ARTICLE INFO

ABSTRACT

Pyrophyllite, with the chemical formula $Al_2Si_4O_{10}(OH)_2$, is a naturally occurring and abundant van der Waals mineral belonging to the group of phyllosilicates. It is very soft, layered crystal used for sculpting and an excellent electrical and thermal insulator aimed for the operation at high pressure and temperature. Here, for the first time, two-dimensional (2D) pyrophyllite obtained by both mechanical and liquid phase exfoliation is presented and investigated at the nanoscale. The layered structure provides low friction coefficient of around 0.1 as measured by friction force microscopy. The wear properties, studied by atomic force microscope (AFM) based scratching, are distinctly different from graphene. Since the wear is initiated at low normal forces, 2D pyrophyllite can be routinely carved by the AFM tip and it is suitable for scratching based nanolithography. According to our optical measurements, 2D pyrophillite is an insulator with a band gap of ~ 5.2 eV. Local current measurements by conductive AFM reveal that 2D pyrophyllite flakes behave as efficient electrical insulators with a breakdown voltage of around 6 MV/cm. Therefore, the obtained results indicate possible applications of 2D pyrophyllite as a low-cost electric insulator and lubricant, as well as an easily-machinable material at the nanoscale.

1. Introduction

Layered materials are usually defined as a special crystal class existing in the form of weakly stacked atomic layers, like graphene in graphite. General property of these materials are the strong in-plane bonds and very weak interactions perpendicular to the planes, typically of the van der Waals type. Therefore, layered materials that can be exfoliated into atomically thin layers are often called van der Waals materials. Two dimensional (2D) materials concerns crystalline solids consisting of a single or few atomic layers. Huge interest for them started when large graphene flakes were isolated for the first time in 2004 by Novoselov et al. using mechanical exfoliation [1]. Extraordinary properties of graphene [2] triggered the search for new 2D materials. Nowadays hundreds of different 2D materials beyond graphene have been devised and thoroughly investigated because of their extraordinary properties that are not present in corresponding counterpart bulk materials. As a result, 2D materials find numerous applications in nanoelectronics, nanophotonics and optoelectronics, spintronics, sensing and many other fields [3–5].

After the discovery of graphene, the second generation of 2D materials, which includes hexagonal boron nitride, 2D transition metal dichalcogenides (such as MoS_2, WS_2, $MoSe_2$, WSe_2, $MoTe_2$) and functionalized graphene, quickly appeared [6–11]. The third-generation of 2D materials includes elemental analogues of graphene such as silicene, germanene, stanene, phosphorene [12], as well as with 2D transition metal carbides and carbonitrides (MXenes) [13], 2D silicon dioxide [14], and minerals [15]. Interestingly, many of them were firstly discovered by numerical calculations, and afterwards, experimentally obtained [16].

The most of 2D materials are synthetic, for instance large-scale 2D materials are commonly prepared by chemical vapour deposition. On the other hand, natural van der Waals minerals exist in most classes of 2D materials like semi-metallic graphite and semiconducting molybdenite MoS_2 and tungstenite WS_2. In recent years, a new family of 2D materials has appeared. It is based on layered natural minerals as a source of 2D materials [15]. This family includes 2D insulating materials based on phyllosilicates such as talc [18–24], muscovite (mica) [25],

* Corresponding author.
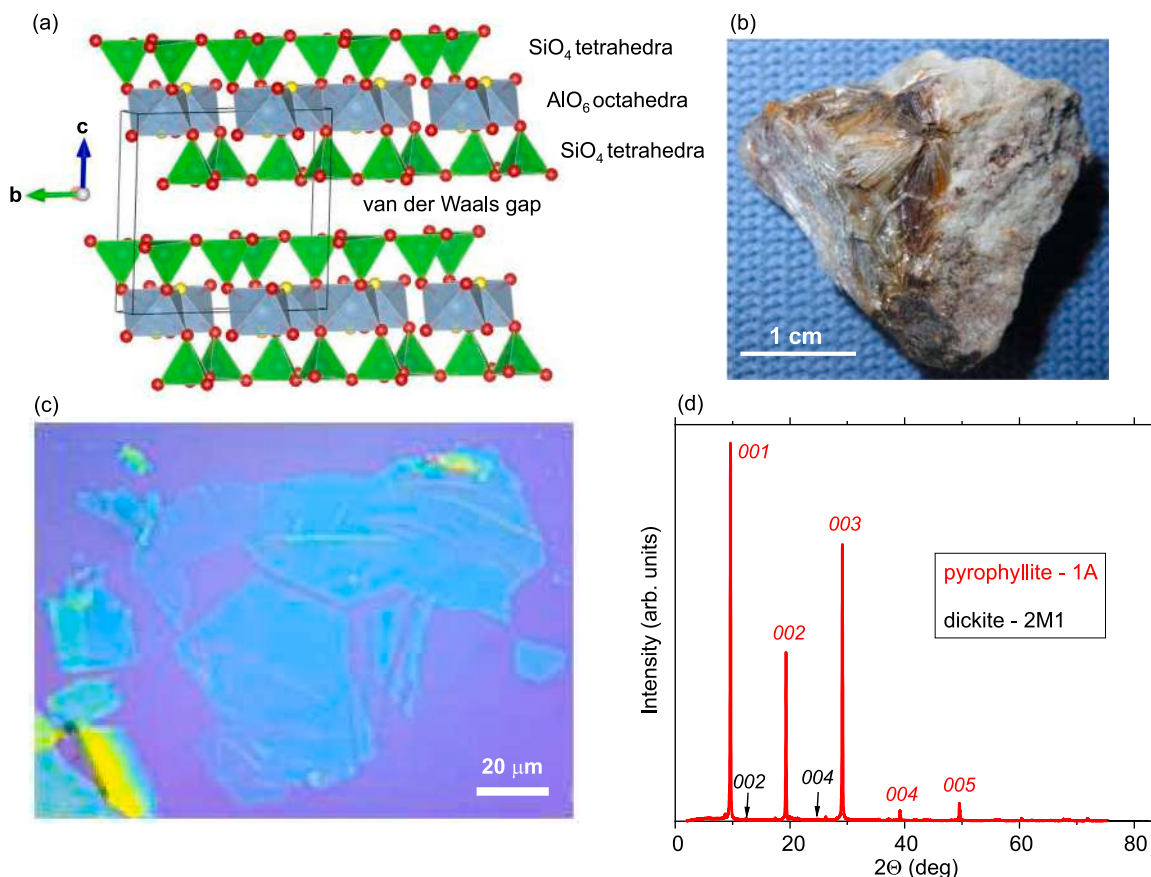*E-mail address:* bvasic@ipb.ac.rs (B. Vasić).

Fig. 1. (a) Polyhedral representation of pyrophyllite-1A structure: SiO$_4$ tetrahedra in green, AlO$_6$ octahedra in blue, oxygen atoms in red, OH group in yellow. The unit cell is outlined in black. VESTA program [17] was used for three-dimensional visualization of the crystal structure. (b) Optical image of the crystalline pyrophyllite used in this study. (c) Optical micrograph of mechanically exfoliated 2D pyrophillite flakes. (d) XRPD pattern of bulk pyrophyllite crystal which contains pyrophyllite-1A (PDF card # 01-075-0856) and small amount (near detection limit) of dickite-2M1 (PDF card # 00-058-2002). Most intense *hkl* reflections are marked.

biotite [26], vermiculite [27], clinochlore [28], and phlogopite [29], as well as 2D magnetic materials such as cylindrite [30] and iron-rich talc [31]. Furthermore, semiconducting van der Waals mineral franckeite has been used for the exfoliation of 2D van der Waals heterostructures [32–34]. Therefore, 2D materials can be obtained directly from natural minerals by just simple exfoliation and without complex synthetic procedures. As a result, search of 2D materials among natural minerals can be particularly interesting. Furthermore, clay minerals are abundant in Earth crust and therefore they serve as cost-effective sources of 2D materials. This mainly concerns phyllosilicates or layered silicates such as talc, pyrophyllte, kaolinite, gibbsite, etc., which are the most common and abundant clays.

Pyrophyllite (from Greek pyro—fire and phyllos—a leaf) is natural van der Waals mineral which belongs to the talc–pyrophyllite family of phyllosilicates. It is a hydrous aluminum silicate with the chemical formula Al$_2$Si$_4$O$_{10}$(OH)$_2$. Single layer of pyrophyllite consists of the AlO$_6$ octahedral sheet sandwiched between two SiO$_4$ tetrahedral layers (Fig. 1(a). Pyrophyllite is a chemically inert material, good electrical and thermal insulator with a high melting point [35] and with a fairly high dielectric constant [36,37]. As a clay mineral, it is abundant and inexpensive. Therefore, it is widely used in refractories, high-grade ceramics, electric insulators, and as a filler in order to improve properties of paper, plastic, rubber, paint and other mixtures [35]. As a van der Waals material, pyrophyllite has a lamellar structure which indicates good frictional properties and its applications as a lubricant [38]. It is very soft mineral [35] which provides easy machining and making of various profiles, while at the same time, it can withstand large pressures. Therefore, bulk pyrophyllite mineral exhibits interesting properties with a broad range of potential applications. Still,

its 2D form has not been studied so far, although small flakes of few layer pyrophyllite have been obtained by liquid phase exfoliation [39], whereas thermal exfoliation was investigated as well [40], but not in the context of 2D layers.

Here we present our report on 2D pyrophyllite with the focus on its properties related to potential applications as 2D electric insulator, lubricant and material suitable for nanolithography. Using mechanical and liquid phase exfoliation (LPE), we routinely fabricated few-layer pyrophyllite which can be exfoliated down to single-layer thickness. The initial characterization was done by X-ray powder diffraction (XRPD), Raman spectroscopy, UV–VIS spectroscopy, and optical microscopy. Afterwards, we focused on nanoscale mechanical and electrical properties of 2D pyrophyllite such as friction, wear, nanoscale machining, as well as insulating properties and dielectric breakdown, which were investigated by atomic force microscopy (AFM) based methods.

2. Experimental methods

2.1. Sample preparation

Here we used the crystalline pyrophyllite from Hillsborough, Orange County, North Carolina, USA (Fig. 1(b)). 2D pyrophyllite flakes were obtained by the mechanical exfoliation [41] onto SiO$_2$/Si substrate (with 300 nm thick SiO$_2$). Briefly, thick pyrophyllite flakes were separated from the bulk crystal by an adhesive tape. These flakes were further thinned by multiple peeling against two pieces of the tape, and finally transferred onto the substrate. The flakes of interest were selected by optical microscopy (typical optical micrograph depicted in Fig. 1(c)).

The starting material for LPE of pyrophyllite was ground pyrophyllite crystal (Hillsborough mine, Orange County, North Carolina, USA). Its dispersion was obtained in N-N-Dimethylformamide (DMF, Sigma Aldrich, product no. D4551), while the initial concentration of pyrophillite was 10 mg/mL (in 10 mL cylindrical vial). The solution was then sonicated in a low-power ultrasonic bath for 12 h. The resulting yellowish dispersion was centrifuged for 15 min at 1000 rpm. In order to fabricate pyrophyllite films from the obtained dispersion, Langmuir–Blodgett Assembly (LBA) technique at a water–air interface was used. This technique was previously employed for the preparation of graphene films as well [42,43]. In the first step, a small amount of pyrophyllite dispersion in DMF was added at the water–air interface. Then, after the pyrophyllite film was formed at the interface, it was slowly picked up by desired substrate. Three different substrates were used: SiO_2/Si for AFM measurements (morphological characterization), Au-coated SiO_2/Si for C-AFM measurements (current maps and breakdown voltage), and quartz for UV–VIS spectroscopy.

2.2. XRPD measurements, Raman and UV–VIS spectroscopy

The structural characterization was done by XRPD which was conducted at room temperature on Rigaku Smartlab X-ray Diffractometer in $\theta-\theta$ geometry (the sample in the horizontal position) in parafocusing Bragg–Brentano geometry using D/teX Ultra 250 strip detector in 1D standard mode with $CuK\alpha_{1,2}$ radiation source (U = 40 kV and I = 30 mA). The XRPD pattern was collected in $2-90°$ 2θ range, with the step of $0.01°$, and data collection speed of $6°/min$. The pyrophyllite sample was spinning in the horizontal plane with the speed of 60 rounds per minute. The low background single crystal silicon sample holder was used to minimize the background. The PDXL2 integrated XRPD software (Version 2.8.30; Rigaku Corporation) was employed for XRPD data treatment.

Raman scattering measurements were performed on Tri Vista 557 Raman system, in backscattering micro-Raman configuration. The 514.5 nm line of an Ar^+/Kr^+ gas laser was used as an excitation source. Laser power was less than 1 mW on a sample in order to minimize its local heating. A microscope objective with the 50x magnification was used for focusing the laser beam. All measurements were performed at ambient conditions.

Optical transmittance of the pyrophyllite film (obtained by liquid phase exfoliation) was measured by ultraviolet–visible (UV–VIS) spectrophotometer Beckman Coulter DU 720 in the range from 200 to 900 nm.

2.3. AFM measurements

The morphological characterization of 2D pyrophillite was done by imaging in the tapping AFM mode. Friction was measured using friction force microscopy, by recording the lateral force which corresponds to the lateral torsion of the AFM cantilever during scanning in the contact AFM mode. The friction signal was calculated as a half difference between lateral forces measured in forward and backward scan direction. The measurements were done using NSG01 probes (nominal stiffness 5 N/m) from NT-MDT, while the applied normal load was up to $\sim$300 nN, well below the threshold force needed to initiate wear. The wedge calibration of frictional forces was used in order to transform measured lateral signal into frictional forces [44].

Wear properties were studied by scratching the pyrophyllite flakes in the AFM contact mode. Square domains were scratched with an increased normal force (applied by the AFM tip) from the bottom to the top of the scan regions. The maximal normal load needed to initiate wear was around 1 µN. When a wear was initiated, the normal force was held constant. Mechanically robust and stiff, diamond coated probes DCP11 (nominal stiffness 11.5 N/m) from NT-MDT were used since they allowed high normal forces needed for scratching as well as subsequent imaging of scratched areas in the tapping AFM mode.

The AFM based nano-lithography was done using diamond coated probes HA_HR_DCP (nominal stiffness 35 N/m) from NT-MDT in three modes: nanoindentation and two lithographic modes, vector and raster. The nanoindentation mode is very similar to the measurement of force–displacement curves. The AFM scanner holding a sample was moved only vertically (without scanning in the horizontal plane) toward the AFM tip in order to induce a point-like deformation in pyrophyllite. For this purpose, the applied normal load was around 6 µN. In the lithographic modes, pyrophillite surface was scratched in the AFM contact mode according to predefined templates. In the case of the vector lithography, the templates were defined by discrete lines only, whereas in the case of the raster lithography, the square domains were taken for simplicity. During the nano-lithography, two force levels were applied. The low force level was applied along trajectories of the AFM tip which should stay intact (the movements between discrete line segments to be scratched, from the initial position to the first line segment, and from the last line segment back to the initial position). On the other hand, a high force level in the range $\sim$2–6 µN was applied on segments which are to be scratched. The scratching velocity was around 0.2 µm/s. It was significantly decreased compared to the scanning speed in order to provide an efficient lithography.

The study of insulating properties and dielectric breakdown requires 2D pyrophyllite flakes placed between two metallic electrodes. In order to make possible study at the nanoscale, conductive AFM (C-AFM) was employed. For this purpose, the pyrophyllite flakes obtained by LPE method were deposited on a gold substrate. Then, a metallic AFM tip on the top of a pyrophyllite flake served as a top electrode, while the underlying gold was a bottom electrode. The bias voltage was applied on the gold, while the AFM tip in contact with the pyrophyllite flakes was (virtually) grounded. The current imaging was done by scanning in C-AFM mode, using highly doped and conductive, diamond coated probes DCP11, and simultaneously recording topography and local current. Dielectric breakdown was examined by measuring local I/V curves at single point, while the bias voltage was swept in a range ±10 V.

3. Results and discussion

3.1. Structural and vibrational properties

The results of XRPD measurements presented in Fig. 1(d) show that the specimen predominantly contains crystalline pyrophyllite-1A (PDF (Powder Diffraction File) card # 01-075-0856), whereas a small amount (near detection limit) of dickite-2M1 (PDF card # 00-058-2002) was also identified. The most intense reflections in the XRPD pattern of the dominant phase are 00l ($l = 1-5$) which is in accordance with the layered structure of pyrophyllite-1A. The XRPD results indicate that a crystalline pyrophyllite sample (Fig. 1(b)) has a triclinic lattice and 2:1 structure (two tetrahedral sheets and one octahedral sheet) depicted in Fig. 1(a). The refined unit cell parameters for pyrophyllite-1A are the following (estimated standard deviations in parenthesis): $a = 5.14(2)$ Å, $b = 8.99(4)$ Å, $c = 9.28(4)$ Å, $\alpha = 91.88(8)°$, $\beta = 99.36(15)°$, $\gamma = 89.16(15)°$, $V = 423(3)$ Å^3. The refined values, within an experimental error, are in a very good agreement with the values obtained for pyrophyllite-1A (OH group in the structure) in both single crystal XRD experiment [45] and powder XRD experiment [46].

Raman spectra of the bulk crystalline pyrophyllite are presented in Fig. 2 in the spectral ranges from 50 to 1100 cm^{-1} and 3600 to 3750 cm^{-1}. The first range describes the fundamental vibrations of all phyllosilicates, whereas the second one displays the vibrations of the H_2O/OH group [47–49]. Our spectra are fully consistent with the previous published Raman spectra of crystalline pyrophyllite [47]. They contain all fundamental modes up to 1100 cm^{-1} as well as H_2O/OH peak at 3670 cm^{-1}. Details and the full assignment of all modes could be found elsewhere [47].
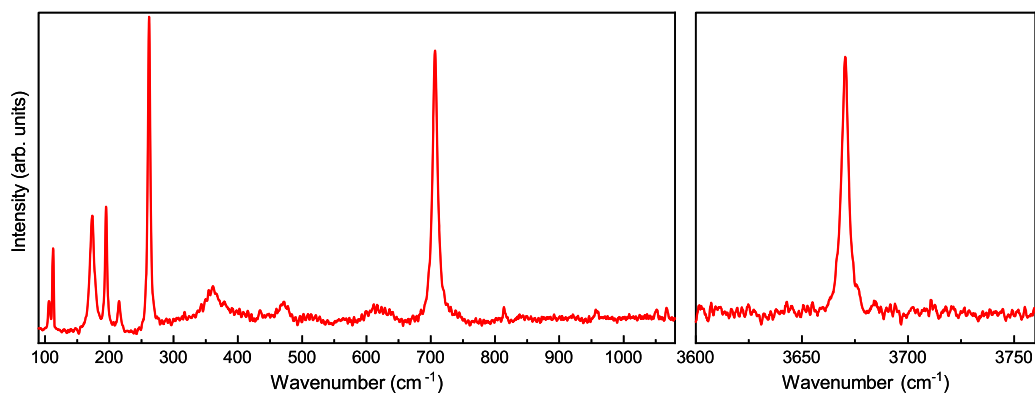
Fig. 2. Raman spectrum of a bulk pyrophyllite for two spectral ranges: the fundamental vibrations of phyllosilicates (left) and the H_2O/OH range (right).
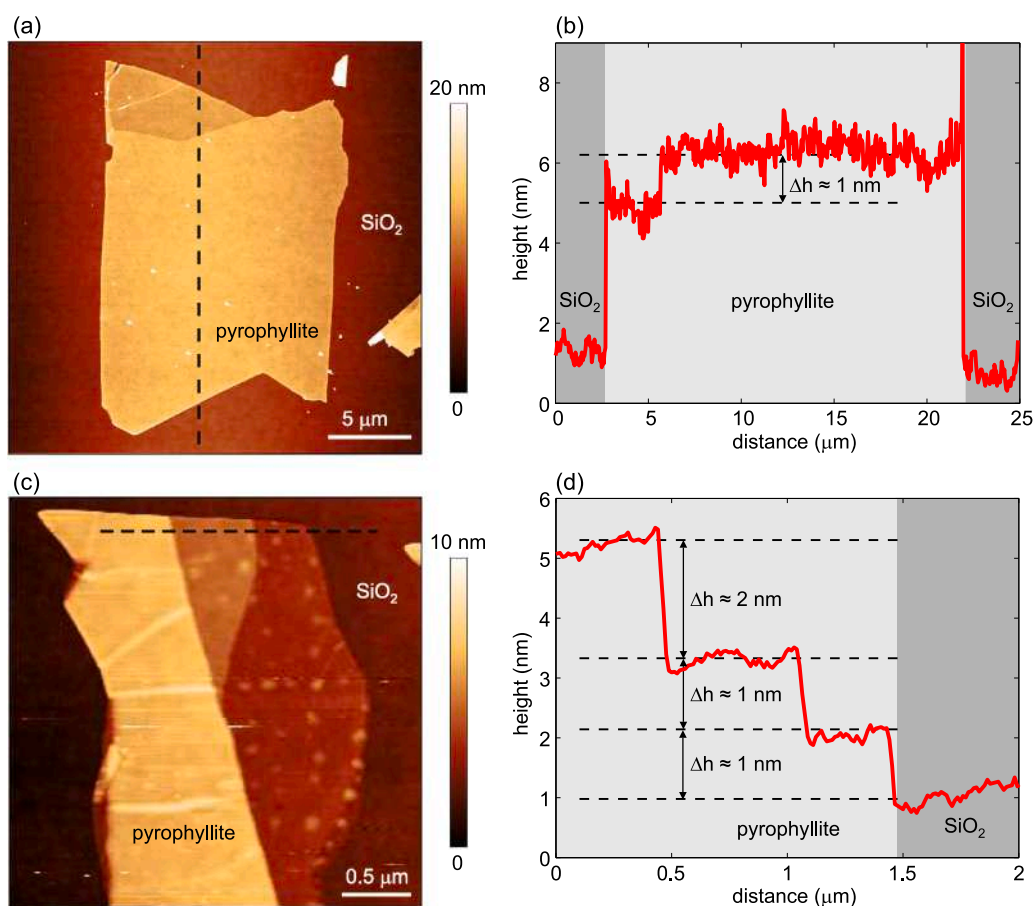

Fig. 3. (a), (c) Topographic images of pyrophillite flakes mechanically exfoliated on Si/SiO_2 with (b), (d) corresponding height profiles along dashed lines with indicated characteristic step heights.

3.2. Morphology

Fig. 3(a) depicts the topography of a typical flake obtained by mechanical exfoliation, with the height profile given in Fig. 3(b). It is a few-layer pyrophyllite with a thickness of ∼5 nm and an area of ∼15 × 20 μm². The root-mean-square roughness calculated on 5 × 5 μm² areas is only 0.6 nm indicating atomically flat surface free of residues. The height profile (Fig. 3(b)) reveals that a step height between two domains is only ∼1 nm.

The trilayer structure of the pyrophyllite unit cell displayed in Fig. 1(a) consists of AlO_6 octahedral sheet sandwiched between two SiO_4 tetrahedral layers. According to XRPD results, the thickness of the neutral trilayer is 6.39 Å, whereas the thickness of van der Waals

gap is 2.76 Å [45], measuring from the center of oxygen ions (O^{2-}). Accordingly, the effective thickness of the trilayer is around 9.2 Å, measuring from the top to bottom oxygen surfaces since we have to add two oxygen ion radii of 2.8 Å. Therefore, the thickness of single layer pyrophyllite measured by AFM should be around more or the same. The smallest thickness measured in our AFM experiments was always around 1 nm. The same minimal thickness was observed in AFM scratching based experiments as discussed below. Therefore, this value corresponds to the single layer of pyrophyllite. The small discrepancy between expected (around 9.2 Å) and measured thickness (around 1 nm) probably appears due to adsorbed water layer which is inevitable at ambient conditions and/or due to measurements done in
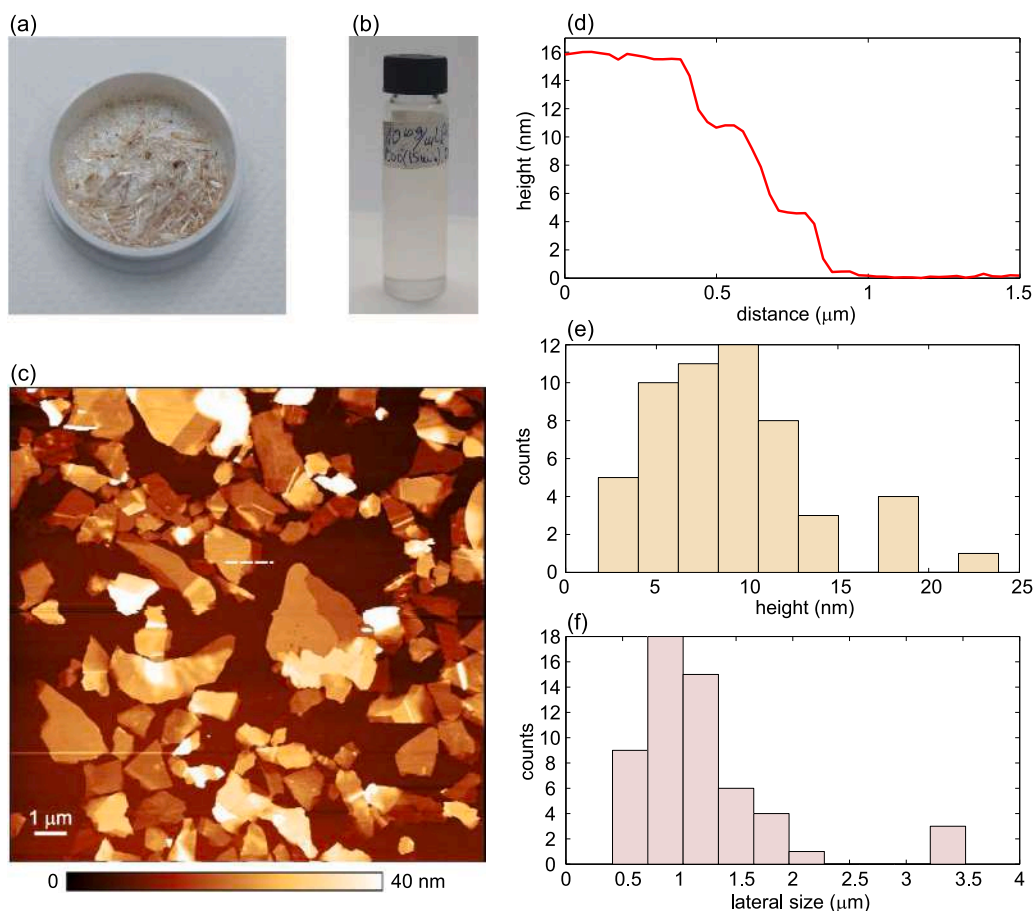
Fig. 4. (a) Ground pyrophyllite mineral used as a starting material for LPE and (b) the resulting dispersion employed for LBA. (c) Topographic image of pyrophillite flakes obtained by LPE and subsequent LBA on Si/SiO₂. (d) Height profile along the dashed line in (c). Histograms of (e) height and (f) lateral size of the flakes shown in (c).

tapping AFM mode, which commonly gives an increased step height on atomically thin layers [50].

Generally, we routinely exfoliated few layer pyrophillite flakes with the lateral size larger than 10 μm. On the other hand, yield of single layers was low, while their size was significantly smaller. One example is illustrated in Fig. 3(c). The corresponding height profile in Fig. 3(d) displays two single-layer step heights of ∼1 nm, and the third step height of ∼2 nm which corresponds to double-layer flake. As can be seen, the area of the single layer pyrophyllite is only several square micrometers.

The ground pyrophyllite crystal and its yellowish dispersion used in LPE are depicted in Fig. 4(a) and (b), respectively. Topography of 2D pyrophyllite obtained by the LPE method is depicted in Fig. 4(c). The height profile in Fig. 4(d) displays three step heights of ∼5 nm. Samples produced by the LPE method consist of a network of flakes with a typical height of 5−15 nm (Fig. 4(e)) and lateral dimensions of ∼1 μm (Fig. 4(f)). The flakes have well defined shapes, flat surface and regular edges. Although they are thicker and smaller compared to those fabricated by the mechanical exfoliation, LPE method provides large scale production of 2D pyrophyllite. At the same time, the LPE method can be easily adapted to various substrates. This was employed below in the study of insulating properties and dielectric breakdown of 2D pyrophyllite, where the flakes were deposited on a gold substrate.

3.3. Friction

Friction properties are analyzed on a small segment of the pyrophyllite layer surrounded by SiO₂ as depicted in Fig. 5(a). In the friction force map displayed in Fig. 5(b), the pyrophyllite is represented by

a dark contrast, thus indicating decreased friction compared to SiO₂. The height and friction force profiles from Fig. 5(c) reveal three times lower friction on the pyrophyllite. The same measurements were done for the normal force in the range ∼30−330 nN. Average friction forces on both pyrophyllite and SiO₂ were calculated from the histograms of friction maps and the corresponding results are presented in Fig. 5(d). As can be seen, the friction force approximately linearly increases with the normal force in accordance with Amonton's law. The friction coefficients were calculated from the slopes of the linear fits (dashed lines in Fig. 5(d)). The obtained friction coefficient of the pyrophyllite flake $\mu_{pyr} = 0.12$ is more than four times lower than the friction coefficient of surrounding silicon-dioxide substrate ($\mu_{SiO_2} = 0.5$). At the same time, μ_{pyr} is very similar to the friction coefficient of graphene grown by chemical vapour deposition [51] and 2D talc [21]. Therefore, the presented results indicate good lubricating properties of few-layer thick pyrophyllite.

Generally, mechanical and liquid phase exfoliation give 2D layers with the same physical properties. The main difference between two methods is morphology of produced layers, the lateral size of the flakes before all. Therefore, we expect the same friction properties of pyrophyllite obtained by both methods. Additional friction measurements on LPE pyrophyllite prove this predictions. The results presented in figure S1 of Supplementary material show that pyrophyllite flakes obtained by LPE has a low friction coefficient of around 0.14, that is, very similar to pyrophyllite obtained by the mechanical exfoliation (0.12). Compared to the surrounding silicon-dioxide substrate, the friction is again decreased by around four times.

In our previous manuscript [21] we investigated friction as a function of talc thickness in detail. Talc friction reduces with number of layers (talc thickness), which is similar to other 2D materials, since so
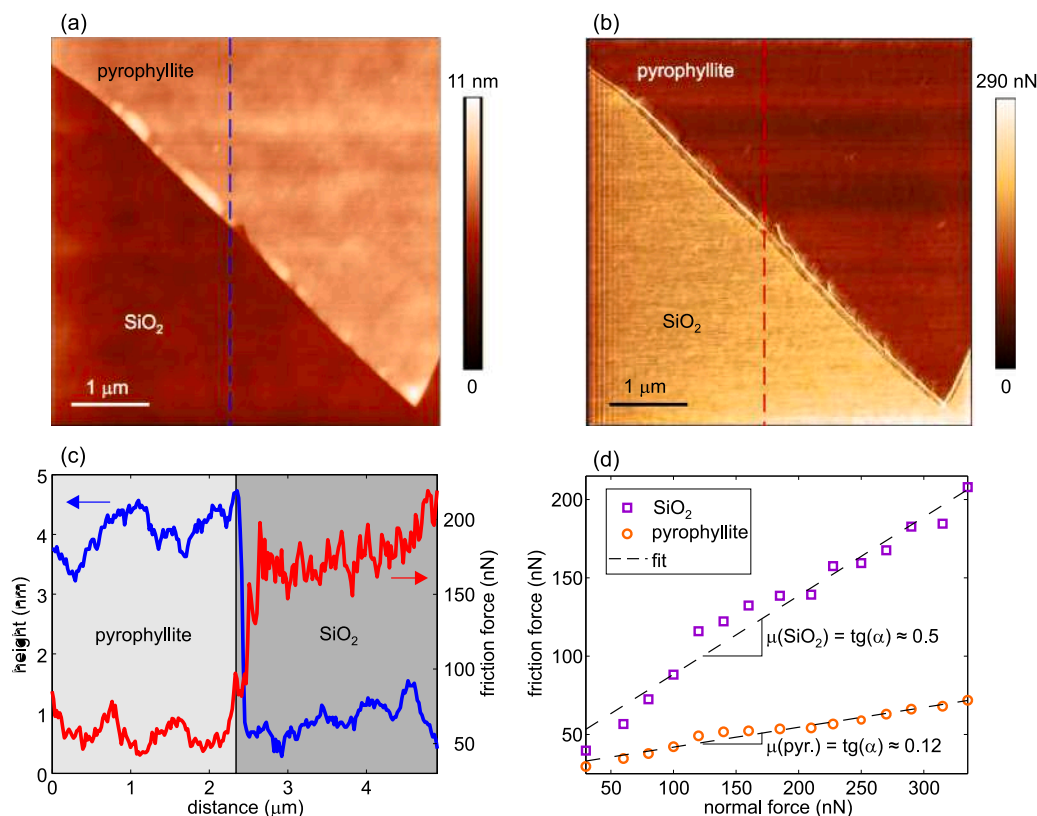
Fig. 5. (a) Topography and (b) friction force map of pyrophyllite flake on Si/SiO$_2$. (c) Height and force profiles along dashed lines in (a) and (b), respectively. (d) Average friction force (calculated from histograms of friction maps such as the one presented in (b)) as a function of the normal force applied by the AFM tip. Friction coefficients were calculated as slopes of the linear fits represented by dashed lines.

called puckering effect, responsible for the friction of 2D materials, is less pronounced for thicker layers due to larger bending rigidity. In the case of talc, this dependence is rather weak, since single layer is 1 nm thick and already consists of three atomic planes. Pyrophyllite and talc belong to the family of 2:1 phyllosilicates. Their chemical formulas are almost identical (pyrophyllite - Al$_2$Si$_4$O$_{10}$(OH)$_2$, talc - Mg$_3$Si$_4$O$_{10}$(OH)$_2$) and they have practically the same structure (octahedral plane with metallic (Al or Mg) ion sandwiched between two tetrahedral SiO layers). The thickness of the single layer (around 1 nm) is similar in both materials. Therefore, dependence of the friction as a function of pyrophyllite thickness should be the same as for talc. This conclusion is further confirmed in figure S1(b) of Supplementary material depicting friction map of pyrophyllite flakes produced by LPE. Although their thicknesses vary in a broad range from only several nanometers to several tens of nanometers, the friction force on the pyrophyllite is associated with a single peak in the corresponding histogram given in figure S1(c) (the observed dispersion (width of the histogram peak) is very similar to the dispersion of the friction force measured on SiO$_2$ substrate).

3.4. Wear

The next step was to analyze wear properties and behavior of 2D pyrophyllite for high normal load applied by the AFM tip during scanning in contact mode. Fig. 6(a) displays the topography recorded after the AFM scratching of the central square domain. From the right, left, and top side, the scratched domain is surrounded by walls (represented by a bright contrast) formed from the material deposited by the AFM tip. Enlarged topographic image of the scratched area is presented in Fig. 6(b) together with the characteristic height profile in Fig. 6(c). At the bottom of the figure, the pyrophyllite surface is flat and without visible wear scars due to low normal load. At the same

time, the lateral force recorded during the AFM scratching is low and approximately constant as depicted in Fig. 6(d) and (e). Since there is no wear, the lateral force corresponds to the friction between the AFM tip and pyrophyllite.

In the experiment, the normal load was increasing as the AFM tip was moving from the bottom to the top. For high enough normal load of around 1.1 μN, the wear was initiated and afterwards, the normal load was held constant. As a result of the wear, pyrophyllite surface became crumpled with many local holes and bumps. The holes present local depressions made by peeling pyrophyllite layers, while bumps are local hills formed out of the material previously peeled off (Fig. 6(c)). The height profile in Fig. 6(c) reveals several step heights of ~1 nm. They correspond to single layer of pyrophyllite which therefore indicates that the AFM scratching leads to layer-by-layer peeling. The lateral force during the scratching (Fig. 6(d) and (e)) is increased compared to the bottom area without wear scars. Although this is expected due to higher normal load applied by the AFM tip, the lateral force profile is not flat anymore, but strongly oscillating. Obviously, bright puddles in the force map (Fig. 6(d)) and peaks in the force profile (Fig. 6(e)) correspond to strongly increased lateral force required for tearing and peeling of pyrophyllite layers.

According to the presented results, during the AFM scratching, pyrophyllite behaves in a different manner compared to well known 2D materials such as graphene and transition metal dichalcogenides (MoS$_2$, and WS$_2$) [52,53]. The scratching of these materials is associated with wrinkling at the initial stage, while at higher normal loads, it is followed by a sudden tearing along the direction of the AFM tip movement, and finally by a peeling of large segments and their folding. On the other hand, in the case of pyrophyllite, exfoliated segments made by the AFM scratching are small, not folded, and they form local bumps of irregular shapes. Recently, similar results have been obtained for muscovite (mica), another phyllosilicate van der Waals mineral, and
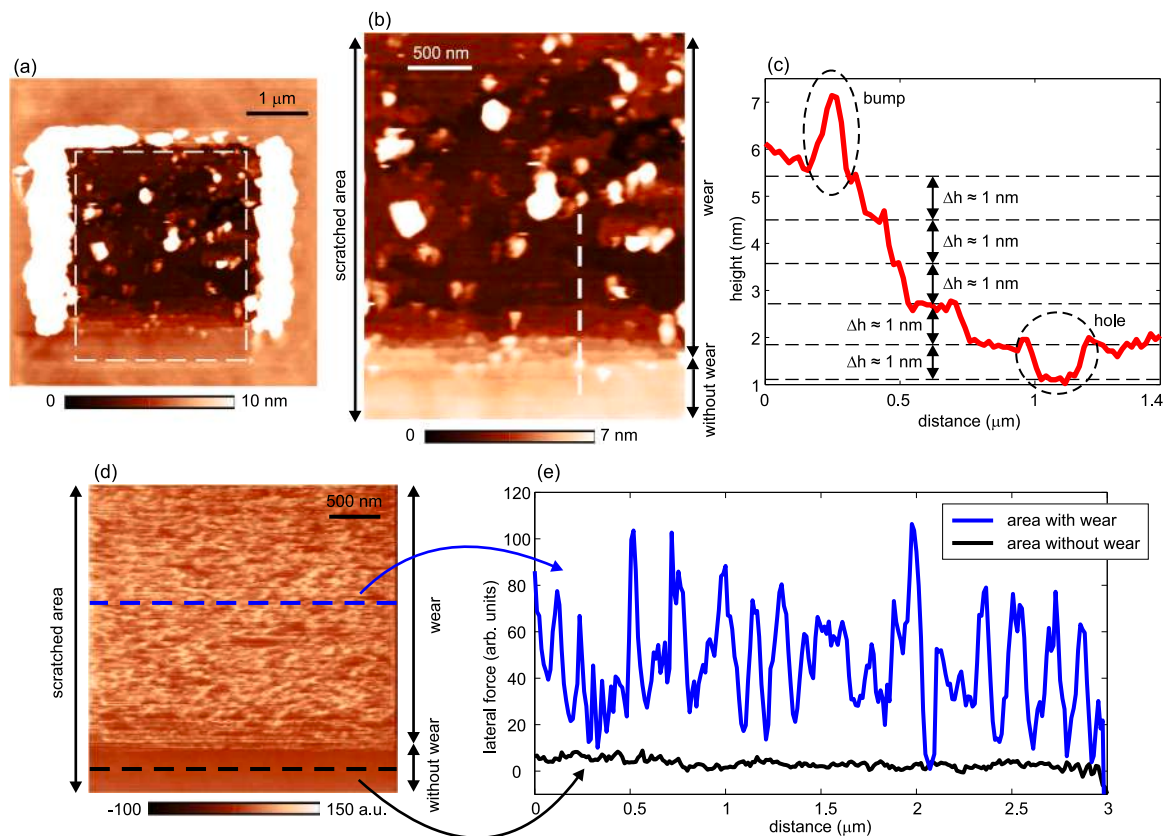
Fig. 6. (a) Topographic image of a pyrophyllite flake after the AFM scratching. (b) The topographic image of the domain encircled by the dashed line in (a) focusing on the scratched area only. (c) The height profile along the dashed line in (b) with indicated step heights of ∼1 nm and local hole/bump (encircled by dashed lines). (d) The lateral force map recorded during the AFM scratching. (e) The lateral force profiles along two dashed lines in (d), standing for the area with and without wear.

the observed difference in wear properties were explained by different mechanical properties [53]. Accordingly, significant thickness of single layer of pyrophyllite (∼1 nm) and large bending rigidity of ∼70 eV [54] limit its flexibility and folding. At the same time, Young's modulus (modulus of elasticity) of ∼100 GPa [55,56] and tensile strength less than 10 GPa [56,57] are much lower than in the case of graphene and transition metal dichalcogenides, which indicates much brittle structure of pyrophyllite. This can be indirectly confirmed by comparing threshold normal loads needed to initiate wear. In the case of graphene and transition metal dichalcogenides, the threshold load is at least several μN [52,53], while in the case of pyrophyllite, it is much lower, around 1 μN. As a result, pyrophillite layers are easily torn into small pieces during AFM scratching.

Wear of 2D materials is always started from their edges (these are weak points for wear), and not on homogeneous (flat) 2D flakes [58]. Since LPE 2D materials are associated with small flakes and huge number of exposed edges, their wear resistance is determined by their edges [59], and it is always lower that the wear resistivity of 2D material itself. For this reason, wear of LPE pyrophyllite was not studied here.

3.5. Nanoscale machining and nanolithography

As mentioned in the previous section, the AFM scratching of graphene and transition metal dichalcogenides generally leads to their peeling, but not to local cutting along directions defined by the movement of the AFM tip. On the other hand, lower elasticity and tensile strength of 2D pyrophyllite indicate that it could be suitable material for AFM scratching based nanolithography. The results of the nanolithography of 2D pyrophyllite are presented in Fig. 7. Three basic shapes and characteristic height profiles are presented for the following

cases: the hole made by nanoindentation (Fig. 7(a–b)), the trench carved out by line scratching (Fig. 7(c–d)), and the square crater made by raster scratching (Fig. 7(e–f)). As can be seen, the AFM tip induces local carving of a pyrophyllite flake. This process is associated with the tearing of the pyrophyllite into small pieces, which are then deposited around the tip during its motion. The deposited material was then removed by several additional scans in contact AFM mode (not shown here). They were done at lower normal load, which was insufficient to cause pyrophyllite cutting and wear, but high enough to provide pushing of the deposited material by the AFM tip.

As can be seen, 2D pyrophyllite is efficiently carved by applying a local pressure at single point (Fig. 7(a)) as well as during AFM tip motion (Fig. 7(c)). Making of holes on wider areas is successfully achieved by AFM scratching along array of parallel lines (Fig. 7(e)). Depth of created objects was controlled by applied normal load as illustrated in Fig. 7(e–f) showing that a deeper crater was formed by a higher normal force. The width of the line trench in Fig. 7(c) is 150−300 nm. It is strongly influenced by the width of the diamond coated probes employed here, and it is reasonable to expect that a better resolution and more narrow features could be created with sharper AFM tips.

3.6. Electronic bandgap

Electronic bandgap was estimated from UV–VIS spectroscopic measurements. For that purpose, a large-area pyrophyllite film was obtained by LPE. The film thickness was around 20 nm as determined by AFM measurement. Transmittance through the pyrophyllite film for wavelengths in the range 200−900 nm is displayed in the inset of Fig. 8. As can be seen, the film is transparent with the transmittance in the visible region above 97%. The obtained transmittance spectrum allows the calculation of an intrinsic optical absorption coefficient
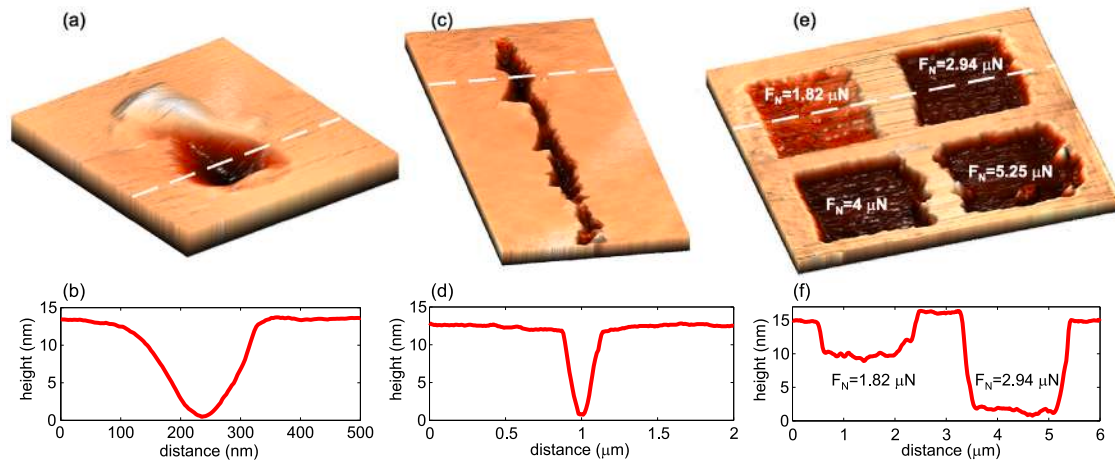
Fig. 7. The topographic images and the height profiles for three characteristic structures made by nanolithography of pyrophyllite: (a–b) single hole obtained by nanoindentation, (c–d) trench made by the AFM scratching along single line, (e–f) four square domains made by raster scratching.
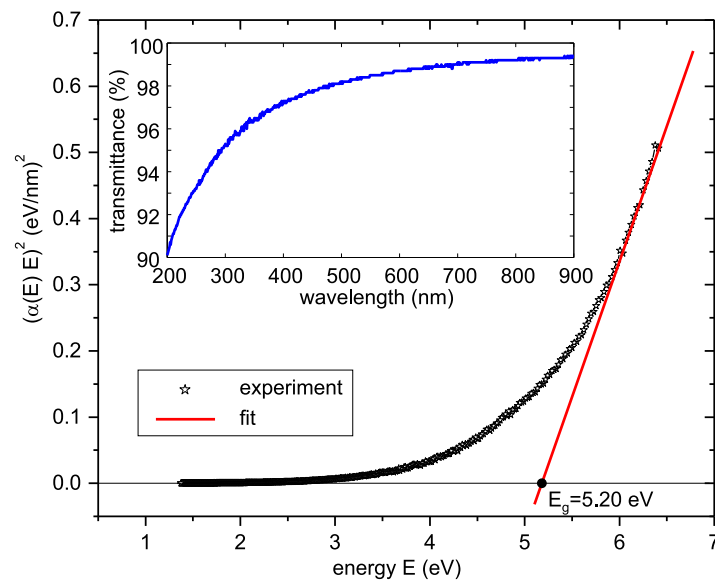

Fig. 8. The Tauc plot with estimated bandgap energy of ∼5.20 eV obtained from the transmittance (plot in the inset) through ∼20 nm thick pyrophyllite film obtained by LPE on a quartz substrate.

$\alpha(E)$. Namely, the well known Bourguer–Lambert–Beer (BLB) law gives the absorption coefficient as $\alpha_{\mathrm{BLB}}(E) = (1/d)\ln(1/T)$, where d is the film thickness and T the measured transmittance [60]. This is the simplest law representing the optical absorption in semiconductors, and in practice the BLB law turned out to be more than a good enough approximation.

For the estimation of a direct optical bandgap E_g, we used the Tauc method [61] and the standard fitting procedure of the linear part of $(\alpha(E)E)^2$ (Tauc plot), i.e. $(\alpha(E)E)^2 = \mathrm{const} \cdot (E - E_g)$. The Tauc plot displaying $(\alpha(E)E)^2$ as a function of the energy of incident light $E = h\nu$ (h is the Planck constant, ν is the frequency of incident photon) is given in Fig. 8. The plot indicates that the pyrophyllite film has a direct band gap of around 5.20 eV (the value obtained as the intersection point of the linear fit of the Tauc plot and x-axis). The obtained value is consistent with the theoretical value of 5.42 eV [55], whereas to best of our knowledge, this is the first experimentally obtained value of the pyrophyllite bandgap. The measured value is also close to the band gap of 2D hexagonal boron nitride (∼6 eV) [62], which implies that pyrophyllite can be considered as efficient 2D insulator as well.

3.7. Insulating properties and dielectric breakdown

Hexagonal boron nitride has been a standard choice as insulator in 2D electronics [63–67]. Insulating properties and dielectric breakdown are usually explored by placing materials between two metallic electrodes in order to form a capacitor. Furthermore, C-AFM [68, 69] provides characterization at the nanoscale [63–65,70–72]. Recent studies have extended the family of 2D insulators to materials with improved properties, such as high-k van der Waals dielectrics [70].

In order to study dielectric properties, 2D pyrophyllite flakes obtained by LPE were deposited on a conductive substrate—thin gold film, which acted as a bottom electrode, while the AFM tip had a role of the top electrode. The topography image (Fig. 9(a)), corresponding current map (Fig. 9(b)), and characteristic profiles (Fig. 9(c)) reveal that pyrophyllite flakes with a thickness ranging from 3 nm to 22 nm are associated with a dark (black) contrast in the current map and zero current. The black color of pyrophyllite flakes in the current map in Fig. 9(b) is spatially homogeneous and therefore it does not contain current spikes which would indicate a possible dielectric breakdown. As a result, at the applied bias voltage $U = 2$ V, several nanometer thick pyrophyllite behaves as 2D insulator.
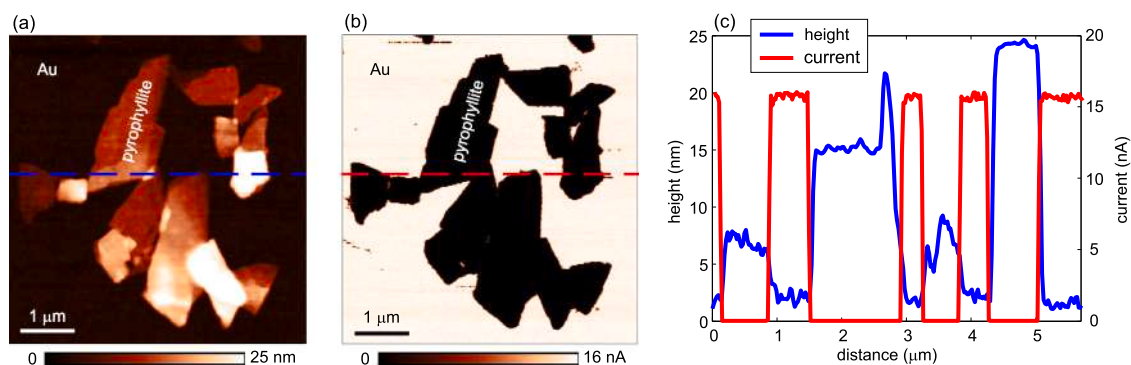
Fig. 9. (a) Topography and (b) the corresponding current maps of the pyrophillite flakes (obtained by LPE) deposited onto gold substrate. (c) The overlapped height and current profiles along the dashed lines in (a) and (b).
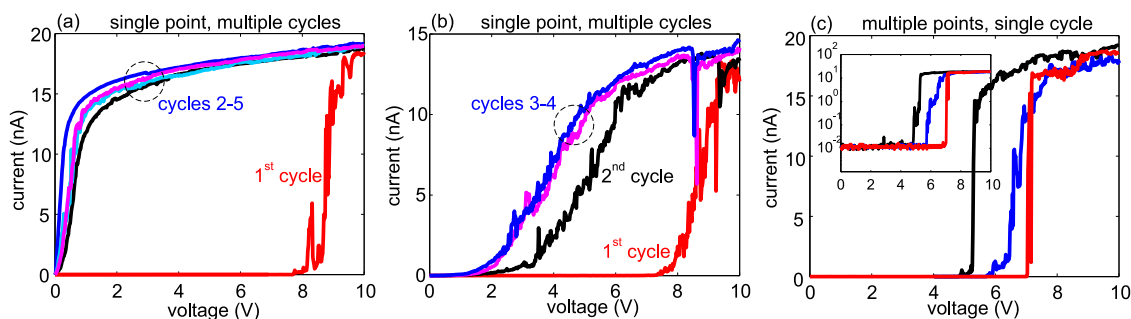

Fig. 10. (a) and (b) Successive cycles of the I/V curves measured at single point (but two different points). (c) The I/V curves (the first cycle only) measured at three different points of the same 10 nm thick pyrophyllite flake. The inset displays the I/V curves in semi-logarithmic scale.

In order to induce a dielectric breakdown, local I/V curves were measured in a wider voltage range. Typical results are given in Fig. 10(a) showing five successive cycles measured at the same point in the voltage range ± 10 V. In the first cycle, the current is zero for voltages below ~ 8 V. After reaching this threshold voltage, the current rapidly grows indicating dielectric breakdown. In the next cycles (2–5), for small voltages below ~ 0.5 V, the current practically linearly increases with the applied bias voltage without any threshold (small nonlinearities around the zero voltage indicate possible Schottky barriers at the tip-sample contact, whereas the decreased slope of I/V curves for the voltages higher than ~ 0.5 V is due to limitations of the current amplifier). Therefore, pyrophyllite does not behave as an insulator anymore and the metallic AFM tip is practically short circuited by the bottom gold electrode. In another case presented in Fig. 10(b), after the first cycle and dielectric breakdown, the region with zero (or near to zero) current becomes narrower indicating gradually decreasing the electronic bandgap of pyrophyllite.

Fig. 10(c) displays the I/V curves (only the first cycles shown) measured at three different points on the same flake. Rapid increase of the current is observed for threshold voltage in the range 5−7 V. The semilogarithmic scale displayed in the inset reveals that below the threshold voltage, the current is at almost constant level in the order of 10^{-2} nA. Taking into account that the thickness of examined pyrophyllite flake was ~ 10 nm, the dielectric breakdown strength of 2D pyrophyllite is around 6 MV/cm. Although the obtained value is slightly below the strength of 2D hexagonal boron-nitride (~ 8 MV/cm) [63], the presented results indicate that 2D pyrophyllite has good insulating properties and could be considered as an efficient 2D dielectric and gate oxide. One of the main issue with applications of hexagonal boron-nitride as 2D insulator is its low dielectric constant (~ 3.9) responsible for high leakage currents. Although dielectric measurements of pyrophyllite are very rare [36,37], it is reasonable to expect lower leakage currents due to larger dielectric constant of pyrophyllite of around 10, which is also similar to the permittivity of the second

member of 2:1 family of phyllosilicates—talc [73]. Still, this has to be confirmed in future studies since leakage currents are influenced by other factors, such as layers' quality (absence of structural defects) and the conduction/valence band discontinuity with respect to the substrate.

Morphological changes after the dielectric breakdown of phyrophyllite are illustrated in Fig. 11. Two- and three-dimensional images of the pyrophyllite flake (Fig. 11(a) and (b), respectively) are recorded in tapping mode after 30 I/V curves measured in the range ± 10 V at the point marked by the arrow. As can be seen, a small hole appeared at the point where the I/V curves were measured, while protrusions appeared around the hole. Height profile in Fig. 11(c) reveals that the hole depth is around 1 nm which corresponds to the thickness of single layer of pyrophyllite. The presented results demonstrate that high local electric fields causing dielectric breakdown lead to local fracture of 2D pyrophyllite. The hole depth equal to the thickness of single layer of pyrophyllite indicates that in the considered case, only the most top pyrophyllite layer was locally cut, while the pyrophyllite thickness is reduced at this point. Although additional measurements should be done in future studies, these results suggest layer-by-layer breakdown of pyrophyllite which was previously confirmed in the case of hexagonal boron nitride [65].

Friction measurements done after the induced dielectric breakdown demonstrate that the point where I/V curves were previously measured is associated with increased friction compared to the rest of pyrophyllite flake. The increased friction indicates some chemical and/or structural changes on the pyrophyllite surface which should be further explored in future studies.

4. Conclusions

In a summary, we have thoroughly characterized pyrophyllite crystal and then successfully fabricated 2D flakes by using both mechanical exfoliation and LPE. Pyrophyllite was exfoliated down to single layer.
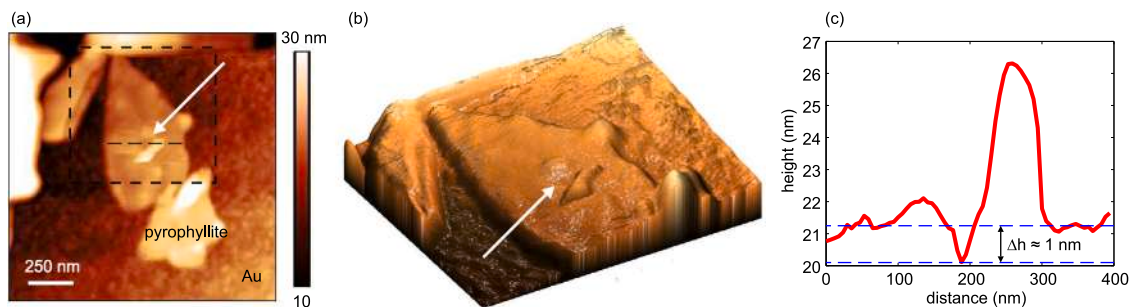
Fig. 11. (a) Two-dimensional topographic image of the pyrophyllite flake after 30 I/V curves measured in the range ±10 V at the point marked by the arrow. (b) Three-dimensional topographic image of the area marked by dashed square in (a). (c) Height profile along the dashed line marked in (a).

The lateral size of typical few-layer flakes was in the order of 10 μm in the case of the mechanical exfoliation, and 1 μm in the case of the LPE. 2D pyrophyllite has different wear properties compared to graphene and transition metal dichalcogenides. The wear is initiated at much lower normal loads while AFM based scratching leads to the tearing of pyrophyllite into small pieces, contrary to nano-exfoliation and folding, typically observed on graphene for example. Such wear properties provide easy machining at the nanoscale by the AFM tip which can be used as a tool for local carving and reshaping of pyrophyllite flakes. At the same time, 2D pyrophyllite has a low friction coefficient of ∼0.1 and therefore, it joins the family of other van der Waals layered materials as a potential candidate for ultra-thin coatings aimed for solid lubrication in micro- and nano-mechanical devices. The optical measurements on thin (∼20 nm) 2D pyrophyllite film obtained by the LPE reveal that it is transparent in the visible domain, with a large band gap of 5.2 eV. The local studies by C-AFM demonstrated that several nanometer thick pyrophyllite flakes behaves as 2D insulators with a high breakdown voltage of around 6 MV/cm, which is close to hexagonal boron-nitride. In addition, the larger dielectric permittivity of pyrophyllite compared to the boron nitride could provide lower leakage currents which needs to be confirmed in future studies.

CRediT authorship contribution statement

Borislav Vasić: Conceptualization, Investigation, Methodology, Formal analysis, Visualization, Writing – original draft. **Radoš Gajić:** Conceptualization, Investigation, Formal analysis, Resources, Supervision, Funding acquisition, Writing – review & editing. **Ivana Milošević:** Investigation, Visualization. **Žarko Medić:** Investigation, Visualization. **Marina Blagojev:** Investigation, Visualization. **Marko Opačić:** Investigation, Formal analysis, Visualization. **Aleksandar Kremenović:** Investigation, Formal analysis, Visualization, Writing – review & editing. **Dejan Lazić:** Investigation, Formal analysis.

Declaration of competing interest

The authors declare that they have no known competing financial interests or personal relationships that could have appeared to influence the work reported in this paper.

Data availability

Data will be made available on request.

Acknowledgments

Appendix A. Supplementary data

Supplementary material related to this article can be found online at https://doi.org/10.1016/j.apsusc.2022.155114.

References

[1] K.S. Novoselov, A.K. Geim, S.V. Morozov, D. Jiang, Y. Zhang, S.V. Dubonos, I.V. Grigorieva, A.A. Firsov, Electric field effect in atomically thin carbon films, Science 306 (2004) 666–669.

[2] A.K. Geim, K.S. Novoselov, The rise of graphene, Nature Mater. 6 (2007) 183–191.

[3] T.F. Avouris, P. nad Heinz, T. Low, 2D Materials, Cambridge University Press, 2017.

[4] Y.M. Jhon, J.H. Lee, 2D Materials for Nanophotonics, Elsevier, 2021.

[5] M. Houssa, A. Dimoulas, A. Molle, 2D Materials for Nanoelectronics, CRC Press, 2016.

[6] B. Radisavljevic, A. Radenovic, J. Brivio, V. Giacometti, A. Kis, Single-layer MoS$_2$ transistors, Nat. Nanotechnol. 6 (2011) 147–150.

[7] M. Xu, T. Liang, M. Shi, H. Chen, Graphene-like two-dimensional materials, Chem. Rev. 113 (2013) 3766–3798.

[8] S.Z. Butler, S.M. Hollen, L. Cao, Y. Cui, J.A. Gupta, H.R. Gutiérrez, T.F. Heinz, S.S. Hong, J. Huang, A.F. Ismach, E. Johnston-Halperin, M. Kuno, V.V. Plashnitsa, R.D. Robinson, R.S. Ruoff, S. Salahuddin, J. Shan, L. Shi, M.G. Spencer, M. Terrones, W. Windl, J.E. Goldberger, Progress, challenges, and opportunities in two-dimensional materials beyond graphene, ACS Nano 7 (2013) 2898–2926.

[9] R. Ganatra, Q. Zhang, Few-layer MoS$_2$: A promising layered semiconductor, ACS Nano 8 (2014) 4074–4099.

[10] S. Manzeli, D. Ovchinnikov, D. Pasquier, O.V. Yazyev, A. Kis, 2D transition metal dichalcogenides, Nat. Rev. Mater. 2 (2017) 17033.

[11] K. Zhang, Y. Feng, F. Wang, Z. Yang, J. Wang, Two dimensional hexagonal boron nitride (2D-hBN): synthesis, properties and applications, J. Mater. Chem. C 5 (2017) 11992–12022.

[12] S. Balendhran, S. Walia, H. Nili, S. Sriram, M. Bhaskaran, Elemental analogues of graphene: Silicene, germanene, stanene, and phosphorene, Small 11 (2015) 640–652.

[13] M. Naguib, V.N. Mochalin, M.W. Barsoum, Y. Gogotsi, 25Th anniversary article: MXenes: A new family of two-dimensional materials, Adv. Mater. 26 (7) (2014) 992–1005.

[14] S. Shaikhutdinov, H.-J. Freund, Ultrathin silica films on metals: The long and winding road to understanding the atomic structure, Adv. Mater. 25 (2013) 49–67.

[15] R. Frisenda, Y. Niu, P. Gant, M. Muñoz, A. Castellanos-Gomez, Naturally occurring van der waals materials, npj 2D Mater. Appl. 4 (2020) 38.

[16] T. Gould, S. Lebègue, T. Björkman, J.F. Dobson, 2D structures beyond graphene: The brave new world of layered materials and how computers can help discover them, in: F. Iacopi, J. Boeckl, C. Jagadish (Eds.), 2D Materials, Academic Press, 2016, pp. 1–33, Ch. 1.

[17] K. Momma, F. Izumi, *VESTA3* for three-dimensional visualization of crystal, volumetric and morphology data, J. Appl. Crystallogr. 44 (2011) 1272–1276.

[18] A.B. Alencar, A.P.M. Barboza, B.S. Archanjo, H. Chacham, B.R.A. Neves, Experimental and theoretical investigations of monolayer and few-layer talc, 2D Mater. 2 (2015) 015004.

[19] A. Harvey, J.B. Boland, I. Godwin, A.G. Kelly, B.M. Szydłowska, G. Murtaza, A. Thomas, D.J. Lewis, P. O'Brien, J.N. Coleman, Exploring the versatility of liquid phase exfoliation: producing 2D nanosheets from talcum powder, cat litter and beach sand, 2D Mater. 4 (2017) 025054.

[20] A.R. Cadore, E. Mania, A.B. Alencar, N.P. Rezende, S. de Oliveira, K. Watanabe, T. Taniguchi, H. Chacham, L.C. Campos, R.G. Lacerda, Enhancing the response of NH$_3$ graphene-sensors by using devices with different graphene-substrate distances, Sensors Actuators B 266 (2018) 438–446.

[21] B. Vasić, C. Czibula, M. Kratzer, B.R.A. Neves, A. Matković, C. Teichert, Two-dimensional talc as a van der Waals material for solid lubrication at the nanoscale, Nanotechnology 32 (2021) 265701.

[22] D. Nutting, G.A. Prando, M. Severijnen, I.D. Barcelos, S. Guo, P.C.M. Christiansen, U. Zeitler, Y. Galvão Gobato, F. Withers, Electrical and optical properties of transition metal dichalcogenides on talc dielectrics, Nanoscale 13 (2021) 15853–15858.

[23] G.A. Prando, M.E. Severijnen, I.D. Barcelos, U. Zeitler, P.C.M. Christianen, F. Withers, Y. Galvão Gobato, Revealing excitonic complexes in monolayer WS_2 on talc dielectric, Phys. Rev. Appl. 16 (2021) 064055.

[24] A.C. Gadelha, T.L. Vasconcelos, L.G. Cançado, A. Jorio, Nano-optical imaging of in-plane homojunctions in graphene and MoS_2 van der Waals heterostructures on talc and SiO_2, J. Phys. Chem. Lett. 12 (2021) 7625–7631.

[25] A. Castellanos-Gomez, M. Wojtaszek, N. Tombros, N. Agraït, B.J. van Wees, G. Rubio-Bollinger, Atomically thin mica flakes and their application as ultrathin insulating substrates for graphene, Small 7 (2011) 2491–2497.

[26] X. Ji, Y. Kang, J. Ouyang, Y. Chen, D. Artzi, X. Zeng, Y. Xiao, C. Feng, B. Qi, N.Y. Kim, P.E. Saw, N. Kong, O.C. Farokhzad, W. Tao, 2D black mica nanosheets: Synthesis of ultrathin biotite nanosheets as an intelligent theranostic platform for combination cancer therapy, Adv. Sci. 6 (2019) 1970118.

[27] Z. Huang, T. Lan, L. Dai, X. Zhao, Z. Wang, Z. Zhang, B. Li, J. Li, J. Liu, B. Ding, A.K. Geim, H.-M. Cheng, B. Liu, 2D functional minerals as sustainable materials for magneto-optics, Adv. Mater. 34, 2110464.

[28] R. de Oliveira, L.A.G. Guallichico, E. Policarpo, A.R. Cadore, R.O. Freitas, F.M.C. da Silva, V. d. C. Teixeira, R.M. Paniago, H. Chacham, M.J.S. Matos, A. Malachias, K. Krambrock, I.D. Barcelos, High throughput investigation of an emergent and naturally abundant 2D material: Clinochlore, Appl. Surf. Sci. 559 (2022) 153959.

[29] A.R. Cadore, R. de Oliveira, R. Longuinhos, V. de C. Teixeira, D.A. Nagaoka, V.T. Alvarenga, J. Ribeiro-Soares, K. Watanabe, T. Taniguchi, R.M. Paniago, A. Malachias, K. Krambrock, I.D. Barcelos, C.J.S. de Matos, Exploring the structural and optoelectronic properties of natural insulating phlogopite in van der waals heterostructures, 2D Mater. 9 (2022) 035007.

[30] Y. Niu, J. Villalva, R. Frisenda, G. Sanchez-Santolino, L. Ruiz-González, E.M. Pérez, M. García-Hernández, E. Burzurí, A. Castellanos-Gomez, Mechanical and liquid phase exfoliation of cylindrite: a natural van der Waals superlattice with intrinsic magnetic interactions, 2D Mater. 6 (2019) 035023.

[31] A. Matković, L. Ludescher, O.E. Peil, A. Sharma, K.-P. Gradwohl, M. Kratzer, M. Zimmermann, J. Genser, D. Knez, E. Fisslthaler, C. Gammer, A. Lugstein, R.J. Bakker, L. Romaner, D.R.T. Zahn, F. Hofer, G. Salvan, J.G. Raith, C. Teichert, Iron-rich talc as air-stable platform for magnetic two-dimensional materials, npj 2D Mater. Appl. 5 (2021) 94.

[32] A.J. Molina-Mendoza, E. Giovanelli, W.S. Paz, M.A. Niño, J.O. Island, C. Evangeli, L. Aballe, M. Foerster, H.S.J. van der Zant, G. Rubio-Bollinger, N. Agraït, J.J. Palacios, E.M. Pérez, A. Castellanos-Gomez, Franckeite as a naturally occurring van der Waals heterostructure, Nature Commun. 8 (2017) 14409.

[33] M. Velický, P.S. Toth, A.M. Rakowski, A.P. Rooney, A. Kozikov, C.R. Woods, A. Mishchenko, L. Fumagalli, J. Yin, V. Zólyomi, T. Georgiou, S.J. Haigh, K.S. Novoselov, R.A.W. Dryfe, Exfoliation of natural van der Waals heterostructures to a single unit cell thickness, Nature Commun. 8 (2017) 14410.

[34] K. Ray, A.E. Yore, T. Mou, S. Jha, K.K.H. Smithe, B. Wang, E. Pop, A.K.M. Newaz, Photoresponse of natural van der Waals heterostructures, ACS Nano 11 (2017) 6024–6030.

[35] M.A. Ali, H.A.M. Ahmed, H.M. Ahmed, M. Hefni, Pyrophyllite: An economic mineral for different industrial applications, Appl. Sci. 11 (2021) 11357.

[36] G.W. Timco, Z. Dvorak, H.H. Schloessin, Dielectric properties of pyrophyllite as a function of water vapor pressure, J. Appl. Phys. 47 (1976) 2232–2233.

[37] E. Izci, The investigation of dielectric properties of pyrophyllite, Key Eng. Mater. 264–268 (2004) 1361–1364.

[38] E.W. Bucholz, X. Zhao, S.B. Sinnott, S.S. Perry, Friction and wear of pyrophyllite on the atomic scale, Tribol. Lett. 46 (2012) 159–165.

[39] E.L. Brightbill, Design Rules for Discovering 2D Materials from 3D Crystals, University of North Carolina at Chapel Hill, 2016.

[40] M. Shamim, T.K. Mukhopadhyay, K. Dana, Kinetic pathway for thermal exfoliation of pyrophyllite, Appl. Clay Sci. 114 (2015) 40–47.

[41] K.S. Novoselov, D. Jiang, F. Schedin, T.J. Booth, V.V. Khotkevich, S.V. Morozov, A.K. Geim, Two-dimensional atomic crystals, Proc. Natl. Acad. Sci. USA 102 (2005) 10451–10453.

[42] A. Matković, I. Milošević, M. Milićević, T. Tomašević-Ilić, J. Pešić, M. Musić, M. Spasenović, D. Jovanović, B. Vasić, C. Deeks, R. Panajotović, M.R. Belić, R. Gajić, Enhanced sheet conductivity of Langmuir–Blodgett assembled graphene thin films by chemical doping, 2D Mater. 3 (2016) 015002.

[43] I.R. Milošević, B. Vasić, A. Matković, J. Vujin, S. Aškrabić, M. Kratzer, T. Griesser, C. Teichert, R. Gajić, Single-step fabrication and work function engineering of Langmuir–Blodgett assembled few-layer graphene films with Li and Au salts, Sci. Rep. 10 (2020) 8476.

[44] M. Varenberg, I. Etsion, G. Halperin, An improved wedge calibration method for lateral force in atomic force microscopy, Rev. Sci. Instrum. 74 (2003) 3362–3367.

[45] J.H. Lee, S. Guggenheim, Single crystal X-ray refinement of pyrophyllite-1Tc, Am. Mineral. 66 (1981) 350–357.

[46] R. Wardle, G.W. Brindley, The crystal structures of pyrophyllite, 1Te, and of its dehydroxylate, Am. Mineral. 57 (1972) 732–750.

[47] A. Wang, J.J. Freeman, B.L. Jolliff, Understanding the Raman spectral features of phyllosilicates, J. Raman Spectrosc. 46 (2015) 829–845.

[48] J. Kloprogge, Chapter 6 - Raman spectroscopy of clay minerals, in: W.P. Gates, J.T. Kloprogge, J. Madejová, F. Bergaya (Eds.), Infrared and Raman Spectroscopies of Clay Minerals, in: Developments in Clay Science, vol. 8, 2017, pp. 150–199.

[49] B. Lafuente, R.T. Downs, H. Yang, N. Stone, 1. The power of databases: The RRUFF project, 2015, pp. 1–30.

[50] P. Nemes-Incze, Z. Osváth, K. Kamarás, L.P. Bíró, Anomalies in thickness measurements of graphene and few layer graphite crystals by tapping mode atomic force microscopy, Carbon 46 (2008) 1435–1442.

[51] K.-S. Kim, H.-J. Lee, C. Lee, S.-K. Lee, H. Jang, J.-H. Ahn, et al., Chemical vapor deposition-grown graphene: The thinnest solid lubricant, ACS Nano 5 (2011) 5107–5114.

[52] B. Vasić, A. Matković, U. Ralević, M. Belić, R. Gajić, Nanoscale wear of graphene and wear protection by graphene, Carbon 120 (2017) 137–144.

[53] A. Özoğul, E. Gnecco, M.Z. Baykara, Nanolithography-induced exfoliation of layered materials, Appl. Surf. Sci. 6 (2021) 100146.

[54] Y.-T. Fu, G.D. Zartman, M. Yoonessi, L.F. Drummy, H. Heinz, Bending of layered silicates on the nanometer scale: Mechanism, stored energy, and curvature limits, J. Phys. Chem. C 115 (2011) 22292–22300.

[55] X. Qin, J. Zhao, J. Wang, M. He, Atomic structure, electronic and mechanical properties of pyrophyllite under pressure: A first-principles study, Minerals 10 (2020) 778.

[56] A. Castellanos-Gomez, M. Poot, A. Amor-Amorós, G.A. Steele, H.S.J. van der Zant, N. Agraït, G. Rubio-Bollinger, Mechanical properties of freely suspended atomically thin dielectric layers of mica, Nano Res. 5 (2012) 550–557.

[57] G.D. Zartman, H. Liu, B. Akdim, R. Pachter, H. Heinz, Nanoscale tensile, shear, and failure properties of layered silicates as a function of cation density and stress, J. Phys. Chem. C 114 (2010) 1763–1772.

[58] B. Vasić, A. Matković, R. Gajić, I. Stanković, Wear properties of graphene edges probed by atomic force microscopy based lateral manipulation, Carbon 107 (2016) 723–732.

[59] R. Buzio, A. Gerbi, S. Uttiya, C. Bernini, A.E. Del Rio Castillo, F. Palazon, A.S. Siri, V. Pellegrini, L. Pellegrino, F. Bonaccorso, Ultralow friction of ink-jet printed graphene flakes, Nanoscale 9 (2017) 7612–7624.

[60] M. Fox, Optical Properties of Solids, Oxford University Press, 2010.

[61] P. Makuła, M. Pacia, W. Macyk, How to correctly determine the band gap energy of modified semiconductor photocatalysts based on UV–Vis spectra, J. Phys. Chem. Lett. 9 (2018) 6814–6817.

[62] G. Cassabois, P. Valvin, B. Gil, Hexagonal boron nitride is an indirect bandgap semiconductor, Nat. Photonics 10 (2016) 262–266.

[63] G.-H. Lee, Y.-J. Yu, C. Lee, C. Dean, K.L. Shepard, P. Kim, J. Hone, Electron tunneling through atomically flat and ultrathin hexagonal boron nitride, Appl. Phys. Lett. 99 (2011) 243114.

[64] L. Britnell, R.V. Gorbachev, R. Jalil, B.D. Belle, F. Schedin, M.I. Katsnelson, L. Eaves, S.V. Morozov, A.S. Mayorov, N.M.R. Peres, A.H. Castro Neto, J. Leist, A.K. Geim, L.A. Ponomarenko, K.S. Novoselov, Electron tunneling through ultrathin boron nitride crystalline barriers, Nano Lett. 12 (2012) 1707–1710.

[65] Y. Hattori, T. Taniguchi, K. Watanabe, K. Nagashio, Layer-by-layer dielectric breakdown of hexagonal boron nitride, ACS Nano 9 (2015) 916–921.

[66] Y.Y. Illarionov, T. Knobloch, M. Jech, M. Lanza, D. Akinwande, M.I. Vexler, T. Mueller, M.C. Lemme, G. Fiori, F. Schwierz, T. Grasser, Insulators for 2D nanoelectronics: the gap to bridge, Nature Commun. 11 (2020) 3385.

[67] K.K. Kim, H.S. Lee, Y.H. Lee, Synthesis of hexagonal boron nitride heterostructures for 2D van der Waals electronics, Chem. Soc. Rev. 47 (2018) 6342–6369.

[68] F. Giannazzo, G. Fisichella, G. Greco, P. Fiorenza, F. Roccaforte, Conductive atomic force microscopy of two-dimensional electron systems: From AlGaN/GaN heterostructures to graphene and MoS_2, in: M. Lanza (Ed.), Conductive Atomic Force Microscopy: Applications in Nanomaterials, WILEY-VCH Verlag, Weinheim, Germany, 2017, pp. 163–186, Ch. 7.

[69] F. Giannazzo, G. Greco, F. Roccaforte, C. Mahata, M. Lanza, Conductive AFM of 2D materials and heterostructures for nanoelectronics, in: U. Celano (Ed.), Electrical Atomic Force Microscopy for Nanoelectronics, Springer, Berlin, Germany, 2019, pp. 303–350, Ch. 10.

[70] C.-Y. Zhu, J.-K. Qin, P.-Y. Huang, H.-L. Sun, N.-F. Sun, Y.-L. Shi, L. Zhen, C.-Y. Xu, 2D indium phosphide sulfide ($In_2P_3S_9$): An emerging van der Waals high-k dielectrics, Small 18 (2022) 2104401.

[71] Y. Ji, C. Pan, M. Zhang, S. Long, X. Lian, F. Miao, F. Hui, Y. Shi, L. Larcher, E. Wu, M. Lanza, Boron nitride as two dimensional dielectric: Reliability and dielectric breakdown, Appl. Phys. Lett. 108 (2016) 012905.

[72] A. Ranjan, N. Raghavan, M. Holwill, K. Watanabe, T. Taniguchi, K.S. Novoselov, K.L. Pey, S.J. O'Shea, Dielectric breakdown in single-crystal hexagonal boron nitride, ACS Appl. Electron. Mater. 3 (2021) 3547–3554.

[73] J.L. Rosenholtz, D.T. Smith, The dielectric constant of mineral powders, Am. Mineral. 21 (1936) 115–120.

Optical conductivity and vibrational spectra of the narrow-gap semiconductor FeGa₃

C. Martin [1] V. A. Martinez,[2] M. Opačić [3] S. Djurdjić-Mijin [3] P. Mitrić [3] A. Umićević [4] A. Poudel [1] I. Sydoryk [1]
Weijun Ren [5,6] R. M. Martin [7] D. B. Tanner [2] N. Lazarević [3] C. Petrovic [5] and D. Tanasković [3]

[1]*School of Theoretical and Applied Sciences, Ramapo College of New Jersey, Mahwah, New Jersey 07430, USA*
[2]*Department of Physics, University of Florida, Gainesville, Florida 32611, USA*
[3]*Institute of Physics Belgrade, University of Belgrade, Pregrevica 118, 11080 Belgrade, Serbia*
[4]*Vinča Institute of Nuclear Sciences, National Institute of the Republic of Serbia, University of Belgrade,*
P.O. Box 522, 11001 Belgrade, Serbia
[5]*Condensed Matter Physics and Materials Science Department, Brookhaven National Laboratory, Upton, New York 11973, USA*
[6]*Shenyang National Laboratory for Materials Science, Institute of Metal Research, Chinese Academy of Sciences, Shenyang 110016, China*
[7]*Department of Physics and Astronomy, Montclair State University, Montclair, New Jersey 07043, USA*

Intermetallic narrow-gap semiconductors have been intensively explored due to their large thermoelectric power at low temperatures and a possible role of strong electronic correlations in their unusual thermodynamic and transport properties. Here we study the optical spectra and vibrational properties of FeGa₃ single crystal. The optical conductivity indicates that FeGa₃ has a direct band gap of ≈ 0.7 eV, consistent with density functional theory (DFT) calculations. Most importantly, we find a substantial spectral weight also below 0.4 eV, which is the energy of the indirect (charge) gap found in resistivity measurements and *ab initio* calculations. We find that the spectral weight below the gap decreases with increasing temperature, which indicates that it originates from the impurity states and not from the electronic correlations. Interestingly, we did not find any signatures of the impurity states in vibrational spectra. The infrared and Raman vibrational lines are narrow and weakly temperature dependent. The vibrational frequencies are in excellent agreement with our DFT calculations, implying a modest role of electronic correlations. Narrow Mössbauer spectral lines also indicate high crystallinity of the sample.

I. INTRODUCTION

Correlated narrow-gap semiconductors represent a class of materials known for their large thermopower at low temperatures and other anomalous transport and thermodynamic properties [1]. Three iron compounds among them, FeSi, FeSb₂, and FeGa₃, share some common features, but also show important differences. FeSi and FeSb₂ behave as insulators only at temperatures $T^* \lesssim 100$ K which corresponds to the energy much smaller than the band gap $E_g \approx 50$ meV [2–4]. A buildup of the in-gap spectral weight at temperatures $k_B T^* \ll E_g$, clearly seen in optical [5–8] and photoemission spectroscopy [9], is a signature of strong electronic correlations [10,11]. A crossover from a nonmagnetic insulator to a bad metal is accompanied by a large increase in the spin susceptibility which obtains Curie-Weiss form above room temperature [12,13]. This crossover leaves fingerprints also in the Raman vibrational spectra which become strongly temperature dependent. The width of vibrational peaks increases several times in the bad-metal region as compared to the low-temperature insulating state [14–16]. At temperatures near 10 K there is a large peak in the thermopower $|S|$ [17,18]. The exact role of the electronic correlations, in-gap states, anisotropy, and phonon drag in colossal thermopower found in FeSb₂ remains a subject of various studies and controversy [19–21].

FeGa₃ has a significantly larger band gap, $E_g \approx 0.4$ eV [22,23], than FeSi and FeSb₂ due to the stronger hybridization between 3*d* orbitals of Fe and 4*p* orbitals of Ga. The electronic structure calculations imply modest contribution of electronic correlations. Density functional theory (DFT) [24] and LDA+*U* [23] calculations give almost the same band structure, while dynamical mean field theory (DFT+DMFT) [25] gives only slightly reduced band gap. Nevertheless, the temperature dependence of dc resistivity is nontrivial: it strongly deviates from a simple activated transport at low temperatures, and features four distinct transport regimes which are associated with a presence of the in-gap states [22,23,25]. For $T \lesssim 5$ K ρ_{dc} has a power law temperature dependence consistent with the variable-range hopping transport driven by the localized in-gap states. In the interval $20 \lesssim T \lesssim 45$ K the charge transport is activated, but corresponds to a small gap of ≈ 40 meV between the in-gap states and the conduction band. Then, following a minimum in ρ_{dc}, there is a metalliclike transport up to ≈ 80 K which presumably corresponds to the regime where most of the in-gap electrons are already transferred to the conduction band. For $T > 300$ K the charge transport is activated, consistent with the wide gap $E_g \approx 0.4$ eV. The measurements show weak sample anisotropy and weak temperature dependence of magnetic susceptibility, whereas the DFT+DMFT calculations give small mass renormalization, as well as strong charge and spin

fluctuations [25]. A maximum in the Seebeck coefficient $|S|$ at $T \approx 15$ K is argued to be a consequence of the phonon-drag effect [23]. In this picture the in-gap states supply free charge carriers and the acoustic phonons cause an additional scattering of the electrons opposite to the direction of a temperature gradient, leading to the large thermoelectric power. Interestingly, to our knowledge, there has been so far only one infrared spectroscopy study of FeGa$_3$ in polycrystalline samples [26], restricted to room temperature and energies larger than 90 meV.

In this paper, we present infrared and Raman spectroscopy study of FeGa$_3$ single crystal in the temperature range between 4 and 300 K. The reflectance is measured in the energy interval between 30 and 24 000 cm^{-1}. The infrared and Raman active vibrational frequencies are in excellent agreement with our DFT calculations, indicating good crystallinity and a small influence of electronic correlations. Good crystallinity is corroborated also by measured Mössbauer spectra. The most prominent feature of the optical spectra is the existence of the in-gap states below the charge gap of approximately 0.4 eV. We observe a reduction of the in-gap spectral weight as the temperature increases to 300 K and conclude that this spectral weight originates from the impurities. Details of experimental and numerical methods are presented in Sec. II. The results are shown in Secs. III and IV contains our conclusions.

II. METHODS

Single crystals of FeGa$_3$ were grown as described previously [22]. For infrared measurements a small crystal was polished until a smooth surface of about 3 mm^2 area was obtained, then mounted on a helium-flow optical cryostat. The temperature dependence of reflectance was measured between 30 and 24 000 cm^{-1}, using a combination of two Fourier-transform infrared spectrometers: a Bruker 113v for far infrared (30–600 cm^{-1}) and a Bruker Vertex 70, with extended spectral range, from midinfrared to visible (100–24 000 cm^{-1}). Reflectance in visible and ultraviolet (12 000–50 000 cm^{-1}) was measured at room temperature only, using a Perkin-Elmer 650 UV/VIS grating spectrometer. As no temperature dependence was observed above about 12 000 cm^{-1}, all temperatures were merged with room temperature data in visible and ultraviolet parts of the spectrum. To capture correctly the width and line shape of lattice vibrations, the far-IR data were taken with a resolution of 0.5 cm^{-1}, while 2 cm^{-1} or larger values were used at higher frequencies. Both gold and aluminum mirrors were used for reference, and in order to correct for surface roughness the sample was also gold coated, using a commercial Ted Pella Cressington 108 sputtering machine. Because of the polishing involved, the precise orientation of the electric field (polarization) with respect to the crystallographic axes of the samples is not clearly defined, hence we cannot discuss potential anisotropic optical properties.

Raman scattering measurements were performed using a TriVista557 Raman system, equipped with a nitrogen-cooled CCD detector, in backscattering micro-Raman configuration. Grating configuration was 1800/1800/2400 grooves/mm, in order to achieve the best possible resolution. The 514.5-nm line of an Ar+/Kr+ gas laser was used as an excitation source and a microscope objective with factor 50 magnification was used for focusing the beam. All measurements were carried out with laser power less than 1.5 mW at the sample, in order to minimize local heating. Room temperature measurements were done in air, whereas for low temperature measurements the sample was placed in a KONTI CryoVac continuous flow cryostat, with a 0.5-mm-thick window. Spectra were corrected for the Bose factor.

The ^{57}Fe-Mössbauer spectrum of the FeGa$_3$ powdered sample was measured at room temperature in high ($\approx \pm 9$ mm/s) and low ($\approx \pm 2$ mm/s) Doppler velocity range. The spectra were collected in standard transmission geometry in constant acceleration mode using a ^{57}Co(Rh) source. The Doppler velocity scale was calibrated by using the Mössbauer spectrum of metallic α-Fe. The spectra were fitted by the RECOIL program [27]. The center shift value (CS) is quoted relative to the α-Fe (CS $= 0$).

First-principles DFT calculations of electronic structure and phonon frequencies were performed using the open-source QUANTUM-ESPRESSO package [28,29]. We employed the ultrasoft Vanderbilt-type pseudopotentials with Perdew-Burke-Ernzerhof exchange and correlation functional. For the Fe atom we considered $3s$, $3p$, $3d$, and $4s$ as valence electrons (in total 16), while the Ga valence electrons were taken to be the electrons from $3d$, $4s$, and $4p$ orbitals (in total 13). Thus, a minimum of 110 bands was needed to perform the calculations since we have four formula units per unit cell, but we nevertheless considered 128 bands, which is a very convenient number for parallelization purposes. The plane wave kinetic energy cutoff was set to 70 Ry, which proved to be sufficient for all our calculations. The ionic relaxation, self-consistent, and normal mode calculations were performed using the Monkhorst-Pack scheme, with the k mesh of $8 \times 8 \times 8$, which corresponds to 75 k points in the irreducible part of the Brillouin zone. On the other hand, the density of states (DOS) calculation requires a much larger number of k points in order to be accurate, and hence we performed the non-self-consistent calculation with a k mesh of $12 \times 12 \times 12$ in order to calculate the DOS. We used density functional perturbation theory (DFPT) [30] in order to calculate the vibrational frequencies.

III. RESULTS

We first present the band structure calculations. These results are known from the literature, but we nevertheless show them for completeness and in order to put into context the analysis of the experimental data that follow. Then we present optical, Raman, and Mössbauer spectra.

A. DFT band structure

The semiconductor FeGa$_3$ belongs to the $P4_2/mnm$ space group and it has a tetragonal P-type lattice with lattice parameters $a = 6.2628(3)$ Å and $c = 6.5546(5)$ Å [31]. In the DFT calculations we used the lattice parameters from the experiment and relaxed only the fractional coordinates of the atoms. These coordinates, shown in Table I, are only slightly adjusted from their measured values.

TABLE I. Nonequivalent atomic positions from the DFT calculation.

Atom	$P\bar{4}n2$	x	y	z
Fe	$4f$	0.34367	0.34367	0
Ga1	$4c$	0	0.5	0
Ga2	$8j$	0.15575	0.15575	0.26295

Figure 1 shows the dispersion relations and the density of states, calculated along the k path Z-R-A-Z-Γ-X-M-Γ in the Brillouin zone. Our results are very similar to previous work [23,32], showing that FeGa$_3$ is an indirect-gap semiconductor with the calculated band gap of 0.44 eV. The bands around the Fermi level are formed from the hybridized Fe $3d$ and Ga $4p$ orbitals.

B. Optical conductivity and infrared vibrational modes

The reflectance $R(\omega)$ measured at several temperatures between 25 and 300 K is shown in Fig. 2(a). Note that the spectra are shown on a logarithmic frequency scale so that we can distinguish both the low- and high-frequency features. The low-frequency reflectance is close to 1 which indicates a possible presence of the in-gap states that we will discuss in detail below. The far-infrared frequency region is shown on a linear scale in the inset. The peaks in $R(\omega)$ correspond to the infrared-active vibrational modes.

A better insight into the excitation spectrum can be obtained from the real part of the optical conductivity $\sigma_1(\omega)$. It corresponds to the imaginary part of the dielectric function, $\sigma_1(\omega) = \omega\epsilon_2(\omega)/4\pi$, describing the absorption of electromagnetic radiation [33,34]. Figure 2(b) shows $\sigma_1(\omega)$ obtained from the Kramers-Kronig transformation of $R(\omega)$. As this transformation involves integration of $R(\omega)$ from zero to infinity, we used extrapolation of our measurements. At high frequency ($\omega \to \infty$), the data were bridged with calculations of the dielectric function based on the x-ray photoabsorption, following the procedure described in Ref. [35]. For $\omega < 30\,\mathrm{cm}^{-1}$ we set $R(\omega) = R(30\,\mathrm{cm}^{-1})$, but we checked that $\sigma_1(\omega)$ is not sensitive to the precise form of $R(\omega)$ in the
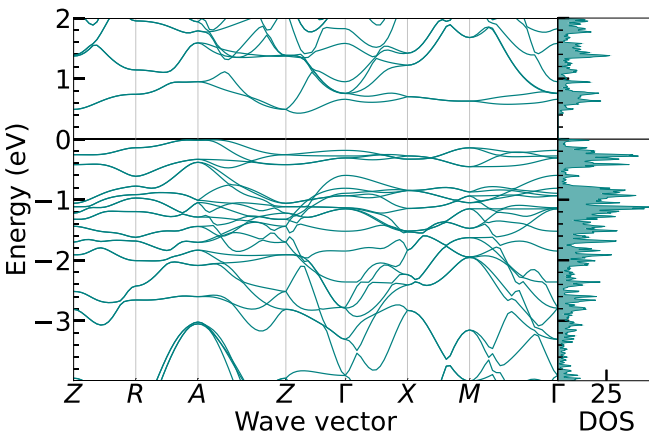
FIG. 2. Reflectance (a) and optical conductivity (b) as a function of frequency in the whole measured frequency range at several temperatures. The insets show the low-frequency data on a linear scale.

FIG. 1. DFT band structure of FeGa$_3$ and density of states in units states/(eV f.u.).

limit $\omega \to 0$. The same result is obtained using the Hagen-Rubens formula, $R(\omega) = 1 - A\sqrt{\omega}$, where A is a constant adjusted to fit the first several points from the measurements [33,34].

The optical conductivity at 25 and 300 K is shown in Fig. 3 on a linear energy (frequency) scale in units of eV. $\sigma_1(\omega)$ rapidly decreases for frequencies $\hbar\omega \lesssim 0.9$ eV (7000 cm^{-1}). This is consistent with the DFT band structure shown in Fig. 1. It gives the smallest direct gap of 0.67 eV near the Z point in the Brillouin zone, but in many regions of the Brillouin zone the gap is between 0.7 and 0.9 eV. At $\hbar\omega = E_g \approx 0.4$ eV the spectral weight is significantly reduced, yet it remains substantial also at $\hbar\omega < E_g$. We note that we did not attempt to calculate the optical spectra since a reliable calculation requires us to include the particle-hole interaction on a level of the Bethe-Salpeter equation, which is a very challenging task even for weakly interacting semiconductors [36,37]. A calculation of the optical spectra of FeGa$_3$ in the independent-particle approach poorly compares with our experiments [24]. On the other hand, our optical spectra for $\hbar\omega \gtrsim 0.5$ eV are

FIG. 3. Optical conductivity as a function of frequency at 25 and 300 K. The inset shows the infrared vibrational modes which are fitted by 11 Lorentzians. The green line corresponds to the cumulative fit.
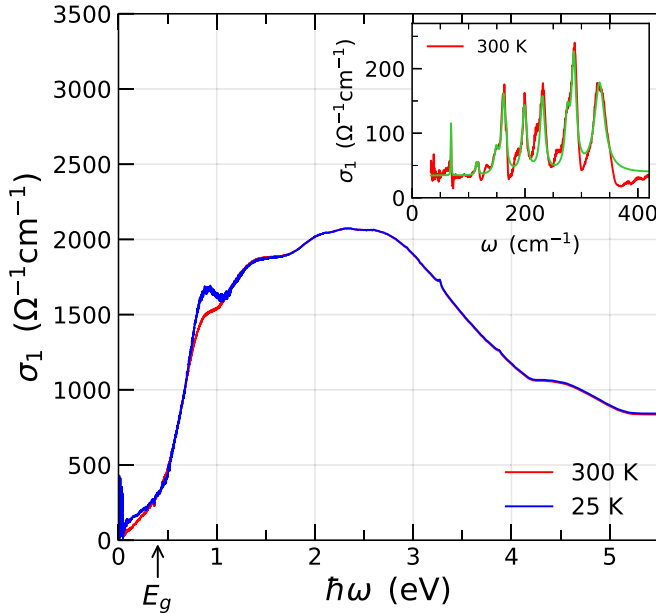
TABLE II. Irreducible representation of infrared-active modes and their frequencies. The measured frequencies are obtained at 300 K. Numerical values are obtained within DFPT calculation.

Irred. rep.	Expt. (cm^{-1})	Calc. (cm^{-1})
$E_u^{1,2}$	69.00	76.08
A_{2u}^1	113.50	107.61
$E_u^{3,4}$	117.50	116.18
$E_u^{5,6}$	149.85	161.78
A_{2u}^2	162.2	162.28
$E_u^{7,8}$	166.99	168.69
$E_u^{9,10}$	199.50	201.71
$E_u^{11,12}$	231.50	229.45
$E_u^{13,14}$	275.00	281.2
A_{2u}^3	287.30	296.61
$E_u^{15,16}$	332.50	329.0

in rather good agreement with the spectra on polycrystalline samples of Ref. [26].

Evidence that the spectral weight below E_g has origins in the impurity states can be obtained from analysis of the temperature dependence of $\sigma_1(\omega)$. At finite temperatures, in a standard band gap semiconductor a small spectral weight would appear just below E_g due to the phonon assisted excitations. The same amount of the spectral weight would recover just above the band edge, where the absorption becomes slightly lower due to the finite hole (electron) concentration in the valence (conduction) band at finite temperatures [33]. On the other hand, in FeSi and FeSb$_2$ a spectral gap is closed at higher temperatures due to the strong correlation effects. In this case, transfers of the spectral weight occur over the energy range much larger than the band gap. However, in our case the spectral weight at $T = 300$ K is reduced both below and above E_g [see Figs. 2(b) and 3]. The reduction of the spectral weight below E_g should correspond to the depopulation of the impurity band, which leads to the reduction in the light absorption for subgap energies [25]. Hence, we conclude that the spectral weight below E_g is due to impurity states. We note that a small surplus of Fe atoms in comparison to the stoichiometric ratio is found in wavelength dispersive x-ray spectroscopy [23]. Our conclusion is in line with the statement that the transfer of the electrons from the impurity states to the conduction band is a likely cause of the anomalous $d\rho/dT > 0$ resistivity temperature dependence around 100 K [20,25].

We now turn our attention to the far-infrared part of the spectrum from 50 to 350 cm^{-1}, which contains infrared vibrational modes. From the inset of Fig. 2(b) it appears that most of the phonon peaks are rather broad. However, that is not the case since several peaks, in fact, consist of two vi-

brational modes with very close frequencies. The space group $P4_2/mnm$ has the corresponding point group $D_{4h}(4/mmm)$. Thus, all the normal modes are classified according to irreducible representations of $D_{4h}(4/mmm)$. The factor group analysis predicts 12 Raman and 11 infrared-active modes, along with ten silent and two acoustic modes:

$$\Gamma_{\text{Raman}} = 3A_{1g} + 4E_g + 2B_{1g} + 3B_{2g},$$
$$\Gamma_{\text{IR}} = 3A_{2u} + 8E_u,$$
$$\Gamma_{\text{silent}} = 2A_{2g} + 2A_{2u} + 4B_{1u} + 2B_{2u},$$
$$\Gamma_{\text{acoustic}} = A_{2u} + E_u. \tag{1}$$

The experimental data at 300 K are fitted with 11 Lorentz profile lines. Their cumulative contribution to the spectra is shown in green color in the inset of Fig. 3. A complete list of the corresponding phonon frequencies is shown in Table II. These frequencies were obtained at 300 K, but we see from the inset in Fig. 2(b) that the temperature dependence of the frequencies is weak. The changes are of the order of 1% in the temperature range between 25 and 300 K. The frequencies calculated within DFPT are in excellent agreement with measured frequencies. This implies that a crystallinity of the sample is very good, even though some surplus of Fe iron atoms is expected in comparison to the ideal composition [23]. In addition, excellent agreement between the calculated and measured frequencies indicates that the electronic correlations beyond the DFT are not strong, in line with the conclusions from DFT+U [23] and DFT+DMFT [25] calculations.

C. Raman spectra

There are 12 Raman-active modes in FeGa$_3$ [see Eq. (1)]. Wyckoff positions of the atoms, their contributions to the Γ-point phonons, and the corresponding tensors for Raman active modes are given in Table III. Since observability of the Raman-active modes in backscattering configuration of the experiment strongly depends on the orientation of the sample, we first performed orientation dependent measurements. This was done by rotating the sample in the steps of 10°. The orientation of the sample which provided the best observability

TABLE III. Contributions of each atom to the Γ-point phonons for the $P4_2/mnm$ space group and the corresponding tensors for Raman active modes.

Space group $P4_2/mnm$	
Atoms	Irreducible representations
Fe ($4f$)	$A_{1g} + A_{2g} + A_{2u} + B_{1g}$
	$+B_{1u} + B_{2g} + E_g + 2E_u$
Ga ($4c$)	$A_{1u} + A_{2u} + B_{1u} + B_{2u} + 4E_u$
Ga ($8j$)	$2A_{1g} + A_{1u} + A_{2g} + A_{2u} + B_{1g}$
	$+2B_{1u} + 2B_{2g} + B_{2u} + 3E_g + 3E_u$

$$A_{1g} = \begin{pmatrix} a & 0 & 0 \\ 0 & a & 0 \\ 0 & 0 & b \end{pmatrix} \quad B_{1g} = \begin{pmatrix} c & 0 & 0 \\ 0 & -c & 0 \\ 0 & 0 & 0 \end{pmatrix} \quad B_{2g} = \begin{pmatrix} 0 & d & 0 \\ d & 0 & 0 \\ 0 & 0 & 0 \end{pmatrix}$$

$${}^1E_g = \begin{pmatrix} c & 0 & 0 \\ 0 & 0 & e \\ 0 & e & 0 \end{pmatrix} \quad {}^2E_g = \begin{pmatrix} 0 & 0 & -e \\ 0 & 0 & 0 \\ -e & 0 & 0 \end{pmatrix}$$

of Raman modes of various symmetries was used in further measurements.

Raman spectra of FeGa$_3$ single crystals, measured from the (011) plane of the sample, at temperature $T = 100$ K, for polarization angles within the range of 0° and 180° are presented in Fig. 4. We have identified 10 out of 12 Raman active modes. The assignation of modes was done in accordance with DFT calculations and polarization measurements. Peaks that exhibit the same polarization dependence were assigned with the same symmetry. Consequently, peaks at 146.58 and 331.80 cm^{-1} were assigned as A_{1g} and peaks at 127.99 and 269.98 cm^{-1} were assigned as B_{1g}. The phonon lines at 138.96, 179.01, and 264.40 cm^{-1} are assigned as E_g, whereas modes at 161.67, 238.27, and 321.43 cm^{-1} correspond to the B_{2g} symmetry modes. The full list of measured phonon

TABLE IV. Experimental Raman frequencies measured at 100 K and the corresponding values calculated within DFPT.

Irred. rep.	Expt. (cm^{-1})	Calc. (cm^{-1})
$E_g^{1,2}$		86.81
B_{1g}^1	127.99	125.52
$E_g^{3,4}$	138.96	139.06
A_{1g}^1	146.58	145.89
B_{2g}^1	161.67	161.51
$E_g^{5,6}$	179.01	165.09
A_{1g}^2		180.12
B_{2g}^2	238.27	239.62
$E_g^{7,8}$	264.40	258.94
B_{1g}^2	269.28	262.96
B_{2g}^3	321.43	318.53
A_{1g}^3	331.80	322.41

frequencies, along with their calculated values, is shown in Table IV.

There is a very good agreement between experimental and calculated phonon frequencies, with a discrepancy of less than 8%. A close match in experimental and theoretical results is not surprising knowing that the investigated material is semiconducting, with moderate electronic correlations. All of the observed phonon lines are sharp, with the full width at half maximum (FWHM) ≈ 2 cm^{-1}, and weakly temperature dependent. This indicates a good crystallinity of the sample and absence of a metal-insulator transition or magnetic ordering.
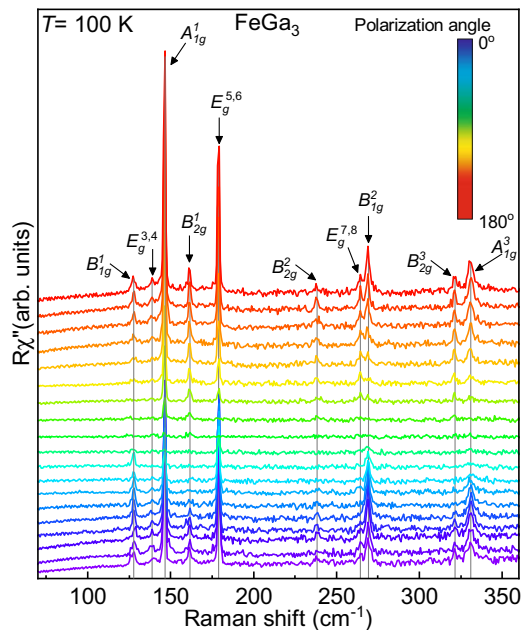

FIG. 4. Polarization-dependent Raman spectra of FeGa$_3$ single crystals. Measurements were performed with measuring step of 10° at temperature $T = 100$ K.
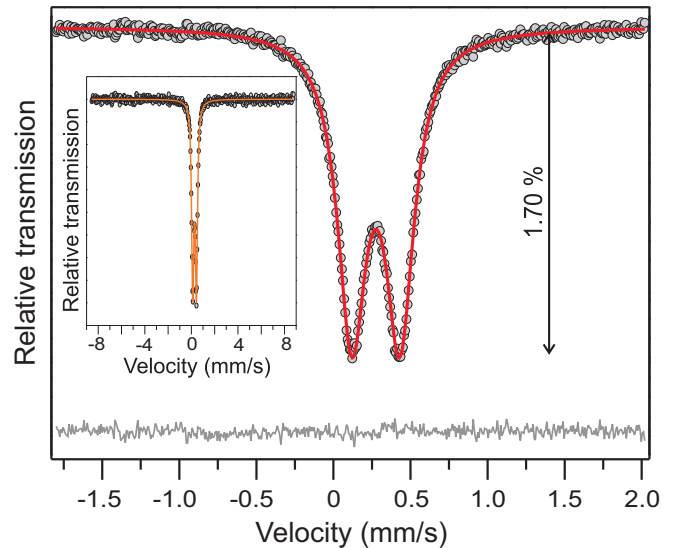
FIG. 5. Room temperature ^{57}Fe-Mössbauer spectra of the FeGa$_3$ sample recorded in the low-velocity range. Experimental data are presented by the solid circles and the fit is given by the red solid line. The difference (Calc. − Expt.) is shown by the dark gray line at the bottom of the figure. The vertical arrow denotes the relative position of the lowest experimental point with respect to the background (relative absorption of 1.70%). The absolute difference is less than 0.05%. The inset shows the room temperature spectrum of the FeGa$_3$ sample recorded within the high-velocity range. The orange line is just a guide for the eye.

D. Mössbauer spectra

The ^{57}Fe-Mössbauer spectroscopy was used to investigate quality and ordering of the prepared sample and to check for the presence of Fe-based impurity phases. The ^{57}Fe-Mössbauer spectra of the FeGa$_3$ are presented in Fig. 5. The spectrum recorded in the low-velocity range showed two absorption lines (doublet). In the spectrum recorded in the high-velocity range, beside the observed doublet, there is no indication of the magnetic hyperfine splitting. The thickness corrected FeGa$_3$ spectrum recorded in the low-velocity range was fitted with one Lorentzian-shaped doublet using the RECOIL program [27]. The obtained Mössbauer parameters for the measured doublet are center shift CS $= 0.28$ mm/s, quadrupole splitting $\Delta = 0.31$ mm/s, and FWHM of the Lorentzian lines is 0.22 mm/s. The obtained results closely match the hyperfine parameters for FeGa$_3$ from the literature [38–42]. A very small broadening of the resonance lines observed in the experiment is a strong indication that the sample is very well ordered and of high crystallinity.

IV. CONCLUSIONS

In summary, we have performed optical, Raman, and Mössbauer spectroscopy measurements of a narrow-gap semiconductor FeGa$_3$, along with DFT band structure and vibrational frequencies calculation. We find that the optical conductivity decreases for frequencies below $\hbar\omega \approx 0.9$ eV consistent with the direct band gap observed in DFT calculations. Our most important finding is the appearance of the optical spectral weight below the charge (indirect) gap $E_g \approx 0.4$ eV. At room temperature the spectral weight below E_g diminishes as compared to the one at $T = 25$ K. Therefore, we conclude that this spectral weight originates from the impurities and not from the correlation effects. Interestingly, we do not find signatures of the impurities in the vibrational spectra. Both the infrared and Raman lines are very narrow, as well as the Mössbauer spectral lines, which implies a good crystallinity of the sample. The calculated vibrational frequencies are in a very good agreement with the measurements, which indicates that the electronic correlations in FeGa$_3$ are not strong, in line with previous studies.

[1] J. M. Tomczak, Thermoelectricity in correlated narrow-gap semiconductors, J. Phys.: Condens. Matter **30**, 183001 (2018).

[2] Z. Schlesinger, Z. Fisk, H.-T. Zhang, M. B. Maple, J. DiTusa, and G. Aeppli, Unconventional Charge Gap Formation in FeSi, Phys. Rev. Lett. **71**, 1748 (1993).

[3] C.-H. Park, Z.-X. Shen, A. G. Loeser, D. S. Dessau, D. G. Mandrus, A. Migliori, J. Sarrao, and Z. Fisk, Direct observation of a narrow band near the gap edge of FeSi, Phys. Rev. B **52**, R16981 (1995).

[4] C. Petrovic, J. W. Kim, S. L. Bud'ko, A. I. Goldman, P. C. Canfield, W. Choe, and G. J. Miller, Anisotropy and large magnetoresistance in the narrow-gap semiconductor FeSb$_2$, Phys. Rev. B **67**, 155205 (2003).

[5] A. Damascelli, K. Schulte, D. van der Marel, and A. A. Menovsky, Infrared spectroscopic study of phonons coupled to charge excitations in FeSi, Phys. Rev. B **55**, R4863 (1997).

[6] M. A. Chernikov, L. Degiorgi, E. Felder, S. Paschen, A. D. Bianchi, H. R. Ott, J. L. Sarrao, Z. Fisk, and D. Mandrus, Low-temperature transport, optical, magnetic and thermodynamic properties of Fe$_{1-x}$Co$_x$Si, Phys. Rev. B **56**, 1366 (1997).

[7] A. Perucchi, L. Degiorgi, R. Hu, C. Petrovic, and V. F. Mitrović, Optical investigation of the metal-insulator transition in FeSb$_2$, Eur. Phys. J. B **54**, 175 (2006).

[8] A. Herzog, M. Marutzky, J. Sichelschmidt, F. Steglich, S. Kimura, S. Johnsen, and B. B. Iversen, Strong electron correlations in FeSb$_2$: An optical investigation and comparison with RuSb$_2$, Phys. Rev. B **82**, 245205 (2010).

[9] M. Arita, K. Shimada, Y. Takeda, M. Nakatake, H. Namatame, M. Taniguchi, H. Negishi, T. Oguchi, T. Saitoh, A. Fujimori, and T. Kanomata, Angle-resolved photoemission study of the strongly correlated semiconductor FeSi, Phys. Rev. B **77**, 205117 (2008).

[10] J. M. Tomczak, K. Haule, T. Miyake, A. Georges, and G. Kotliar, Thermopower of correlated semiconductors: Application to FeAs$_2$ and FeSb$_2$, Phys. Rev. B **82**, 085104 (2010).

[11] J. M. Tomczak, K. Haule, and G. Kotliar, Signatures of electronic correlations in iron silicide, Proc. Natl. Acad. Sci. USA **109**, 3243 (2012).

[12] V. Jaccarino, G. K. Wertheim, J. H. Wernick, L. R. Walker, and S. Arajs, Paramagnetic excited state of FeSi, Phys. Rev. **160**, 476 (1967).

[13] T. Koyama, Y. Fukui, Y. Muro, T. Nagao, H. Nakamura, and T. Kohara, Nuclear quadrupole resonance study of the electronic properties of the narrow-gap semiconductor FeSb$_2$, Phys. Rev. B **76**, 073203 (2007).

[14] A.-M. Racu, D. Menzel, J. Schoenes, and K. Doll, Crystallographic disorder and electron-phonon coupling in Fe$_{1-x}$Co$_x$Si single crystals: Raman spectroscopy study, Phys. Rev. B **76**, 115103 (2007).

[15] N. Lazarević, Z. V. Popović, R. Hu, and C. Petrovic, Evidence for electron-phonon interaction in $Fe_{1-x}M_xSb_2$ ($M =$ Co and Cr; $0 \leqslant x \leqslant 0.5$) single crystals, Phys. Rev. B **81**, 144302 (2010).

[16] N. Lazarević, M. M. Radonjić, D. Tanasković, R. Hu, C. Petrovic, and Z. V. Popović, Lattice dynamics of $FeSb_2$, J. Phys.: Condens. Matter **24**, 255402 (2012).

[17] B. C. Sales, E. C. Jones, B. C. Chakoumakos, J. A. Fernandez-Baca, H. E. Harmon, J. W. Sharp, and E. H. Volckmann, Magnetic, transport, and structural properties of $Fe_{1-x}Ir_xSi$, Phys. Rev. B **50**, 8207 (1994).

[18] P. Sun, N. Oeschler, S. Johnsen, B. B. Iversen, and F. Steglich, Huge thermoelectric power factor: $FeSb_2$ versus $FeAs_2$ and $RuSb_2$, Appl. Phys. Express **2**, 091102 (2009).

[19] C. C. Homes, Q. Du, C. Petrovic, W. H. Brito, S. Choi, and G. Kotliar, Unusual electronic and vibrational properties in the colossal thermopower material $FeSb_2$, Sci. Rep. **8**, 11692 (2018).

[20] M. Battiato, J. M. Tomczak, Z. Zhong, and K. Held, Unified Picture for the Colossal Thermopower Compound $FeSb_2$, Phys. Rev. Lett. **114**, 236603 (2015).

[21] Q. Du, L. Wu, H. Cao, C.-J. Kang, C. Nelson, G. L. Pascut, T. Besara, T. Siegrist, K. Haule, G. Kotliar, I. Zaliznyak, Y. Zhu, and C. Petrovic, Vacancy defect control of colossal thermopower in $FeSb_2$, npj Quantum Mater. **6**, 13 (2021).

[22] Y. Hadano, S. Narazu, M. A. Avila, T. Onimaru, and T. Takabatake, Thermoelectric and magnetic properties of a narrow-gap semiconductor $FeGa_3$, J. Phys. Soc. Jpn. **78**, 013702 (2009).

[23] M. Wagner-Reetz, D. Kasinathan, W. Schnelle, R. Cardoso-Gil, H. Rosner, Y. Grin, and P. Gille, Phonon-drag effect in $FeGa_3$, Phys. Rev. B **90**, 195206 (2014).

[24] Z. P. Yin and W. E. Pickett, Evidence for a spin singlet state in the intermetallic semiconductor $FeGa_3$, Phys. Rev. B **82**, 155202 (2010).

[25] M. B. Gamża, J. M. Tomczak, C. Brown, A. Puri, G. Kotliar, and M. C. Aronson, Electronic correlations in $FeGa_3$ and the effect of hole doping on its magnetic properties, Phys. Rev. B **89**, 195102 (2014).

[26] Y. V. Knyazev and Y. I. Kuz'min, The study of the structure of the electronic states of the $FeGa_3$ and $RuGa_3$ compounds by optical spectroscopy method, Phys. Solid State **59**, 2244 (2017).

[27] K. Lagarec and D. G. Rancourt, RECOIL, *Mössbauer spectral analysis software for Windows* (University of Ottawa, Ottawa, Canada, 1998).

[28] P. Giannozzi, S. Baroni, N. Bonini, M. Calandra, R. Car, C. Cavazzoni, D. Ceresoli, G. L. Chiarotti, M. Cococcioni, I. Dabo, A. D. Corso, S. de Gironcoli, S. Fabris, G. Fratesi, R. Gebauer, U. Gerstmann, C. Gougoussis, A. Kokalj, M. Lazzeri, L. Martin-Samos *et al.*, Quantum espresso: a modular and open-source software project for quantum simulations of materials, J. Phys.: Condens. Matter **21**, 395502 (2009).

[29] P. Giannozzi, O. Andreussi, T. Brumme, O. Bunau, M. B. Nardelli, M. Calandra, R. Car, C. Cavazzoni, D. Ceresoli, M. Cococcioni, N. Colonna, I. Carnimeo, A. D. Corso, S. de Gironcoli, P. Delugas, R. A. DiStasio, A. Ferretti, A. Floris, G. Fratesi, G. Fugallo *et al.*, Advanced capabilities for materials modelling with quantum espresso, J. Phys.: Condens. Matter **29**, 465901 (2017).

[30] S. Baroni, S. de Gironcoli, A. Dal Corso, and P. Giannozzi, Phonons and related crystal properties from density-functional perturbation theory, Rev. Mod. Phys. **73**, 515 (2001).

[31] U. Häussermann, M. Boström, P. Viklund, O. Rapp, and T. Björnängen, $FeGa_3$ and $RuGa_3$: Semiconducting Intermetallic Compounds, J. Solid State Chem. **165**, 94 (2002).

[32] Y. Imai and A. Watanabe, Electronic structures of semiconducting $FeGa_3$, $RuGa_3$, $OsGa_3$, and $RuIn_3$ with the $CoGa_3$- or the $FeGa_3$-type structure, Intermetallics **14**, 722 (2006).

[33] F. Wooten, *Optical Properties of Solids* (Academic Press, New York, 1972).

[34] D. B. Tanner, *Optical Effects in Solids* (Cambridge University Press, New York, 2019).

[35] D. B. Tanner, Use of x-ray scattering functions in Kramers-Kronig analysis of reflectance, Phys. Rev. B **91**, 035123 (2015).

[36] S. Albrecht, L. Reining, R. Del Sole, and G. Onida, *Ab Initio* Calculation of Excitonic Effects in the Optical Spectra of Semiconductors, Phys. Rev. Lett. **80**, 4510 (1998).

[37] M. Rohlfing and S. G. Louie, Electron-hole excitations and optical spectra from first principles, Phys. Rev. B **62**, 4927 (2000).

[38] G. L. Whittle, P. E. Clark, and R. Cywinski, Vacancies and site occupation in Co-Ga-Fe alloys (Mössbauer study), J. Phys. F **10**, 2093 (1980).

[39] I. Dézsi, I. Szücs, C. Fetzer, and W. Keune, The local interactions of Co and Fe in β-phase $Co_x Ga_{(1-x)}$, Acta Mater. **46**, 3299 (1998).

[40] N. Tsujii, H. Yamaoka, M. Matsunami, R. Eguchi, Y. Ishida, Y. Senba, H. Ohashi, S. Shin, T. Furubayashi, H. Abe, and H. Kitazawa, Observation of energy gap in $FeGa_3$, J. Phys. Soc. Jpn. **77**, 024705 (2008).

[41] G. R. Hearne, S. Bhattacharjee, B. P. Doyle, M. A. M. Ahmed, P. Musyimi, E. Carleschi, and B. Joseph, Pressure-induced disruption of the local environment of Fe-Fe dimers in $FeGa_3$ accompanied by metallization, Phys. Rev. B **98**, 020101(R) (2018).

[42] D. Mondal, C. Kamal, S. Banik, A. Bhakar, A. Kak, G. Das, R. V. R., A. Chakrabarti, and T. Ganguli, Structural and electronic properties of $Fe(Al_x Ga_{1-x})_3$ system, J. Appl. Phys. **120**, 165102 (2016).

Correction: A typographical error in the fourth affiliation was introduced during the production cycle and has been fixed.

Book of abstracts

PHOTONICA2019

The Seventh International School and Conference on Photonics, 26 August – 30 August 2019, Belgrade, Serbia

& Machine Learning with Photonics Symposium (ML-Photonica 2019)

& ESUO Regional Workshop

ESUO
EUROPEAN
SYNCHROTRON
AND FEL USER
ORGANISATION

& COST action CA16221

AtomQT cost

Editors: Milica Matijević, Marko Krstić and Petra Beličev

Belgrade, 2019

ABSTRACTS OF TUTORIAL, KEYNOTE, INVITED LECTURES, PROGRESS REPORTS AND CONTRIBUTED PAPERS

of

The Seventh International School and Conference on Photonics
PHOTONICA2019, 26 August – 30 August 2019, Belgrade, Serbia

and
Machine Learning with Photonics Symposium

and
ESUO Regional Workshop

Committees:

Scientific committee:

Aleksandar Krmpot, Serbia
Antun Balaž, Serbia
Arlene D. Wilson-Gordon, Israel
Bojan Resan, Switzerland
Boris Malomed, Israel
Branislav Jelenković, Serbia
Dejan Gvozdić, Serbia
Detlef Kip, Germany
Dragan Indjin, United Kingdom
Edik Rafailov, United Kingdom
Feng Chen, China
Francesco Cataliotti, Italy
Giannis Zacharakis, Greece
Goran Isić, Serbia
Goran Mašanović, United Kingdom
Isabelle Philippa Staude, Germany
Jelena Radovanović, Serbia
Jerker Widengren, Sweden
Jovana Petrović, Germany
Laurent Sanchez, France
Ljupčo Hadžievski, Serbia
Marco Santagiustina, Italy
Milan Mashanović, United States of America
Milan Trtica, Serbia
Miloš Živanov, Serbia
Milutin Stepić, Serbia
Milivoj Belić, Qatar
Nikola Stojanović, Germany
Pavle Anđus, Serbia
Peđa Mihailović, Serbia
Peter Schaaf, Germany
Radoš Gajić, Serbia
Sergei Turitsyn, United Kingdom
Suzana Petrović, Serbia
Ticijana Ban, Croatia
Vladana Vukojević, Sweden
Zoran Jakšić, Serbia
Željko Šljivančanin, Serbia

Organizing Committee:

Petra Beličev (Chair)
Marko Krstić (Co-chair)
Milica Matijević (Secretary)
Goran Gligorić (Webmaster)
Ljupčo Hadžievski
Aleksandra Maluckov
Milutin Stepić
Maja Nešić
Marija Ivanović
Danka Stojanović
Marjan Miletić
Jelena Kršić
Mirjana Stojanović

ML-Photonica 2019
Symposium Steering Committee:

Sergei Turitsyn, United Kingdom
Darko Zibar, Denmark
Sugavam Srikanth, UK

Technical Organizer:

VII

Lattice dynamics of iron-based superconductors and related compounds

M. Opacic[1], N. Lazarevic[1], D. Tanaskovic[2], C. Petrovic[3] and Z.V.Popovic[1,4]

[1]*Center for Solid State Physics and New Materials, Institute of Physics Belgrade, University of Belgrade, Serbia*
[2]*Scientific Computing Laboratory, Center for the Study of Complex Systems,
Institute of Physics Belgrade University of Belgrade, Serbia*
[3]*Condensed Matter Physics and Materials Science Department,
Brookhaven National Laboratory, Upton, New York, USA*
[4]*Serbian Academy of Sciences and Arts, Belgrade, Serbia*
e-mail: marko.opacic@ipb.ac.rs

The lecture focuses on vibrational properties of some unconventional iron-based superconductors and related compounds by means of Raman spectroscopy. In the measured phonon spectra of superconducting $K_xFe_{2-y}Se_2$ and nonsuperconducting $K_{0.8}Fe_{1.8}Co_{0.2}Se_2$ single crystals there are phonon modes originating from metallic/superconducting $I4/mmm$ phase and insulating $I4/m$ phase with ordered Fe vacancies. Temperature analysis of energy and linewidth of the vibrational modes were done using the model which takes into account lattice thermal expansion and anharmonic effects. The modes originating from the $I4/m$ phase are well described by that model. On the other hand, A_{1g} mode energy in the superconducting sample exhibits sudden jump, which was ascribed to the change in the electronic structure when entering the superconducting state. By investigating Raman spectra of $K_xFe_{2-y}Se_2$ single crystals doped with various Co concentrations, the evolution of phase separation was followed. With increasing cobalt content phonon modes from the $I4/m$ phase disappear and in Raman spectra remain only two phonon modes originating from the high symmetry $I4/mmm$ phase. Broad asymmetric structure in the samples with intermediate Co concentrations was interpreted as a fingerprint of strong crystalline disorder. The presence of only two phonon modes in the end member of this sequence - $K_xCo_{2-y}Se_2$ - excludes the possibility of ordered vacancies. Measured Raman spectra show that ferromagnetic phase transition around 74 K in this single crystal has significant impact on phonon mode behavior. Namely, above the ferromagnetic transition, temperature dependence of phonon energy and linewidth looks conventional. On the other hand, below critical temperature both modes exhibit sudden hardening, A_{1g} mode narrows and B_{1g} one significantly broadens, which is ascribed to the spin-phonon and electron-phonon interaction. Large linewidth of the Raman modes originates from the electron-phonon coupling enhanced by the crystal disorder and spin fluctuation effects.

MATERIALS RESEARCH SOCIETY OF SERBIA
INSTITUTE OF TECHNICAL SCIENCES OF SASA

Programme and the Book of Abstracts

EIGHTEENTH YOUNG RESEARCHERS' CONFERENCE

MATERIALS SCIENCE AND ENGINEERING

Belgrade, December 4–6, 2019

http://www.mrs-serbia.org.rs/index.php/young-researchers-conference

Aim of the Conference

Main aim of the conference is to enable young researchers (post-graduate, master or doctoral student, or a PhD holder younger than 35) working in the field of materials science and engineering, to meet their colleagues and exchange experiences about their research.

Topics

Biomaterials
Environmental science
Materials for high-technology applications
Materials for new generation solar cells
Nanostructured materials
New synthesis and processing methods
Theoretical modelling of materials

Scientific and Organizing Committee

Committee President
Smilja Marković   Institute of Technical Sciences of SASA, Belgrade, Serbia

Vice-presidents
Dragana Jugović   Institute of Technical Sciences of SASA, Belgrade, Serbia
Magdalena Stevanović   Institute of Technical Sciences of SASA, Belgrade, Serbia
Đorđe Veljović   Faculty of Technology and Metallurgy, Belgrade, Serbia

Members
Nadica Abazović   Institute of Nuclear Sciences "Vinča", Belgrade, Serbia
Jasmina Dostanić   Institute of Chemistry, Technology and Metallurgy, Belgrade, Serbia
Branka Hadžić   Institute of Physics, Belgrade, Serbia
Ivana Jevremović   Norwegian University of Science and Technology, Trondheim, Norway
Sonja Jovanović   Institute of Nuclear Sciences "Vinča", Belgrade, Serbia; Institute Jožef Stefan, Ljubljana, Slovenia
Ralph Kraehnert   Technical University of Berlin, Germany
Snežana Lazić   Universidad Autónoma de Madrid, Spain
Miodrag Lukić   Institute of Technical Sciences of SASA, Belgrade, Serbia
Lidija Mančić   Institute of Technical Sciences of SASA, Belgrade, Serbia
Marija Milanović   Faculty of Technology, Novi Sad, Serbia
Nebojša Mitrović   Faculty of Technical Sciences, Čačak, Serbia
Irena Nikolić   Faculty of Metallurgy and Technology, Podgorica, Montenegro
Marko Opačić   Institute of Physics, Belgrade, Serbia
Rafał Poręba   Institute of Macromolecular Chemistry AS CR, v.v.i., Prague 6, Czech Republic
Vuk Radmilović   Faculty of Technology and Metallurgy, Belgrade, Serbia
Srečo Škapin   Institute Jožef Stefan, Ljubljana, Slovenia
Boban Stojanović   Faculty of Sciences, Kragujevac, Serbia

Ivana Stojković-Simatović   Faculty of Physical Chemistry, Belgrade, Serbia
Vuk Uskoković   University of California, Irvine, USA
Rastko Vasilić   Faculty of Physics, Belgrade, Serbia
Siniša Vučenović   Faculty of Sciences, Department of Physics, Banja Luka, B&H
Marija Vukomanović   Institute Jožef Stefan, Ljubljana, Slovenia

Conference Secretary
Aleksandra Stojičić   Institute of Technical Sciences of SASA, Belgrade, Serbia

Conference Technical Committee

Milica Ševkušić, Miloš Milović, Ivana Dinić, Marina Vuković, Vladimir Rajić, Željko Mravik, Vukašin Ugrinović

Results of the Conference

Beside printed «Program and the Book of Abstracts», which is disseminated to all conference participants, selected and awarded peer-reviewed papers will be published in journal "Tehnika – Novi Materijali". The best presented papers, suggested by Session Chairpersons and selected by Awards Committee, will be proclaimed at the Closing Ceremony. Part of the award is free-of-charge conference fee at YUCOMAT 2020.

Sponsors

Acknowledgement

10-6

Spin-phonon coupling in $CrSiTe_3$ and $CrSi_{0.8}Ge_{0.1}Te_3$

Ana Milosavljević[1], A. Šolajić[1], J. Pešić[1], B. Višić[1], M. Opačić[1],
Yu Liu[2], C. Petrovic[2], N. Lazarević[1], Z. V. Popović[1,3]

[1]*Center for Solid State Physics and New Materials, Institute of Physics Belgrade, University of Belgrade, Pregrevica 118, 11080 Belgrade, Serbia,* [2]*Condensed Matter Physics and Materials Science Department, Brookhaven National Laboratory, Upton, NY 11973-5000, USA,* [3]*Serbian Academy of Sciences and Arts, Knez Mihailova 35, 11000 Belgrade, Serbia*

Trichalcogenides $CrXTe_3$ (X = Si, Ge) are semiconducting representatives of the van der Waals materials, with ferromagnetic order and band gap of 0.4 eV for Si and 0.7 eV for Ge compound, and Curie temperatures of 32 K and 61 K, respectively. Their layered structure provided exfoliation to mono and few-layer nanosheets, due to the weak van der Waals interlayer bonding. This possibility togeather with their semiconducting and magnetic properties makes them ideal candidates for applications in optoelectronics and nano-spintronics.

Here we present temperature dependent Raman scattering study on $CrSiTe_3$ and $CrSi_{0.8}Ge_{0.1}Te_3$. Four and eight out of ten Raman active modes were assigned and observed for pure and slightly doped compound, respectively. The self-energies of $A_g^?$ and E_g^3 symmetry modes of $CrSiTe_3$ compound exhibit unconventional temperature evolution around 180 K. In addition, doubly degenerate E_g^3 mode shows a clear change of asymmetry in the same temperature region. The observed behavior is consistent with the previously reported presence of short-range magnetic order and strong spin-phonon coupling. Changing the concentrations of elements in parent compounds and doping plays a significant role in semiconducting physics and can lead to surprising physical properties, like considerable change in magnetic transition temperature or structural modifications. SEM measurements performed on our CrSi0.8Ge0.1Te3 single crystals revealed the 10% concentration of Ge atoms and the same amount of vacancies. Inelastic scattering results on CrSi0.8Ge0.1Te3 in addition to symmetry predicted modes, shows the presence of one mode attributed to the inhomogeneous distribution of Ge atoms, and two overtones, all obeying pure A_g selection rules. All analyzed modes display unconventional behavior, but in a difference from the pure compound on a higher temperature of 210 K.

INSTITUTE OF TECHNICAL SCIENCES OF SASA
MATERIALS RESEARCH SOCIETY OF SERBIA

Programme and the Book of Abstracts

TWENTIETH YOUNG RESEARCHERS' CONFERENCE
MATERIALS SCIENCE AND ENGINEERING

Belgrade, November 30 – December 2, 2022

Aim of the Conference

Main aim of the conference is to enable young researchers (post-graduate, master or doctoral student, or a PhD holder younger than 35) working in the field of materials science and engineering, to meet their colleagues and exchange experiences about their research.

Topics

Biomaterials
Environmental science
Materials for high-technology applications
Materials for new generation solar cells
Nanostructured materials
New synthesis and processing methods
Theoretical modelling of materials

Scientific and Organizing Committee

Committee President
Smilja Marković   Institute of Technical Sciences of SASA, Belgrade, Serbia

Vice-presidents
Dragana Jugović   Institute of Technical Sciences of SASA, Belgrade, Serbia
Magdalena Stevanović   Institute of Technical Sciences of SASA, Belgrade, Serbia
Đorđe Veljović   Faculty of Technology and Metallurgy, Belgrade, Serbia

Members
Tatiana Demina   Enikolopov Institute of Synthetic Polymeric Materials,
                                    Russian Academy of Sciences
Jasmina Dostanić   Institute of Chemistry, Technology and Metallurgy, Belgrade,
                                    Serbia
Xuesen Du   Chongqing University, Chongqing, China
Branka Hadžić   Institute of Physics, Belgrade, Serbia
Ivana Jevremović   Norwegian University of Science and Technology, Trondheim,
                                    Norway
Sonja Jovanović   Institute of Nuclear Sciences "Vinča", Belgrade, Serbia
Snežana Lazić   Universidad Autónoma de Madrid, Spain
Lidija Mančić   Institute of Technical Sciences of SASA, Belgrade, Serbia
Marija Milanović   Faculty of Technology, Novi Sad, Serbia
Miloš Milović   Institute of Technical Sciences of SASA, Belgrade, Serbia
Nebojša Mitrović   Faculty of Technical Sciences, Čačak, Serbia
Irena Nikolić   Faculty of Metallurgy and Technology, Podgorica, Montenegro
Marko Opačić   Institute of Physics, Belgrade, Serbia
Vuk Radmilović   Faculty of Technology and Metallurgy, Belgrade, Serbia
Tatjana D. Savić   Institute of Nuclear Sciences "Vinča", Belgrade, Serbia
Ana Stanković   Institute of Technical Sciences of SASA, Belgrade, Serbia
Srečo Škapin   Institute Jožef Stefan, Ljubljana, Slovenia
Boban Stojanović   Faculty of Sciences, Kragujevac, Serbia

Ivana Stojković-Simatović	Faculty of Physical Chemistry, Belgrade, Serbia
Konrad Terpiłowski	Department of Interfacial Phenomena, Institute of Chemical Sciences, Faculty of Chemistry, Maria Curie-Skłodowska University in Lublin, Poland
Vuk Uskoković	TardigradeNano, Irvine, CA, USA
Rastko Vasilić	Faculty of Physics, Belgrade, Serbia
Ljiljana Veselinović	Institute of Technical Sciences of SASA, Belgrade, Serbia
Siniša Vučenović	Faculty of Sciences, Department of Physics, Banja Luka, B&H
Marija Vukomanović	Institute Jožef Stefan, Ljubljana, Slovenia

Conference Secretary

Ivana Dinić   Institute of Technical Sciences of SASA, Belgrade, Serbia

Conference Technical Committee

Aleksandra Stojičić, Marina Vuković, Željko Mravik, Katarina Aleksić, Jelena Rmuš

Results of the Conference

Beside printed «Programme and the Book of Abstracts», which is disseminated to all conference participants, selected and awarded peer-reviewed papers will be published in journal "Tehnika – Novi Materijali". The best presented papers, suggested by Session Chairpersons and selected by Awards Committee, will be proclaimed at the Closing Ceremony. Part of the award is free-of-charge conference fee at YUCOMAT 2023.

Sponsors

Acknowledgement

6-7

Effect of disorder and electron-phonon interaction on 2*H*-TaSe$_{2-x}$S$_x$ lattice dynamics probed by Raman spectroscopy

Jovan Blagojević[1], Sanja Đurđić Mijin[1], Jonas Bekaert[2], Milorad Milošević[2], Čedomir Petrović[3], Yu Liu[3], Marko Opačić[1], Zoran Popović[1, 4] and Nenad Lazarević[1]

[1]*Institute of Physics, University of Belgrade, Pregrevica 118, 11080 Belgrade, Serbia,* [2]*Department of Physics & NANOlab Center of Excellence, University of Antwerp, Groenenborgerlaan 171, B-2020 Antwerp, Belgium,* [3]*Condensed Matter Physics and Materials Science Department, Brookhaven National Laboratory, Upton, NY 11973-5000, USA,* [4]*Serbian Academy of Sciences and Arts, Knez Mihailova 35, 11000 Belgrade, Serbia*

Transitional metal dichalcogenides have attracted a lot of attention due to their rich phase diagrams, thickness-dependent transport, distinctive optical characteristics, and the emergence of collective electron phenomena (e. g. charge density waves - CDW and superconductivity) which can co-exist, contrary to what was predicted by previous theoretical studies. Given that both superconductivity and CDW phase have been experimentally confirmed in the crystal alloys of 2*H*-TaSe$_{2-x}$S$_x$, these materials represent perfect candidates to investigate an intricate connection between these two phenomena. Additionally, it was recently shown that in the metallic single crystal alloys of 2*H*-TaSe$_{2-x}$S$_x$ the crystalline disorder favours superconductivity while suppressing CDW phase. In this study, Raman spectroscopy was used to investigate the lattice dynamics of 2*H*-TaSe$_{2-x}$S$_x$ (0 ≤ x ≤ 2) alloys. Experimental results were compared to density functional theory (DFT) and density functional perturbation theory (DFPT) calculations. In the Raman spectra of pristine samples two out of three symmetry predicted Raman active modes were observed, with the missing mode being unobservable in the used backscattering geometry. Experimental values of phonon energies are in good agreement with theoretical calculations. The temperature dependence of phonon energies and line widths directly reflects existing CDW transitions. The Raman spectra of doped materials were compared to those of pure samples in order to inspect how the electron-phonon interaction and crystallographic disorder affect the phonons. Additional peaks and a dramatic development of the two-phonon structure are detected in the Raman spectra of the doped samples. A signature of the crystallographic disorder can also be identified in the sulfur content dependence of phonon energies, line widths and Fano parameter.

7-2

Optical properties of nanostructured multi-stoichiometric tungsten suboxides

Bojana Višić[1,2,3], Luka Pirker[1,3], Marko Opačić[2], Ana Milosavljević[2], Nenad Lazarević[2], Boris Majaron[3,4], Maja Remškar[1]

[1]Department of Condensed Matter Physics, Jozef Stefan Institute, Jamova Cesta 39, 1000 Ljubljana, Slovenia, [2]Institute of Physics Belgrade, University of Belgrade, Pregrevica 118, 11080 Belgrade, Serbia, [3]Department of Complex Matter, Jozef Stefan Institute, Jamova 39, 1000 Ljubljana, Slovenia, [4]Faculty of Physics and Mathematics, University of Ljubljana, Jadranska 19, Slovenia

Tungsten suboxide (WO_{3-x}) nanomaterials were synthesized via chemical vapor transport method and the role of their crystal structures on the optical properties was investigated. These materials grow either in the shape of platelets or nanotiles, or as nanowires (W_5O_{14}, $W_{18}O_{49}$). For the first one which represents thin quasi-2D materials, the appearance of defect states gives rise to two indirect absorption edges. One is assigned to the regular bandgap between the valence and the conduction band, while the second is a defect-induced band. While the bandgap values of platelets and nanotiles are in the upper range of the reported values for the suboxides, the nanowires' bandgaps are lower due to the higher number of free charge carriers. Both types of nanowires sustain localized surface plasmon resonances, as evidenced from the extinction measurements, whereas the quasi-2D materials exhibit excitonic transitions. Photoluminescence emission peaks in the UV region were detected for all four materials. The interplay of the crystal structure, oxygen vacancies and shape can result in changes in optical behavior, and the understanding of these effects could enable intentional tuning of selected properties.

9-7

Infrared and Raman study of narrow-gap semiconductor FeGa$_3$

C. Martin[1], V. A. Martinez[2], M. Opačić[3], S. Djurdjić-Mijin[3], P. Mitrić[3], A. Umićević[4], V. N. Ivanovski[4], A. Poudel[1], I. Sydoryk[1], Weijun Ren[5], R. M. Martin[6], D. B. Tanner[2], N. Lazarević[3], C. Petrovic[5], and D. Tanasković[3]

[1]*Ramapo College of New Jersey, Mahvah, NJ 07430, USA,* [2]*Department of Physics, University of Florida, Gainesville, Florida 32611, USA,* [3]*Institute of Physics Belgrade, University of Belgrade, Pregrevica 118, 11080 Belgrade, Serbia,* [4]*Vinca Institute of Nuclear Sciences – National Institute of the Republic of Serbia, University of Belgrade, Belgrade, Serbia,* [5]*Brookhaven National Laboratory, NY 11973, USA,* [6]*Montclair State University, Montclair, NJ 07043, USA*

Narrow-gap semiconductors have been intensively studied in the last few years due to their huge thermoelectric power at low temperatures and possible impact of strong electronic correlations on their physical properties. Here, we analyse infrared and Raman spectra of FeGa$_3$ single crystal. The optical conductivity obtained from reflectance measurements suggests an indirect energy gap of around 0.4 eV, although the existence of substantial spectral weight at low energies prevents its precise determination. The energies of Raman and infrared active modes obtained by our DFT calculations agree very well with the experimental results. Temperature dependence of Raman mode energies and linewidths is weak between 80 and 300 K, indicating the absence of any phase transition. Most of the vibrational modes are very narrow due to weak electron-phonon and/or spin-phonon interactions, and good crystallinity of the single crystal, which is also confirmed by the Mössbauer spectra.

Strained FeSC

Center for Solid
State Physics &
New Materials

IP8
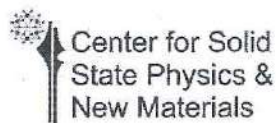
9-10 June 2022, Institute of Physics Belgrade

http://strainedfesc.ipb.ac.rs/workshop-in-strongly-correlated-electron-systems/

WORKSHOP IN STRONGLY CORRELATED ELECTRON SYSTEMS

Special focus of the conference will be devoted to iron chalcogenide superconductors and research performed during StrainedFeSC project.

"Workshop in strongly correlated electron systems" will be held in honor of Academician Zoran V. Popovic.

Science Fund
of the Republic of Serbia

Organization Committee

Dr. Nenad Lazarević, *Institute of Physics Belgrade, University of Belgrade*
Dr. Jelena Pešić, *Institute of Physics Belgrade, University of Belgrade*
Dr. Borislav Vasić, *Institute of Physics Belgrade, University of Belgrade*
Dr. Ana Milosavljević, *Institute of Physics Belgrade, University of Belgrade*
Dr. Sanja Đurđić Mijin, *Institute of Physics Belgrade, University of Belgrade*
MSc Andrijana Šolajić, *Institute of Physics Belgrade, University of Belgrade*

SUPPORTED BY

Influence of magnetism and electron-phonon interaction on lattice dynamics of pure and Co-doped $K_xFe_{2-y}Se_2$ single crystals

M. Opačić[1], N. Lazarević[1], D. Tanasković[1], M. Šćepanović[1], C. Petrovic[2] and Z. V. Popović[1,3]

[1]Institute of Physics Belgrade, University of Belgrade, Pregrevica 118, 11080 Belgrade, Serbia
[2]Department of Condensed Matter Physics and Materials Science, Brookhaven National Laboratory, Upton, New York 11973, USA
[3]Serbian Academy of Sciences and Arts, Knez Mihailova 35, 11000 Belgrade, Serbia

In this work, we aimed to determine the effects electronic and magnetic degrees of freedom have on vibrational properties of pure and cobalt-doped $K_xFe_{2-y}Se_2$ single crystals. Vibrational properties were investigated using Raman spectroscopy, with the help of density functional theory (DFT) calculations. Phonon spectra of superconducting $K_xFe_{2-y}Se_2$ and nonsuperconducting $K_{0.8}Fe_{1.8}Co_{0.2}Se_2$ crystals reveal Raman modes originating from metallic/superconducting *I4/mmm* phase and Fe vacancy-ordered, insulating *I4/m* phase. Temperature dependence of energy and linewidth of phonons from the insulating phase can be well described by taking into account lattice thermal expansion and anharmonicity. However, energy of the A_{1g} mode, originating from the *I4/mmm* phase, exhibits sudden hardening in the superconducting sample around critical temperature, suggesting the change of the electronic structure. By doping $K_xFe_{2-y}Se_2$ with cobalt, Raman modes from the insulating phase gradually disappear, and broad asymmetric structure become observable, probably originating from strong crystalline disorder. Raman spectra of $K_xCo_{2-y}Se_2$ single crystal host only two modes, excluding the possibility of ordered vacancies, unlike its Fe-counterpart. Ferromagnetic phase transition leaves clear fingerprint on temperature dependence of phonon energies and linewidths.

BPU11 CONGRESS
The Book of Abstracts
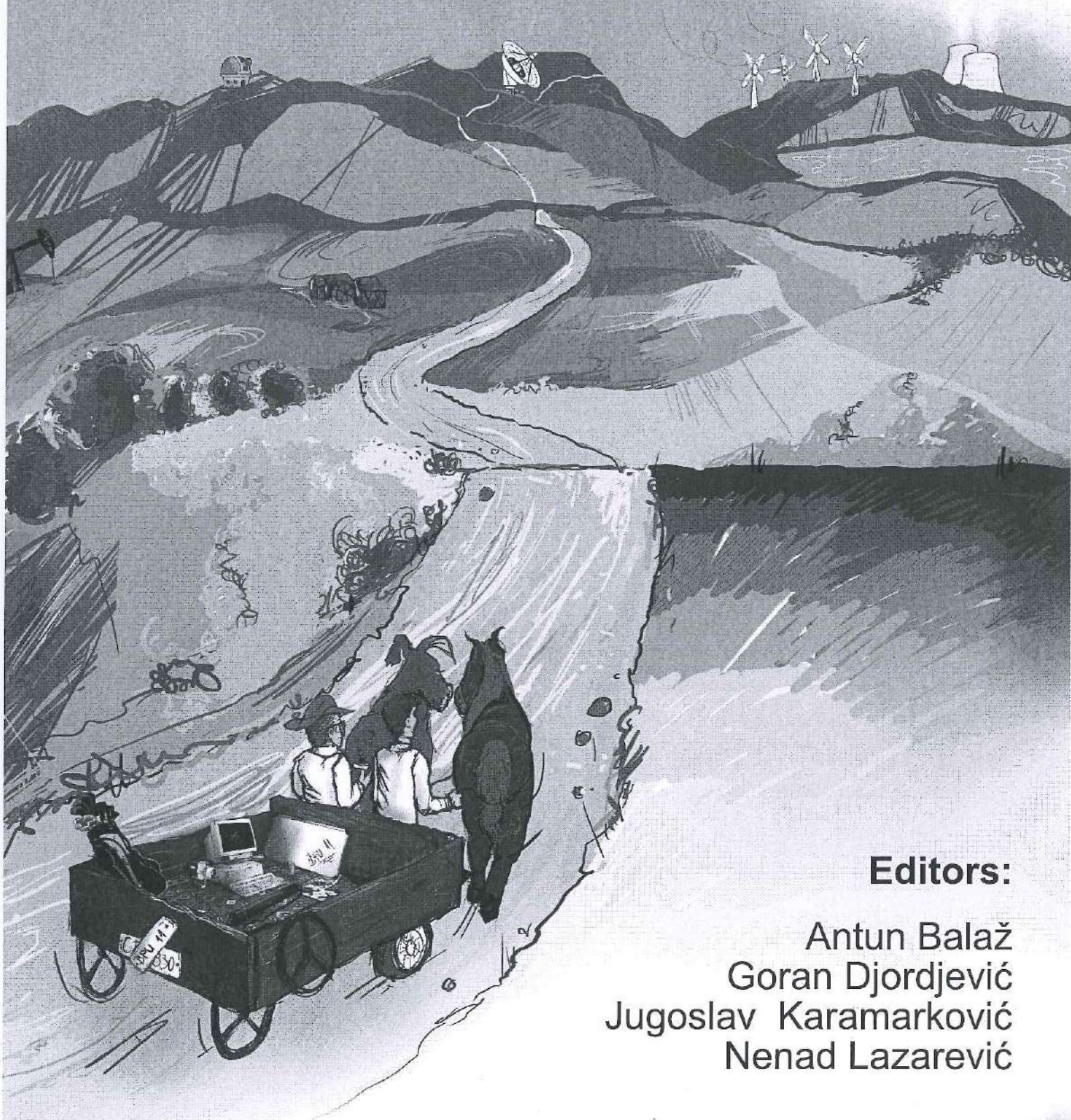
Editors:

Antun Balaž
Goran Djordjević
Jugoslav Karamarković
Nenad Lazarević

Belgrade, 2022

BPU11 CONGRESS

28 August 2022 - 1 September 2022

Book of Abstracts

Editors: Antun Balaž, Goran Djordjević,
Jugoslav Karamarković, Nenad Lazarević

Belgrade, 2022

S06-CMPSP-112 / Oral presentation

Effects of structural disorder on phonon spectra of $2H$-TaSe$_{2-x}$S$_x$ $(0 \le x \le 2)$ single crystals

Authors: Jovan Blagojević[1]; Sanja Djurdjic Mijin[2]; Jonas Bekaert[3]; Yu Liu[4]; Marko Opačić[2]; Milorad V. Milošević[3]; Cedomir Petrovic[4]; Nenad Lazarević[2]

[1] *Faculty of Physics, University of Belgrade, Studentski trg 12, 11001 Belgrade, Serbia & Institute of Physics Belgrade, University of Belgrade, Pregrevica 118, 11080 Belgrade, Serbia*

[2] *Institute of Physics Belgrade, University of Belgrade, Pregrevica 118, 11080 Belgrade, Serbia*

[3] *Department of Physics, University of Antwerp, Groenenborgerlaan 171, B-2020 Antwerp, Belgium*

[4] *Department of Condensed Matter Physics and Materials Science, Brookhaven National Laboratory, Upton, New York 11973, USA*

Presenter: M. Opačić (marko.opacic@ipb.ac.rs)

Transition metal dichalcogenides, as a well studied family of quasi-2D materials, have attracted considerable attention in recent years due to rich phase diagrams, thickness-dependent transport, unique optical properties and collective electron phenomena which occur at experimentally accessible temperatures. Additionally, it was recently shown that in the metallic single crystal alloys of $2H$-TaSe$_{2-x}$S$_x$ the crystalline disorder promotes superconductivity, while suppressing charge density wave (CDW) order. In this work, the lattice dynamics of TaSe$_{2-x}$S$_x$ $(0 \le x \le 2)$ alloys was probed using Raman spectroscopy and results were compared to density functional theory (DFT) calculations. In order to investigate whether crystallographic disorder affects the phonons, spectra of doped materials were compared to the ones belonging to the end alloys. The Raman spectra of the end compounds ($x = 0$ and $x = 2$) host two out of three symmetry-expected Raman active modes for backscattering configuration. Calculated phonon energies agree well with the experimental ones. In Raman spectra of the doped samples additional peaks, though of low intensity, can be easily identified. These additional peaks most likely arise from the crystalline disorder. Dependence of phonon energies and linewidths on sulfur content x also reveals a clear fingerprint of crystallographic disorder.

S06-CMPSP-113 / Oral presentation

DFT study of AlF3 intercalated in HOPG: a rechargeable battery application

Authors: Sindy Julieth Rodriguez Sotelo[1]; Adriana E. Candia[2]; Mario C.G. Passeggi (Jr.)[1]; Gustavo Ruano[3]

[1] *Laboratorio de Física de Superficies e Interfaces, Instituto de Física del Litoral (CONICET-UNL) & Departamento de Física, Facultad de Ingeniería Química (UNL)*

[2] *Laboratorio de Física de Superficies e Interfaces, Instituto de Física del Litoral (IFIS-CONICET-UNL)*

- Blerina Papajani (Elbasan, Albania)
- Alexander Petrov (Sofia, Bulgaria)
- Zoran Petrović (Belgrade, Serbia)
- Stevan Pilipović (Novi Sad, Serbia), TBC
- Stefan Pokorski (Warsaw, Poland)
- Zoran Popović (Belgrade, Serbia), co-chair
- Zoran Radović (Belgrade, Serbia)
- Petra Rudolf (Groningen, Netherlands / EPS)
- Miljko Satarić (Belgrade, Serbia)
- Dejan Stojković (Buffalo, NY, USA)
- Đorđe Šijački (Belgrade, Serbia), TBC
- Milan Tadić (Belgrade, Serbia)
- Efstratios Theodossiou (Athens, Greece)
- Ion Tiginyanu (Chişinău, Moldova)
- Viktor Urumov (Skopje, North Macedonia)
- Evgeniya Valcheva (Sofia, Bulgaria)
- Mihai Visinescu (Bucharest, Romania)
- Gerti Xhixha (Tirana, Albania)
- Oliver Zajkov (Skopje, North Macedonia)
- Christos Zerefos (Athens, Greece)

International Scientific Committee

- Antun Balaž (Belgrade, Serbia), co-chair
- Jugoslav Karamarković (Niš, Serbia), co-chair
- Nenad Lazarević (Belgrade, Serbia), co-chair

1. **Nuclear Physics and Nuclear Energy**
   - Daniel Andreica (Cluj-Napoca, Romania)
   - Burcu Cakirli Mutlu (Istanbul, Turkey)
   - Igor Čeliković (Belgrade, Serbia), coordinator
   - Dimitrije Maletić (Belgrade, Serbia), secretary
   - Georgi Raynovski (Sofia, Bulgaria)
   - Svetislav Savović (Kragujevac, Serbia)
   - Erjon Spahiu (Tirana, Albania)
2. **Astronomy and Astrophysics**
   - Vesna Borka (Belgrade, Serbia)
   - Gojko Đurašević (Belgrade, Serbia)
   - Mimoza Hafizi (Tirana, Albania)
   - Gordana Jovanović (Podgorica, Montenegro)
   - Milan Milošević (Niš, Serbia)
   - Jelena Petrović (Belgrade, Serbia)
   - Marius Piso (Bucharest, Romania)
   - Luka Popović (Belgrade, Serbia), coordinator

- Evgeni Semkov (Sofia, Bulgaria)
- Saša Simić (Kragujevac, Serbia)
- Nikolaos Spyrou (Thessaloniki, Greece)
- Vladimir Srećković (Belgrade, Serbia), coordinator
- Dejan Urošević (Belgrade, Serbia)

3. **Gravitation and Cosmology**
- Duško Borka (Belgrade, Serbia)
- Dragoljub Dimitrijević (Niš, Serbia), secretary
- Mimoza Hafizi (Tirana, Albania)
- Predrag Jovanović (Belgrade, Serbia)
- Kostas Kleidis (Thessaloniki, Greece)
- Voja Radovanović (Belgrade, Serbia)
- Zoran Rakić (Belgrade, Serbia)
- Marko Vojinović (Belgrade, Serbia), coordinator
- Dumitru Vulcanov (Timisoara, Romania)
- Stoycho Yazadzhiev (Sofia, Bulgaria)

4. **Atomic and Molecular Physics**
- Tasko Grozdanov (Belgrade, Serbia)
- Lucian Ion (Bucharest, Romania)
- Slavoljub Mijović (Podgorica, Montenegro)
- Nenad Milojević (Niš, Serbia), secretary
- Asen Pashov (Sofia, Bulgaria)
- Violeta Petrović (Kragujevac, Serbia), coordinator
- Igor Savić (Novi Sad, Serbia), coordinator
- Nenad Simonović (Belgrade, Serbia)

5. **High Energy Physics (Particles and Fields)**
- Tatjana Agatonović Jovin (Belgrade, Serbia)
- Calin Alexa (Bucharest, Romania)
- Biljana Antunović (Banja Luka, Bosnia and Herzcegovina)
- Ion Cotaescu (Timisoara, Romania)
- Dragoljub Dimitrijević (Niš, Serbia), secretary
- Magdalena Đorđević (Belgrade, Serbia)
- Miloš Đorđević (Belgrade, Serbia)
- Plamen Iaydjiev (Sofia, Bulgaria)
- Predrag Milenović (Belgrade, Serbia), coordinator
- Rudina Osmanaj (Tirana, Albania)
- Fotios Ptochos (Nicosia, Cyprus)
- Voja Radovanović (Belgrade, Serbia)
- Nataša Raičević (Podgorica, Montenegro)
- Ömer Yavas (Ankara, Turkey)
- Lidija Živković (Belgrade, Serbia), coordinator

6. **Condensed Matter Physics and Statistical Physics**
- Miroslav Abrashev (Sofia, Bulgaria)
- Antun Balaž (Belgrade, Serbia)
- Jelena Belošević-Čavor (Belgrade, Serbia), coordinator
- Željka Cvejić (Novi Sad, Serbia), coordinator

- Zorana Dohčević-Mitrović (Belgrade, Serbia)
- Sinasi Ellialtioglu (Ankara, Turkey)
- Cristian Enachescu (Iasi, Romania)
- Oguz Gulseren (Ankara, Turkey)
- Sanja Janićević (Kragujevac, Serbia)
- Nataša Jović Orsini (Belgrade, Serbia)
- Nenad Lazarević (Belgrade, Serbia)
- Panos Patsalas (Thessaloniki, Greece)
- Dušan Popović (Belgrade, Serbia)
- Vadim Sirkeli (Chişinău, Moldova)
- Nicolaos Toumbas (Nicosia, Cyprus)
- Daniel Vizman (Timisoara, Romania)
- George Vourlias (Thessaloniki, Greece)
- Nenad Vukmirović (Belgrade, Serbia), coordinator
- Tatjana Vuković (Belgrade, Serbia)

7. **Optics and Photonics**
- Petar Atanasov (Sofia, Bulgaria)
- Tudor Braniste (Chişinău, Moldova)
- Maria Dinescu (Bucharest, Romania)
- Nikola Filipović (Niš, Serbia)
- Milan Kovačević (Kragujevac, Serbia)
- Ana Mančić (Niš, Serbia)
- Peđa Mihailović (Belgrade, Serbia), secretary
- Stanko Nikolić (Belgrade, Serbia)
- Vladan Pavlović (Niš, Serbia)
- Marica Popović (Belgrade, Serbia)
- Svetislav Savović (Kragujevac, Serbia)
- Milutin Stepić (Belgrade, Serbia), coordinator
- Rodica Vladoiu (Constanta, Romania)

8. **Plasma and Gas-Discharge Physics**
- Gheorghe Dinescu (Bucharest, Romania)
- Saša Dujko (Belgrade, Serbia), coordinator
- Saša Gocić (Niš, Serbia)
- Zhivko Kissovski (Sofia, Bulgaria)
- Milan Kovačević (Kragujevac, Serbia)
- Bratislav Obradović (Belgrade, Serbia), coordinator
- Mara Šćepanović (Podgorica, Montenegro)

9. **Theoretical, Mathematical and Computational Physics**
- Metin Arık (Istanbul, Turkey)
- Miroljub Dugić (Kragujevac, Serbia)
- Igor Franović (Belgrade, Serbia), coordinator
- Borislav Gajić (Belgrade, Serbia), secretary
- Aurelian Isar (Bucharest, Romania)
- Milan Milošević (Niš, Serbia)
- Klaudio Peqini (Tirana, Albania)
- Slobodan Radošević (Novi Sad, Serbia)

- Radoslav Rashkov (Sofia, Bulgaria)
- Neli Stoilova (Sofia, Bulgaria)

10. **Meteorology and Geophysics**
   - Ekaterina Bachvarova (Sofia, Bulgaria)
   - Vladimir Đurđević (Belgrade, Serbia), coordinator
   - Kostadin Ganev (Sofia, Bulgaria)
   - Slobodan Ničković (Belgrade, Serbia), secretary
   - Klaudio Peqini (Tirana, Albania)
   - Tanja Porja (Tirana, Albania)
   - Sabina Stefan (Bucharest, Romania)

11. **Environmental Physics – Alternative Sources of Energy**
   - Balis Dimitrios (Thessaloniki, Greece)
   - Valentin Ivanovski (Belgrade, Serbia)
   - Zoran Mijić (Belgrade, Serbia), coordinator
   - Ioan Stamatin (Bucharest, Romania)
   - Ana Umićević (Belgrade, Serbia), secretary
   - Petko Vitanov (Sofia, Bulgaria)
   - Gerti Xhixha (Tirana, Albania)

12. **Physics of Socioeconomic Systems and Applied Physics**
   - Olta Çakaj (Tirana, Albania)
   - Dragana Krstić (Kragujevac, Serbia)
   - Mihail Lungu (Timisoara, Romania)
   - Vladimir Marković (Kragujevac, Serbia), secretary
   - Marija Mitrović Dankulov (Belgrade, Serbia), coordinator
   - Petar Petrov (Sofia, Bulgaria)
   - Dode Prenga (Tirana, Albania)
   - Stavros Stavrinides (Thessaloniki, Greece)

13. **Biophysics and Medical Physics**
   - Aleksandar Krmpot (Belgrade, Serbia), coordinator
   - Dragana Krstić (Kragujevac, Serbia), secretary
   - Mihai Radu (Bucharest, Romania)
   - Miloš Vićić (Belgrade, Serbia)
   - Victoria Vitkova (Sofia, Bulgaria)
   - Gerti Xhixha (Tirana, Albania)
   - Emil Xhuvani (Tirana, Albania)

14. **Physics Education, History and Philosophy of Physics**
   - Dejan Đokić (Belgrade, Serbia), secretary
   - Maya Gaydarova (Sofia, Bulgaria)
   - Ivan Lalov (Sofia, Bulgaria)
   - Dragana Malivuk Gak (Banja Luka, Bosnia and Herzcegovina)
   - Silvana Mico (Tirana, Albania)
   - Violeta Petrović (Kragujevac, Serbia), coordinator
   - Sebastian Popescu (Iasi, Romania)
   - Stavros Stavrinides (Thessaloniki, Greece)
   - Maja Stojanović (Novi Sad, Serbia)
   - Mira Vučeljić (Podgorica, Montenegro)
   - Andrijana Žekić (Belgrade, Serbia)

15. **Metrology and Instrumentation**
  - Luljeta Gjeçi (Tirana, Albania)
  - Aleksandar Kandić (Belgrade, Serbia)
  - Marina Lekić (Belgrade, Serbia), coordinator
  - Aurelian Luca (Bucharest, Romania)
  - Ivan Stefanov (Sofia, Bulgaria)
  - Stevan Stojadinović (Belgrade, Serbia), secretary

International Organizing Committee

  - Baki Akkuş (Istanbul, Turkey)
  - Lambe Barandovski (Skopje, North Macedonia)
  - Ivan Belča (Belgrade, Serbia)
  - Luc Berge (DAM Arpjaon, France/ EPS P), co-chair
  - Aleksandar Bogojević (Belgrade, Serbia)
  - Radu Constantinescu (Craiova, Romania)
  - Dragoljub Dimitrijević (Niš, Serbia)
  - Marija Dimitrijević Ćirić (Belgrade, Serbia)
  - Goran Djordjević (Niš, Serbia), co-chair
  - Polikron Dhoqina (Tirana, Albania)
  - Danica Dobrosavljevic (Niš, Serbia)
  - Nikola Filipović (Niš, Serbia)
  - Ertan Güdekli (Istanbul, Turkey)
  - Valentin Ivanovski (Belgrade, Serbia)
  - Jasmina Jeknić Dugić (Niš, Serbia)
  - Božidar Jovanović (Belgrade, Serbia)
  - Nikola Konjik (Belgrade, Serbia)
  - Milan Kovačević (Kragujevac, Serbia)
  - Nenad Lazarević (Belgrade, Serbia)
  - David Lee (Mulhouse, France / EPS GS)
  - Vladimir Marković (Kragujevac, Serbia)
  - Milan Milošević (Niš, Serbia)
  - Peđa Mihailović (Belgrade, Serbia), TBC
  - Predrag Miranović (Podgorica, Montenegro)
  - Dušan Mrđa (Novi Sad, Serbia)
  - Zoran Ognjanović (Belgrade, Serbia)
  - Şener Oktik (Istanbul, Turkey)
  - Snežana Pajović (Belgrade, Serbia)
  - Milica Pavkov Hrvojević (Novi Sad, Serbia)
  - Alexander Petrov (Sofia, Bulgaria)
  - Goran Poparić (Belgrade, Serbia)
  - Zoran Rakić (Belgrade, Serbia)
  - Goran Ristić (Niš, Serbia)
  - Nenad Stevanović (Kragujevac, Serbia)

- Marko Stojanović (Niš, Serbia)
- Gülfem Süsoy Dogan (Istanbul, Turkey)
- Blanka Škipina (Banja Luka, Bosnia and Herzcegovina)
- Pavel Topala (Balti, Moldova)
- Dejan Urošević (Belgrade, Serbia)
- Kleideri Vivian (, Greece)
- Kostas Vourlias (Thessaloniki, Greece)
- Siniša Vučenović (Banja Luka, Bosnia and Herzcegovina)
- Hatice Yılmaz Alan (Ankara, Turkey)

Local Organizing Committee

- Jelena Aleksić (Niš)
- Katarina Bito (Niš)
- Marjan Ćirković (Belgrade)
- Dragoljub Dimitrijević (Niš), chair
- Marija Dimitrijević Ćirić (Belgrade)
- Goran Djordjević (Niš)
- Danica Dobrosavljević (Niš)
- Nikola Konjik (Belgrade)
- Irida Lazić (Belgrade)
- Milan Milošević (Niš)
- Stevan Pecić (Belgrade)
- Milica Perić (Niš)
- Anja Petrović (Niš)
- Irena Savić (Belgrade)
- Milena Simić (Niš)
- Jovana Stanimirović (Niš)
- Marko Stojanović (Niš)
- Milica Tošić (Belgrade)

Country Coordinators

- Polikron Dhoqina (Albania)
- Ekaterina Bachvarova (Bulgaria)
- Demetrios Philippou (Cyprus)
- Kostas Vourlias (Greece)
- Pavel Topala (Moldova)
- Predrag Miranović (Montenegro)
- Lambe Barandovski (North Macedonia)
- Mitica Dragusin (Romania)
- Ayşegül Ertoprak (Turkey)

SCMP

26 - 30 June 2023
Belgrade, Serbia

21. СИМПОЗИЈУМ ФИЗИКЕ КОНДЕНЗОВАНЕ МАТЕРИЈЕ
THE 21st SYMPOSIUM ON CONDENSED MATTER PHYSICS

BOOK OF ABSTRACTS

IPB

Institute of Physics Belgrade

Vinca Institute of Nuclear Sciences

University of Belgrade, Faculty of Physics

Serbian Academy of Sciences and Arts

Ministry of Science, Technological Development and Innovation

Conference Chairs

Vladimir Dobrosavljević, *Florida State University, USA*

Zorica Konstantinović, *Institute of Physics Belgrade*

Željko Šljivančanin, *Vinča Institute of Nuclear Sciences*

Organizing Committee

Jelena Pešić, *Institute of Physics Belgrade*- chair

Andrijana Šolajić, *Institute of Physics Belgrade*

Ivana Milošević, *Institute of Physics Belgrade*

Tijana Tomašević-Ilić, *Institute of Physics Belgrade*

Jelena Mitrić, *Institute of Physics Belgrade*

Bojana Višić, *Institute of Physics Belgrade*

Jovan Blagojević, *Institute of Physics Belgrade*

Marko Orozović, *Vinča Institute of Nuclear Sciences*

Mitra Stepić, *Vinča Institute of Nuclear Sciences*

Igor Popov, *Institute for Multidisciplinary Research, Belgrade*

Program Committee

Ivan Božović, *Brookhaven National Laboratory, USA*

Vladimir Dobrosavljević, *Florida State University, USA*

Milan Damnjanović, *Faculty of Physics, University of Belgrade, Serbia*

Vladimir Djoković, *Vinča Institute, University of Belgrade, Serbia*

Gyula Eres, *Oak Ridge National Laboratory, USA*

Laszló Forró, *University of Notre Dame, USA*

Radoš Gajić, *Institute of Physics Belgrade*

Igor Herbut, *Simon Fraser University, Canada*

Zoran Ikonić, *University of Leeds, UK*

Nenad Lazarević, *Institute of Physics Belgrade*

Ivanka Milošević, *Faculty of Physics, University of Belgrade, Serbia*

Milorad Milošević, *University of Antwerp, Belgium*

Milica Milovanović, *Institute of Physics Belgrade*

Stevan Nadj-Perge, *CALTECH, USA*

Branislav Nikolić, *University of Delaware, USA*

Cedomir Petrovic, *Brookhaven National Laboratory, USA*

Dragana Popović, *National High Magnetic Field Laboratory, USA*

Zoran V. Popović, *Institute of Physics Belgrade*

Zoran Radović, *Faculty of Physics, University of Belgrade, Serbia*

Miljko Satarić, *Faculty of Technical Sciences, University of Novi Sad, Serbia*

Marko Spasenović, *Institute of Chemistry, Technology and Metallurgy, Belgrade, Serbia*

Djordje Spasojević, *Faculty of Physics, University of Belgrade, Serbia*

Željko Šljivančanin, *Vinča Institute of Nuclear Sciences*

Bosiljka Tadić, *Jožef Štefan Institute, Slovenia*

Milan Tadić, *School of Electrical Engineering, University of Belgrade, Serbia*

Darko Tanasković, *Institute of Physics Belgrade*

Jasmina Tekić, *Vinča Institute of Nuclear Sciences*

Effect of disorder and electron-phonon interaction on $2H$-TaSe$_{2-x}$S$_x$ lattice dynamics

Jovan Blagojević[1], Sanja Đurđić Mijin[1], Ana Milosavljević[1], Marko Opačić[1], Jonas Bekaert[2], Milorad Milošević[2], Zoran Popović[3] and Nenad Lazarević[1]

[1]Institute of Physics, University of Belgrade, Pregrevica 118, 11080 Belgrade, Serbia
[2]Department of Physics & NANOlab Center of Excellence, University of Antwerp, Groenenborgerlaan 171, B-2020 Antwerp, Belgium
[3]Serbian Academy of Sciences and Arts, Knez Mihailova 35, 11000 Belgrade, Serbia

Abstract. Quasi-2D materials have gained a significant attention in the last few years because of their unique physical properties. The family of transition metal dichalcogenides is particularly intriguing due to their complex phase diagrams, characteristic optical properties and possibility to observe collective electron phenomena at higher temperatures. A strong correlation was observed between the electron-phonon interaction and the CDW phase in materials that display such states. Recent study has revealed that crystalline disorder promotes superconductivity while simultaneously suppresses CDW phase in metallic single crystal alloys of 2H-TaSe$_{2-x}$S$_x$.

Raman spectroscopy was used to investigate the effect of defects on lattice dynamics and electron-phonon coupling in these materials, and the results were compared to theoretical calculations. In our scattering configuration two out of four Raman active modes predicted by symmetry for parent compounds are identified. Additionally, in the spectra of pure samples broad two-phonon structures are observed, emerging as a consequence of strong electron-phonon coupling in related phonon branches. By substituting Se with S atoms, extra peak obeying A$_{1g}$ selection rules, overtone in nature, appears in spectra along with an intriguing evolution of two-phonon structure. The Raman spectra of the x = 0.84 sample shows single-phonon excitations that are superimposed on already existing structure. These excitations correspond to PDOS maxima projected due to significant crystallographic disorder. Symmetry predicted A$_{1g}$ modes expectedly harden with doping as unit cell volume decreases, whereas E$_{2g}$ modes exhibit anomalous behavior attributed to enhanced electron-phonon coupling. The analysis of E$_{2g}$ mode Fano parameter indicates that disorder has a minor impact on electron-phonon interaction.